

MASARYKOVA UNIVERZITA
PŘÍRODOVĚDECKÁ FAKULTA
ÚSTAV TEORETICKÉ FYZIKY A ASTROFYZIKY

Bakalářská práce

BRNO 2021

DANIEL JADLOVSKÝ

Fotometrické a spektroskopické charakteristiky červeného veleobra Betelgeuse

Bakalářská práce

Daniel Jadlovský

Bibliografický záznam

Autor:	Daniel Jadlovní Přirodovědecká fakulta, Masarykova univerzita Ústav teoretické fyziky a astrofyziky
Název práce:	Fotometrické a spektroskopické charakteristiky červeného veleobra Betelgeuse
Studijní program:	PřF B-FY Fyzika
Studijní obor:	PřF ASTR Astrofyzika
Vedoucí práce:	prof. Mgr. Jiří Krtička, Ph.D.
Akademický rok:	2020/2021
Počet stran:	viii + 71
Klíčová slova:	Betelgeuse; červení veleobři; radiální rychlost; fotometrie; spektroskopie; hvězdná pulzace

Bibliographic Entry

Author:	Daniel Jádlovský Faculty of Science, Masaryk University Department of Theoretical Physics and Astrophysics
Title of Thesis:	Photometric and spectroscopic characteristics of red supergiant Betelgeuse
Degree Programme:	PřF B-FY Physics
Field of Study:	PřF ASTR Astrophysics
Supervisor:	prof. Mgr. Jiří Krtička, Ph.D.
Academic Year:	2020/2021
Number of Pages:	viii + 71
Keywords:	Betelgeuse; red supergiants; radial velocity; photometry; spectroscopy; stellar pulsations

Abstrakt

Betelgeuse je pulzující červený veleobr, jehož jasnost se nepravidelně mění a v únoru 2020 dosáhla historického minima. Cílem této práce je charakterizovat proměnnost Betelgeuse na základě dostupných archivních dat a studium možných příčin proměnnosti. Pro spektrální charakterizaci bylo použito velké množství spekter z ultrafialové a optické oblasti. Spektra byla využita zejména pro určení radiálních rychlostí a jejich dlouhodobého vývoje v obou oblastech. Bylo také využito velkého množství fotometrických dat v různých filtrech k vytvoření světelné křivky a určení period jejích změn. Spektroskopické a fotometrické proměnnosti jsou vzájemně porovnány a dány do kontextu s historickým minimem, i za použití hvězdných modelů.

Abstract

Betelgeuse is a pulsating red supergiant whose brightness is semi periodically variable and in February 2020 reached a historical minimum, the Great Dimming. The aim of this thesis is to characterize Betelgeuse's variability based on available archival data and to study possible causes of light variability. A large number of spectra, from ultraviolet and optical regions, were evaluated for spectral analysis. The spectra were used primarily to determine radial velocities and their long term evolution. Additionally, photometric data was analysed in different filters as well, to create a light curve and to determine periods of the variability. Spectroscopic and photometric variability are compared to each other and given into a context with the Great Dimming, using theoretical stellar models as well.

ZADÁNÍ
BAKALÁŘSKÉ PRÁCE

Akademický rok: 2020/2021

Ústav:	Přírodovědecká fakulta
Student:	Daniel Jadlovský
Program:	Fyzika
Obor:	Astrofyzika

Ředitel ústavu PřF MU Vám ve smyslu Studijního a zkušebního řádu MU určuje bakalářskou práci s názvem:

Název práce:	Fotometrické a spektroskopické charakteristiky červeného veleobra Betelgeuze
Název práce anglicky:	Photometric and spectroscopic characteristics of red supergiant Betelgeuse
Jazyk závěrečné práce:	angličtina

Oficiální zadání:

Betelgeuze je hvězdou na konci svého vývoje. Tento červený obr vykazuje nepravidelnou světelnou proměnnost. Cílem bakalářské práce je studium proměnnosti hvězdy a možností jejího vysvětlení. Bude provedena spektroskopická charakterizace hvězdy na základě dostupných archivních ultrafialových a optických spekter. Bude studována proměnnost hvězdy v ultrafialovém a optickém oboru a budou hledány možné příčiny proměnnosti hvězdy.

Literatura:

- Gray, R. O., Corbally, C. J.: Stellar Spectral Classification
- Maeder, A.: Physics, Formation and Evolution of Rotating Stars
- van Loon, J. Th.: EAS Publications Series, 60, 2013, pp.307

Vedoucí práce:	prof. Mgr. Jiří Krtička, Ph.D.
Konzultant:	doc. RNDr. Vladimír Štefl, CSc.
Datum zadání práce:	11. 3. 2020
V Brně dne:	27. 5. 2021

Zadání bylo schváleno prostřednictvím IS MU.

Daniel Jadlovský, 22. 1. 2021

prof. Mgr. Jiří Krtička, Ph.D., 26. 1. 2021

Mgr. Michael Krbek, Ph.D., 1. 2. 2021

Poděkování

Na prvním místě bych chtěl poděkovat vedoucímu mé práce prof. Mgr. Jiřímu Krtičkovi, Ph.D., za přijetí mého návrhu na téma bakalářské práce a jeho rozvinutí do řádné podoby, a zejména za jeho vytrvalou a neochvějnou podporu, rady a trpělivost. Chtěl bych poděkovat doc. Ernstu Paunzenovi, Dr.rer.nat., za poskytnutí přístupu k datům z družice SMEI a jejich základní kalibraci. Chtěl bych také poděkovat správci archivu ASTRAL Thomasu Ayresovi, Ph.D., z University of Colorado, který mi poradil ohledně dat v archivu a poskytl referenční ultrafialové spektrum Betelgeuse. V neposlední řadě bych chtěl poděkovat ostatním učitelům, přátelům a zejména rodině za podporu a pomoc.

Prohlášení

Prohlašuji, že jsem svoji bakalářskou práci vypracoval samostatně pod vedením vedoucího práce s využitím informačních zdrojů, které jsou v práci citovány.

Brno 16. června 2021

.....
Daniel Jadlovský

Contents

Introduction	1
1. Evolution of Stars	2
1.1 Observational Stellar Parameters	2
1.2 Star Formation	4
1.2.1 Cloud Contraction	4
1.2.2 Protostars	5
1.3 Main Sequence	6
1.3.1 Low Mass Stars	7
1.3.2 Massive Stars	8
1.4 Post-Main Sequence	9
1.4.1 Low Mass Stars	9
1.4.2 Intermediate Mass Stars	10
1.4.3 Massive Stars	10
1.5 End States of Stars	11
1.5.1 White Dwarfs	11
1.5.2 Neutron Stars	12
1.5.3 Black Holes	12
2. Betelgeuse and Red Supergiants	13
2.1 Red Supergiants	13
2.1.1 Evolution at Constant Mass	13
2.1.2 Evolution of Red Supergiants	14
2.1.3 Mass Loss Rate and Stellar Winds	16
2.1.4 Rotation	17
2.1.5 Chemical Abundance	18
2.2 Betelgeuse	19
2.2.1 History of Observation	19
2.2.2 Physical Characteristics	20
2.2.3 Variability	21
2.2.4 2019-2020 Dimming	22
3. Stellar Spectroscopy	25
3.1 Formation of Spectrum	25

3.1.1 Continuous Spectrum	25
3.1.2 Absorption Lines	26
3.1.3 Emission Lines	26
3.1.4 Spectral Classes of Stars	26
3.2 Spectral Lines	27
3.2.1 Radial Velocity	28
3.2.2 Rotational Velocity	28
3.2.3 Temperature and Gravitational Acceleration	29
3.2.4 Density of Outer Layers	29
3.2.5 Chemical Composition	29
4. Spectral and Photometric Analysis of Betelgeuse	30
4.1 Spectroscopy	30
4.1.1 Spectral Analysis	30
4.1.2 Optical Spectra	31
4.1.3 UV spectra	34
4.1.4 Radial Velocity	39
4.1.5 Rotational Velocity	42
4.2 Photometry	44
4.2.1 BRITe	45
4.2.2 SMEI	46
4.2.3 AAVSO	47
4.2.4 Light Curve	47
4.3 Period Analysis	48
4.3.1 Photometric Variability	49
4.3.2 Radial Velocity Variability	49
4.4 Radial-Light Curve	52
4.5 Discussion on the Great Dimming	52
4.5.1 Models of Stellar Fluxes	54
Conclusion and Future Insights	56
Appendix	59
Bibliography	65

Introduction

Betelgeuse has always been one of the most famous stars since people started observing the sky. It is easily visible to a naked eye due to its extraordinary brightness. It is even brighter in the infrared spectrum. Along with the orange colour that Betelgeuse has, it is one of the essential stars of Orion constellation. When the astronomers started to study Betelgeuse more closely, they discovered that it is an old red supergiant star, which also has a semi-regular variability consisting of at least two long periods that cause extensive changes in its brightness. However, recently the brightness of the star dropped significantly lower than ever before, which has brought more attention to the star, as we still do not know enough about these types of stars, especially in this part of their evolution. Many theories to explain this unprecedented behaviour have been published recently, such as that the drop in brightness is caused by a convergence of the two periods, or such as more audacious ones, hypothesizing that Betelgeuse may soon explode as a supernova.

Therefore, in this thesis I will undergo a photometric and spectroscopic analysis of Betelgeuse, with an intent to shed some light into the processes that could have caused this recent eccentric behaviour of the star.

To be able to examine Betelgeuse's behaviour and analyse it, it is imperative to properly understand stars and their physical processes. Thus in the first chapter of this thesis I will describe a general evolution of all stars, from the beginning of their life cycles to their end states, while slightly focusing on more massive stars. In the second chapter I will then go from a general approach to an entirely specific one, and focus solely on red supergiants and Betelgeuse itself. In the third chapter I will summarize essential spectroscopic methods that we are able to use to study stellar spectra.

In the final chapter, I will provide my own photometric and spectroscopic study of Betelgeuse's variability and combine it with various relevant published results, in an attempt to provide some context to the recent unprecedented behaviour.

Chapter 1

Evolution of Stars

1.1 Observational Stellar Parameters

To be able to discuss the evolution of stars, it is first necessary to define some fundamental astrophysical relations.

Flux

A radiative flux F_r from a star is total amount of light energy that crosses a unit area that is orientated perpendicularly to the direction of light's travel per a unit of time, and is given by

$$F_r = \frac{L}{4\pi r^2}, \quad (1.1)$$

where r is a diameter of a spherical shell surrounding a star of luminosity L ([Carroll & Ostlie, 2007](#)).

Magnitude

The brightness of a star is expressed by apparent magnitude m , given by Pogson's equation

$$m_1 - m_2 = -2.5 \log_{10} \left(\frac{F_1}{F_2} \right). \quad (1.2)$$

m is the brightness of the star as seen by an observer, which means that it depends on distance r . When talking of apparent magnitude m in a specific filter, a different symbol may be used. For example apparent magnitude m in visible light can be marked as m_V or V . To acquire an intrinsic brightness, we use absolute magnitude M of a star. Using one of the magnitudes in equation 1.2 as an apparent magnitude a star would have in distance d of 10 pc, and using F_r from equation 1.1, we can derive a relation for absolute magnitude

$$M = m - 5 \log_{10}(d) + 5 + A, \quad (1.3)$$

where A in magnitudes is an extinction along our line of sight. Absolute magnitude M is therefore used to directly compare brightness of stars ([Gray & Corbally, 2009](#)).

Effective Temperature

If we use equation 1.1 as flux in distance $r = R$ along with Stefan-Boltzmann equation, we can implement

$$F_{\text{surf}} = \sigma T_{\text{eff}}^4, \quad (1.4)$$

where σ is Stefan-Boltzmann constant and T_{eff} is effective temperature of a stellar surface. Therefore we can also write that luminosity L is given by

$$L = 4\pi R^2 \sigma T_{\text{eff}}^4 \quad (1.5)$$

(Carroll & Ostlie, 2007).

HR diagram

Hertzsprung-Russel diagram (HR diagram) is undoubtedly one of the most important and influential diagrams in astrophysics. Although there are many variations of the diagram, the basic part is the same. It is a plot of luminosity L versus surface temperature T_{eff} , or the related quantities, such as absolute magnitude M versus stellar class, and other combinations, as we can see in figure 1.1.

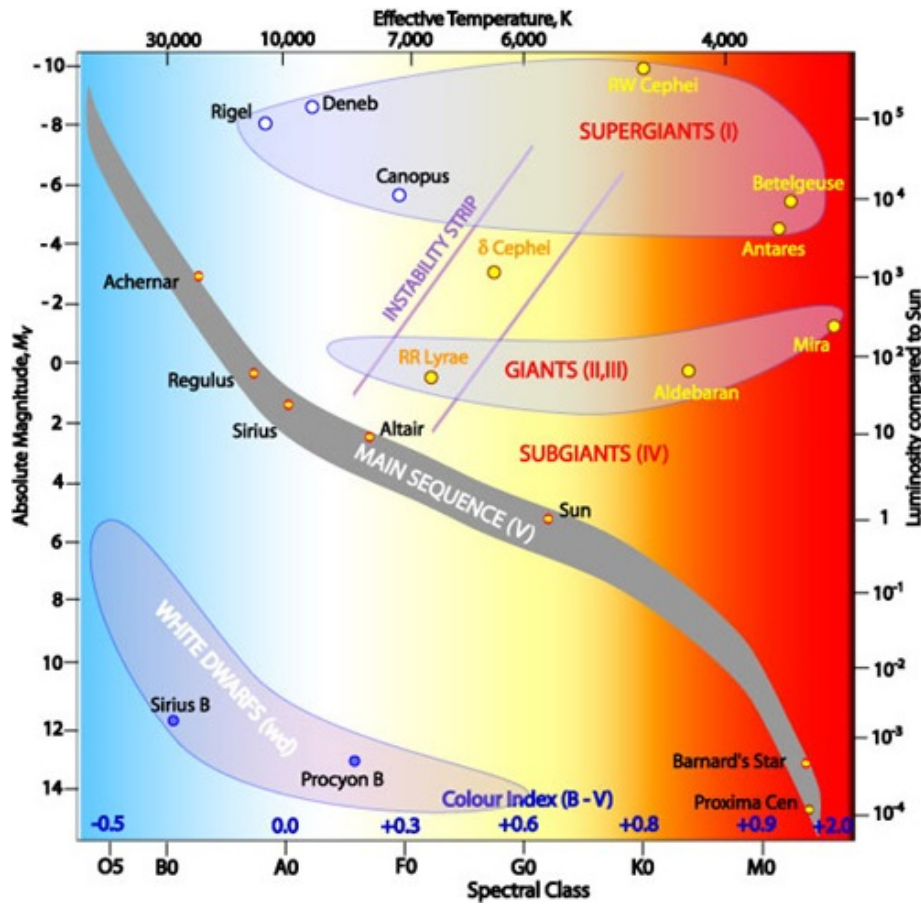


Figure 1.1: This basic version of the HR diagram shows the main stages of star evolution and also labels some notable stars. Taken from E1.

In the HR diagram we can notice that stars are classified into several groups, most noticeably the main sequence. The HR diagram is not static, stars change their positions within it over the course of their evolution, hence we are going to use the diagram several times in the following chapters. The HR diagram effectively shows how the stars evolve. After the protostar and contraction evolution, the star descends into the main sequence track, where it stays for a majority of its life. The exact length depends on a mass of the star. Once the star exhausts its main fuel resource in the core, it increases its radius, leaves the main sequence and enters post-main sequence (the exact evolution is strongly dependant on mass), where it stays for much a shorter time than on the main sequence. After this turbulent era, once the star burns out other fuel resources, it ends its life in various forms ([Stahler & Palla, 2005](#)).

We will explore the exact evolution of stars more closely, in dependence on their mass, in the following chapters.

1.2 Star Formation

1.2.1 Cloud Contraction

Stars seem to never form alone, but simultaneously in dense interstellar clouds of huge sizes and masses. Thus afterwards their creation, those stars are part of open clusters, that may typically contain hundreds of stars. However, for a star to arise from these clouds, it first has to become a protostar and undergo several processes. If mass M of an interstellar cloud is large enough, it can start to contract under its own gravity ([Elridge & Tout, 2019](#)). This is described by Jeans mass M_J

$$M_J \approx \left(\frac{5kT}{G\mu m_H} \right)^{3/2} \left(\frac{3}{4\pi\rho_0} \right)^{1/2}, \quad (1.6)$$

where the variables are temperature T of a cloud and its density ρ_0 ([Carroll & Ostlie, 2007](#)). G is the gravitational constant, k is the Boltzmann's constant, μ is the mean molecular weight and m_H is a molecular mass of hydrogen. For a contraction to be possible, mass M of a cloud must overcome the Jeans mass. It is accomplished by cold clouds of high density ρ . Diameters of the clouds are of the order of 10 pc, and are typically located in the spiral arms of the Galaxy. It is not fully known what causes a cloud to contract, but generally it is caused by some external nearby processes, such as when a cloud is passing through a spiral arm or when a nearby supernova explodes ([Elridge & Tout, 2019](#)).

Once the cloud begins to contract, the newly created heat is radiated away, because the opacity κ is still too low. That further decreases M_J and that creates a fragmentation within the cloud. The fragments continue contraction on their own until the opacity κ increases due to increased density ρ , which causes the fragment to heat up. This, along with the rising pressure p , causes the contraction to stop in the inner parts of the cloud, while the outer parts are still falling freely. During this, the cloud may already be considered a protostar ([Karttunen et al., 1996](#)).

1.2.2 Protostars

A cloud that has satisfied the Jeans criterion, can be described by free-fall (dynamical) time scale

$$t_{\text{ff}} = \sqrt{\frac{3\pi}{32} \frac{1}{G\rho_0}}. \quad (1.7)$$

It is the time it would take for the radius of a collapsing sphere to reach a zero value. It only depends on the initial density ρ_0 and not on initial radius.

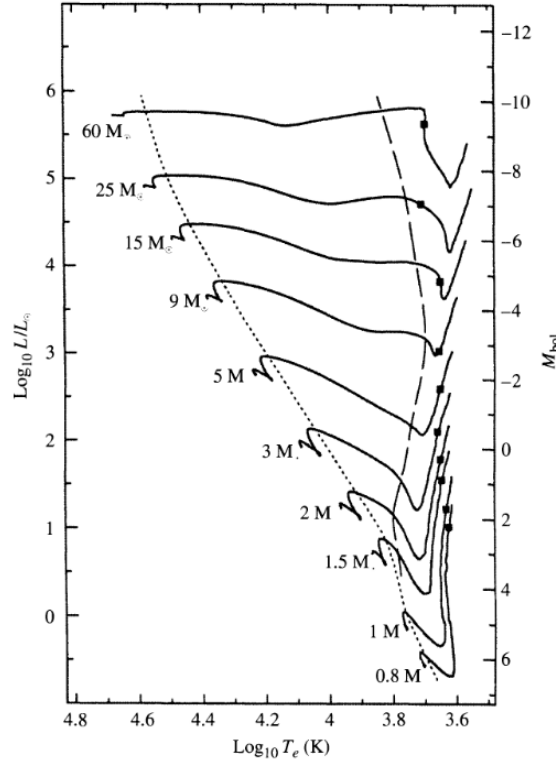


Figure 1.2: Figure shows evolutionary tracks of stars of various masses M , starting at the Hayashi track and heading towards Zero Age Main Sequence (ZAMS). Contraction times are shown in table 1.1. Original figure is from [Bernasconi & Maeder \(1996\)](#), edited by [Carroll & Ostlie \(2007\)](#).

Once the protostar accumulates more mass and is optically thick enough, while being in a hydrostatic equilibrium, the evolution is controlled by Kelvin-Helmholtz (thermal) time scale

$$t_{\text{KH}} = \frac{\Delta E_g}{L} = \frac{\frac{3}{10} \frac{GM^2}{R}}{L}, \quad (1.8)$$

where ΔE_g is total mechanical energy of a protostar gained from the virial theorem. The liberated energy is the source of object's luminosity L gradually released over time. R is radius of a protostar and M is mass of a protostar. t_{KH} is much longer than t_{ff} , therefore the evolution towards the main sequence takes much longer than the collapse ([Stahler & Palla, 2005](#)). By this time the protostar has already decreased its radius significantly and is accreting material from its surroundings, therefore further increasing its mass M . When

the star reaches a hydrostatic equilibrium, the temperature T is still low. Due to the large opacity κ , the star will become convective, which is an efficient energy transfer under these circumstances.

Once the star is fully convective, it will settle on the Hayashi track in HR diagram. The track is a boundary between protostars that are at the previously mentioned low temperature hydrostatic equilibrium and protostars that cannot be in a hydrostatic equilibrium. To the right side of the track, there is no mechanism that could support luminosity of such a protostar (because the output of nuclear reactions is not high enough yet), while on the left side the energy transport is covered by convection or radiation (Carroll & Ostlie, 2007).

A protostar descends the track, until the temperature in the core is high enough to ignite nuclear reactions or to form a radiative core. Once the nuclear reactions fully cover luminosity L of a star, it enters the main sequence. Nonetheless, if a protostar has lower mass M than about $0.08 M_{\odot}$, then the mass is not sufficient to ignite hydrogen reactions. In such a scenario, the star becomes a brown dwarf (Hayashi & Nakano, 1963).

Initial Mass [M_{\odot}]	Contraction Time [Myr]
60.0	0.0282
25.0	0.0708
15.0	0.117
9.0	0.288
5.0	1.15
3.0	7.24
2.0	23.4
1.5	35.4
1.0	38.9
0.8	68.4

Table 1.1: Contraction times for stars in figure 1.2. The data are from Bernasconi & Maeder (1996).

1.3 Main Sequence

During the main sequence the dominant energy source for stars are nuclear fusion reactions in stellar cores. These reactions use primarily hydrogen available in the core and it provides the star with a continuous stable income of energy, allowing such a star to be in a relative stability, compared to other evolutionary phases. The position of a star is not completely stationary in HR diagram during the main sequence, but it is slightly increasing in luminosity and brightness, henceforth it moves upwards from ZAMS. Once all the hydrogen in the inner parts of a star is burnt, the stability is disrupted and the star abandons the main sequence. However, there is enough hydrogen to make the equilibrium last for a significant period of time, in most cases, for billions of years, depending on a mass M of the star (Elridge & Tout, 2019).

Instead of free-fall (1.7) and Kelvin-Helmholtz (1.8) time scales, a star can now be described using the nuclear time scale (Carroll & Ostlie, 2007), which is the time that it

Initial Mass [M_{\odot}]	Main Sequence Duration [Myr]
85.0	2.8
40.0	4.3
20.0	8.1
9.0	26.0
4.0	160.0
2.0	1100.0
1.0	10 000.0
0.8	25 000.0

Table 1.2: Time that stars spend on the main sequence in dependence on their mass M . The time basically corresponds to the length of hydrogen burning in a core of the star. The table is from [Mikulášek & Krtička \(2005\)](#).

would take for a star to exhaust all its (hydrogen) nuclear reactions energy and is given by

$$t_n = \frac{E_n}{L} \approx \frac{0.007 q_c M c^2}{L}, \quad (1.9)$$

where E_n is energy released by nuclear reactions, q_c is the mass fraction that is used for the reactions and c is the speed of light. Only 0.7 % of the mass of hydrogen is converted into energy during the reactions. Typically, only about 10 % of hydrogen within sun-like stars is used for nuclear reactions. For Sun, the result of equation 1.9 would be $\approx 10^{10}$ years ([Carroll & Ostlie, 2007](#)).

Therefore, the equation 1.9 can be rewritten as

$$t_n \approx 10^{10} \text{ years} \left[\frac{M}{M_{\odot}} \right] \left[\frac{L_{\odot}}{L} \right], \quad (1.10)$$

which can be used to approximately calculate the duration of the main sequence for any star.

1.3.1 Low Mass Stars

For stars with mass M of less than about $1.2 M_{\odot}$ the most efficient hydrogen fusion reaction is the pp chain (table 1.3), due to their low core temperature T . The pp chain converts nucleons of hydrogen into an α -particle (${}^4\text{He}$), releasing a significant amount of energy.

In such low-mass stars the core is radiative, which is due to energy being produced in a large portion of the star. In the same time, opacity κ in outer layers is higher due to lower temperature T , henceforth these outer layers are convective, which means that the energy is being transferred by macroscopic motion of materials. Due to no convective motion in the core, the abundance of hydrogen in the core decreases at a much faster pace than in outer layers ([Pols, 2011](#)).

However, stars of the lowest mass from this group (M lower than $\sim 0.5 M_{\odot}$) are an exception, they are fully convective for the whole duration of the Main Sequence ([Carroll & Ostlie, 2007](#)).

		Q [MeV]	Approximate τ
$^1\text{H} + ^1\text{H}$	$\rightarrow ^2\text{H} + e^+ + \nu_e$	1.442	$7.0 \cdot 10^9$ yr
$^2\text{H} + ^1\text{H}$	$\rightarrow ^3\text{He} + \gamma$	5.493	1.0 s
$^3\text{He} + ^3\text{He}$	$\rightarrow ^4\text{He} + 2\ ^1\text{H}$	12.859	$1.5 \cdot 10^5$ yr

Table 1.3: Reactions of pp chain. The first two reactions have to happen twice for the third reaction to be possible, hence 4 nucleons of hydrogen are required for the whole chain. The total amount of liberated energy is 26.23 MeV. There are also two other types of pp chain taking place in the core, but they are less common in overall. Q is the reaction energy and τ is the approximate time duration for the reaction to take place. Data taken from [Maeder \(2009\)](#).

1.3.2 Massive Stars

In cores of more massive stars the temperature T is high enough for CNO cycle (table 1.4) to become more effective than the pp chain. The overall function of the cycle is very similar to the pp chain, four nucleons of hydrogen are converted into an α -particle, but the cycle also requires presence of CNO elements. These elements serve as catalysts of the reaction. Even though the cycle has a similar energy outcome as pp chain, the time required for the whole cycle to happen is considerably shorter ([Maeder, 2009](#)).

		Q [MeV]	Approximate τ
$^{12}\text{C} + ^1\text{H}$	$\rightarrow ^{13}\text{N} + \gamma$	1.944	10^3 yr
^{13}N	$\rightarrow ^{13}\text{C} + e^+ + \nu_e$	2.211	420 s
$^{13}\text{C} + ^1\text{H}$	$\rightarrow ^{14}\text{N} + \gamma$	7.750	$2.9 \cdot 10^2$ yr
$^{14}\text{N} + ^1\text{H}$	$\rightarrow ^{15}\text{O} + \gamma$	7.293	$9.4 \cdot 10^4$ yr
^{15}O	$\rightarrow ^{15}\text{N} + e^+ + \nu_e$	2.761	120.0 s
$^{15}\text{N} + ^1\text{H}$	$\rightarrow ^{12}\text{C} + ^4\text{He}$	4.966	3.7 yr

Table 1.4: Reactions of CN cycle. The total amount of liberated energy is 25.03 MeV (without neutrinos). There are also 3 ON branches, which become more relevant for even higher temperatures. Data taken from [Maeder \(2009\)](#).

As the cycle is much more efficient and temperature dependant than the pp chain, it is significantly restricted to the core of a star. The energy production is stronger, which causes the inner parts to become convective. That ensures a steady income of hydrogen to the core, therefore the abundances are similar in the whole convective zone. The size of a convective zone may encompass the majority of a star. In the outer parts, the opacity κ is lower, as well as the flux of energy. That causes the envelope to be radiative.

1.4 Post-Main Sequence

Once all the hydrogen in the core is turned into helium, the star is now in a phase when there is a burning hydrogen shell surrounding a helium core. As the helium core attains more mass, the envelope expands, and because of the nuclear burning in the shells, the luminosity L increases (Karttunen et al., 1996). The star is now in Sub Giant Branch phase (SGB). Eventually, the mass M of the helium core reaches the Schönberg-Chandrasekhar limit, and begins to contract. The evolution of a star proceeds on the much faster Kelvin-Helmholtz time scale 1.8. The released energy causes the envelope to expand, and therefore surface temperature to decrease in result. The star is now on it's way to enter the Red Giant Branch phase (RGB), or the Red Supergiant Branch phase (RSGB) instead, if the mass M is high enough. Some stars may experience a first dredge-up of material before that. Based on the mass M of a star, there may be several upcoming phases (Carroll & Ostlie, 2007).

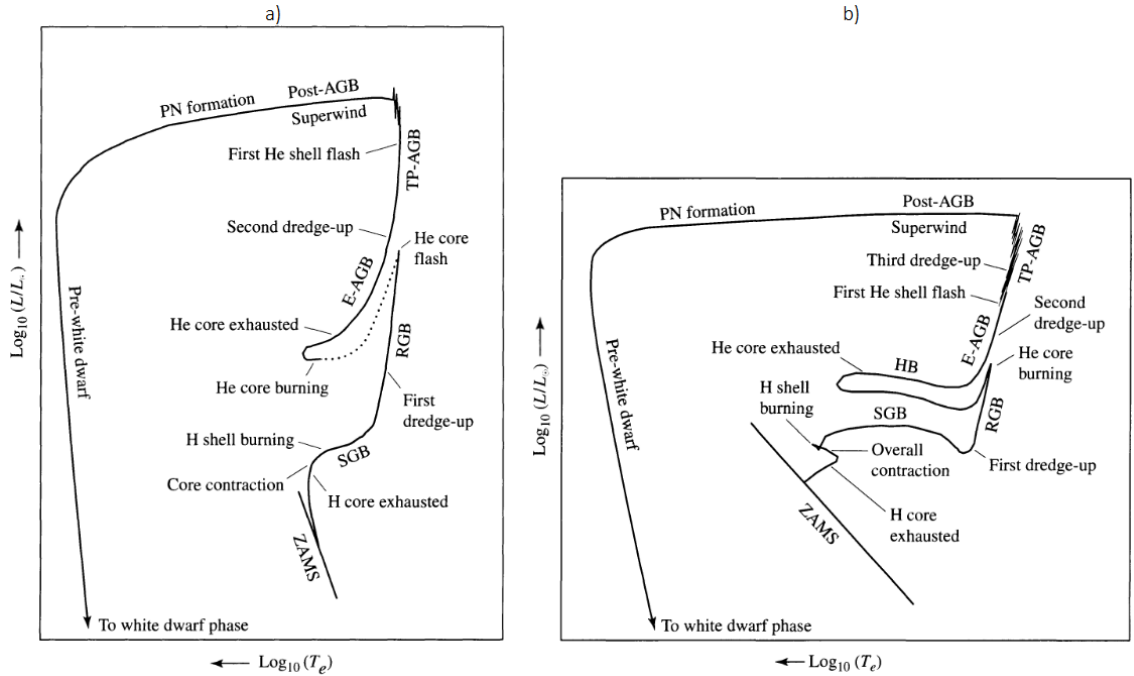


Figure 1.3: Figure shows a schematic diagram of post-main sequence phases, starting at ZAMS. a) is for $1 M_{\odot}$ stars and b) is for $5 M_{\odot}$ stars. Dredge-ups refer to phases when material from deeper layers of a star are being pushed to the surface. The different heights and widths of axis are not to scale. Original figure is from Carroll & Ostlie (2007).

1.4.1 Low Mass Stars

In low mass stars the density ρ of the helium core continues to grow, until the core becomes degenerate. Along with density ρ also the core temperature T grows, which will consequently lead to ignition of helium burning. That empowers a sudden increase in the core temperature, which ultimately removes the degeneracy and simultaneously causes the gas to abruptly expand. This all happens just in a matter of seconds after the helium

begins to burn, and it is followed by an explosion, the helium flash. The explosion in the end causes a decrease in luminosity L , because while the core expands, the outer layers contract. Eventually, a balanced state is reached again and the expanded core continues to burn helium (Maeder, 2009).

This phase ends when the star burns all the helium in its inner core. The helium continues to burn in a lower shell, while the hydrogen burns in an outer shell. That moves the star to the Asymptotic Giant Branch (AGB). This Branch can be divided into two parts. During early Asymptotic Giant Branch (E-AGB) the helium burning shell is the primary source of energy output, due to the activity of hydrogen burning in the outer shell being lower (Karttunen et al., 1996). Afterwards, during Thermal-pulse Asymptotic Giant Branch (TP-AGB), the hydrogen burning becomes dominant again, whereas the helium-burning activity increases and decreases quasi-periodically. That repeatedly occurs due to a new shell of not burning helium being created between the two burning shells, as a result of hydrogen-burning. The shell increases degeneration of the inner helium shell, diminishing the helium-burning activity, until the rising core temperature T eventually ignites the helium-burning activity again, accompanied by the helium flash. Although, this flash is less energetic than the first one (Carroll & Ostlie, 2007).

As the star in this state is not stable, and the core temperature T is not high enough to ignite burning of carbon, the giant eventually starts to lose its outer layers. The ejected layers become a planetary nebula (PN), carried away by superwind of a star, while the core becomes a white dwarf (Kippenhahn et al., 2012).

1.4.2 Intermediate Mass Stars

Unlike in the low-mass stars, the core of intermediate mass stars will not become degenerate during the RGB phase, as the core density ρ is lower, while the temperature T is higher. That allows the helium to begin burning without the helium flash. Afterwards the process continues similarly as with the low-mass stars (Carroll & Ostlie, 2007).

1.4.3 Massive Stars

Assuming that the initial mass of the star is higher than about $7 M_{\odot}$, it can burn elements all the way up to iron, therefore there may be several shells burning simultaneously, such as carbon, oxygen and silicon. Once the inner core is converted into an iron core, there are no further available exothermic nuclear reactions to burn it, therefore energy ceases to be produced. Electron degenerate core grows in mass, but eventually Chandrasekhar limit is exceeded, and the core begins to contract. When the temperature T in the contracting core is sufficiently high, photons have high enough energy to disintegrate heavier nuclei into protons and neutrons, most importantly the iron. This process is called photodisintegration and is highly endothermic. The protons created by photodisintegration capture electrons and form neutrons, leading to the emission of highly energetic neutrinos, therefore electron degeneracy pressure is severely weakened and the core begins to contract extremely rapidly (Carroll & Ostlie, 2007). The free-fall time scale 1.7 can be used to describe the contraction. In the most dense cores, the contraction will take just a fraction of a second (Karttunen et al., 1996). Other shells are also collapsing, but at slower pace, while the yet unburned

fuel is being strongly heated up. Ultimately, the outer layers explode as a supernova and release a tremendous amount of energy (Kippenhahn et al., 2012). Depending on the mass of the contracting core, the core may become a neutron star or a black hole, which will be explored in [section 1.5](#).

Stars with mass between about $7-8 M_{\odot}$ may undergo a carbon flash, which is incomparably more powerful than the helium flash, and would likely cause the star to be scattered in a supernova explosion. Whether the star explodes depends on a mass loss rate and the increasing temperature T and density ρ in the core (Maeder, 2009).

Supernovae

Due to the enormous energy provided by a supernova explosion, formation of even heavier elements than iron is possible during such an event. Supernovae can be divided in several categories, based on a composition of their spectra.

Type I supernovae have no hydrogen lines in their spectra, which suggests that the collapsing star is a highly evolved object, which has already lost its hydrogen envelope. Their light curves and spectra are similar to each other, especially supernovae of type Ia (Iben & Tutukov, 1984), which makes it possible to use them for determining distances. Spectra of type Ia supernovae have strong Si II absorption lines, which are missing in spectra of type Ib and Ic supernovae. The main difference between spectra of type Ib and Ic supernovae is that spectra of supernovae of type Ib have strong He lines, while spectra of type Ic do not (Bianco et al., 2014).

Spectra of type II supernovae includes hydrogen spectral lines and are generally dimmer than type Ia. This type is being associated with the core collapse of massive stars, and are typically located in regions, where stars have recently formed (Turatto, 2003).

The absolute magnitude of type Ia supernovae can reach up to -19.6 mag, while the supernovae of types Ib, Ic and II are generally about 1.5 mag dimmer (Mikulášek & Krtićka, 2005).

1.5 End States of Stars

Whether the electron degeneracy pressure gradient is able to support the core of a star is described by Chandrasekhar limit (Chandrasekhar, 1935). The limit is $\approx 1.46 M_{\odot}$ (Pols, 2011).

1.5.1 White Dwarfs

As discussed in the previous chapter, a white dwarf is a stellar remnant of low-mass stars. The gradient of electron degeneracy pressure in the core, created due to quantum effects when all the allowed energy levels fill up, managed to cease the contraction driven by the gravitational forces and the core becomes a white dwarf. The electron degeneracy pressure is independent of temperature T and increases with density ρ . The white dwarfs will slowly cool down, even though they have no source of nuclear energy (Sion et al., 2019). The sizes of white dwarfs range from 0.008 to $0.02 R_{\odot}$ (Morison, 2019).

1.5.2 Neutron Stars

If the core continues to contract further and it reaches a sufficient density ρ , the neutrons become degenerate and even more powerful neutron degeneracy pressure comes into an effect. The degeneracy pressure gradient may be able to support the core, in which case a neutron star would emerge. Such an object has diameter R only on the order of kilometres, with an upper boundary of about 10 km ([Chamel et al., 2013](#)). Rapid long-term stable rotation of some neutron stars makes them an extremely useful tool for timing measurements ([Ozel & Freire, 2016](#)).

1.5.3 Black Holes

In case when the gradient of neutron degeneracy pressure fails to overcome the contraction, a black hole may be formed instead. Tolman-Oppenheimer-Volkoff limit describes this boundary, and sets the upper limit for a mass M of neutron stars to $2.2\text{--}2.8 M_{\odot}$ ([Kalogera & Baym, 1996](#)). Unlike other objects, which are composed of materials, a black hole is a spacetime structure. The black holes were predicted by the theory of general relativity. Once matter or radiation fall below an event horizon of the black hole, it can never escape again. The event horizon is located at Schwarzschild radius

$$r_s = \frac{2GM}{c^2}, \quad (1.11)$$

where M is the mass of a black hole ([Lambourne, 2010](#)).

Chapter 2

Betelgeuse and Red Supergiants

We have already discussed the red supergiants in a very general manner in [section 1.4](#). However, now we will examine this phase of stellar evolution much deeper, so that we are able to discuss Betelgeuse in the necessary context.

2.1 Red Supergiants

The class of red giants and supergiants may loosely refer to various types of stars at different phases of post-main sequence evolution, based on their spectral class. In the following chapter, we will primarily focus on *true* red supergiants in an evolutionary context. Therefore, the stars that are currently on the Red Supergiant Branch (RSGB). If we take into consideration models that do not neglect mass loss and rotation, the evolutionary tracks may start to differ significantly. That will be explored further in [subsection 2.1.2](#) and the chapters that follow. Mass loss rate may also lead to a previously not mentioned evolved state of stars, Wolf-Rayet stars.

For a star of a solar metallicity to be able to become a red supergiant, its initial main sequence mass M must be between about $8\text{--}40\text{ M}_{\odot}$. Therefore, based on spectral classification, the spectral class of red supergiants' progenitors during the main sequence is primarily O, partially also B. During the RSGB phase, their spectral class is either M or K. If the mass M of a star is above the upper limit of 40 M_{\odot} , such a star would never cool down enough, hence it would remain a blue supergiant. For even higher initial mass M , above 60 M_{\odot} , the star would lose its outer layers during the main sequence, so it would likely never become a supergiant. On the other hand if the mass M of a star was below 8 M_{\odot} , it would become only a red giant and undergo post-main sequence as described in [section 1.4](#). However, the limits depend significantly on initial metallicity Z ([Maeder, 2009](#); [Ekström et al., 2012](#)).

2.1.1 Evolution at Constant Mass

As explored in the previous chapters, once the star runs out of hydrogen in its core, it will eventually start burning heavier elements. Light elements continue to burn in the shells surrounding the core. Based on the mass limit for red supergiants that we defined in the previous section, all stars in it should be able to burn elements all the way up to iron.

The primary nuclear reactions that follow after hydrogen are listed in table 2.1, along with other stellar properties during such phases.

Core Burning Phase	T_c [10^9 K]	L [$10^3 L_\odot$]	R [R_\odot]	Burning duration τ
He \rightarrow C & O	0.172–0.196	26–182	359–1030	$2.67–0.839 \cdot 10^6$ yr
C \rightarrow O, Ne & Mg	0.815–0.841	60–245	665–1390	$2.82–0.052 \cdot 10^3$ yr
Ne \rightarrow O & Mg	1.69–1.57	64–246	690–1400	0.341–0.891 yr
O & Mg \rightarrow Si	1.89–2.09	65–246	691–1400	4.77–0.402 yr
Si \rightarrow Ni & Fe	3.28–3.65	65–246	692–1400	17.8–0.733 d

Table 2.1: Stellar properties during the primary post-main sequences phases of nuclear burning and their durations. The values are for stars from mass interval of $13–25 M_\odot$, the first number in each column is always a value for a $13 M_\odot$ star, and the second value is for a $25 M_\odot$ star. Adapted from Woosley et al. (2002). Burning durations for hydrogen may be found in table 1.2.

Massive stars from our defined limit are not able to cool down enough from blue supergiants to become red supergiants before the end of helium burning phase, or even later when carbon is about to ignite. As we can see in table 2.1, the durations of all the phases after helium are extremely short, compared the duration of helium burning, and especially compared to hydrogen burning (table 1.2). That effectively means that the red supergiant phase is extremely short as well, as soon after this, they explode as a supernova, which in turn implies that we should not observe almost any red supergiants. While we do not observe many red supergiants, it is still more than we should have been able to observe based on this simplified model (Maeder, 2009). We can see results of such models in figure 2.1.

If we however take into consideration other effects, primarily mass loss, we will have more appropriate models. Such models will be used in the following chapters.

2.1.2 Evolution of Red Supergiants

As discussed above, in order to become a red supergiant (RSG) a star must often first become a blue supergiant (BSG). Approximate post-main evolution sequences of stars from our interval are shown in table 2.2. More massive stars than about $25 M_\odot$ have too high surface temperature T during the main sequence to cool down directly to the red. Supergiants with mass between $25–30 M_\odot$ may experience blue loops (Maeder, 2009). The mass loss of the star is the dominant cause of this, as it causes the helium core to represent a larger part of the total mass of the star than a star of this age typically has. Hence, it causes a blue ward evolution. On the other hand, the mass loss also helps supergiants with mass below $25 M_\odot$ to remain red supergiants, until they eventually explode (Meynet et al., 2015). This effect depends on the gravitational potential of the core Φ_c , the mass of the core M_c and the radius of the core R_c in the following manner:

$$\Phi_c \sim \frac{M_c}{R_c} \sim M_c^{0.4} \quad (2.1)$$

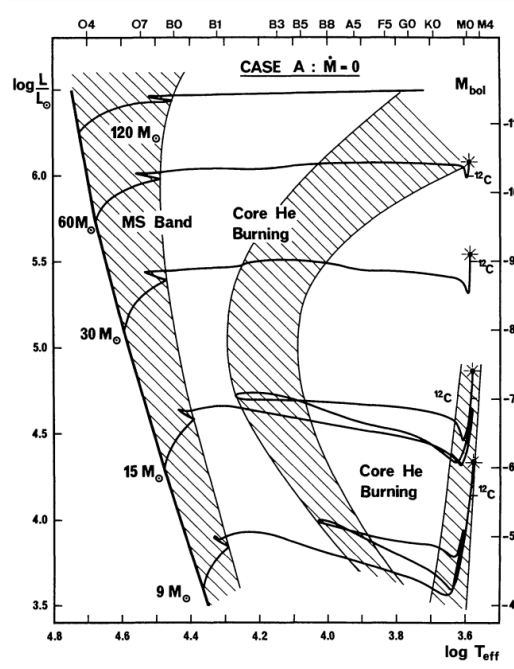


Figure 2.1: Stellar evolution at constant mass M . The "shiny dots" represent locations of pre-supernova models. The beginning of carbon burning is also labelled in the graph as " ^{12}C ". Original figure from (Maeder, 1981). See graph 2.2 for a comparison.

$$\Phi_c(M_c) < \Phi_{\text{crit}}(M) \Rightarrow \text{blue ward motion} \quad (2.2)$$

$$\Phi_c(M_c) > \Phi_{\text{crit}}(M) \Rightarrow \text{red ward motion} \quad (2.3)$$

Φ_{crit} increases with the total mass M of a star. Red supergiants have more concentrated cores than blue supergiants at a given mass (Kippenhahn et al., 2012).

$M [M_{\odot}]$	Evolution
30 – 40	O \rightarrow BSG \rightarrow RSG \rightarrow WR
25 – 30	O \rightarrow (BSG) \rightarrow RSG \rightarrow BSG \leftrightarrow RSG
10 – 25	OB \rightarrow RSG \rightarrow (Cepheid loop) \rightarrow RSG

Table 2.2: Tentative filiations based on solar neighborhood. \leftrightarrow indicates possible back and forth evolution between two stages, in this case the blue loop. The mass limits are uncertain, depending on Z . Wolf-Rayet (WR) stars are evolved massive stars that lost their outer envelopes. Cepheid loop occurs for stars with $M < 15 M_{\odot}$. For red supergiants with lower mass, the evolution in figure 1.3 occurs. All these evolutions end with a supernova explosion. Adapted from Maeder (2009).

Low-mass supergiants may also enter nearly vertical cepheid instability strip, where they begin to pulsate, until they leave the strip (Carroll & Ostlie, 2007).

2.1.3 Mass Loss Rate and Stellar Winds

The mass loss rate \dot{M} of a star can be described in several ways. For a main-sequence OB star with $T_{\text{eff}} \geq 25000$ K, the mass loss rate depends on metallicity Z as

$$\dot{M} \sim Z^{0.69}. \quad (2.4)$$

And for B supergiants with $T_{\text{eff}} \geq 25000$ K, it can be described as

$$\dot{M} \sim Z^{0.64} \quad (2.5)$$

(Vink et al., 2001).

The mass loss rate can be also described using the luminosity L of a star (Crowther, 2004; Kippenhahn et al., 2012) based on observations in the following way:

$$\dot{M} \sim L^{1.6} \quad (2.6)$$

for OV stars, and as

$$\dot{M} \sim L^{1.5} \quad (2.7)$$

for OI stars.

To describe mass loss rate of red supergiants and AGB stars the so-called Reimer's law (Reimers, 1975) is widely used

$$\dot{M} = 4 \cdot 10^{-13} \eta \frac{LR}{M}, \quad (2.8)$$

where \dot{M} is in $M_{\odot} \text{ yr}^{-1}$, and η is a free variable, usually approximated by 1.

For dust enshrouded red supergiants and AGB stars that experience significant mass loss rates due to high dust opacity, it is also possible to use

$$\log \dot{M} = -5.65 + 1.05 \log \left[\frac{L}{10^4 L_{\odot}} \right] - 6.3 \log \left[\frac{T_{\text{eff}}}{3500 \text{ K}} \right] \quad (2.9)$$

(van der Hucht, 2006).

Stellar winds in the massive stars are largely responsible for the mass loss. Their velocities can reach up to 3000 km s^{-1} for OB stars, and up to mass loss rates of $10^{-5} M_{\odot} \text{ yr}^{-1}$. For the Sun, the mass loss rate due to the stellar wind is $10^{-14} M_{\odot} \text{ yr}^{-1}$. The mass loss due to line-driven winds may be described as

$$\dot{M} = N \frac{L}{c^2}, \quad (2.10)$$

where $\frac{L}{c^2}$ is mass loss by nuclear reactions per unit of time. It can therefore be interpreted as the mass loss rate for one optically thick line. N is then the number of lines effectively producing the mass loss rate. Values of N around 100 correspond to mass loss rates of main-sequence OB stars (Maeder, 2009).

In figure 2.2, the final masses are 11.09, 12.49, $24.80 M_{\odot}$ for initial masses 15, 30 and $60 M_{\odot}$, respectively. In case C, the corresponding final masses are 3.50, 10.15, $19.6 M_{\odot}$ (Maeder, 1981, 2009).

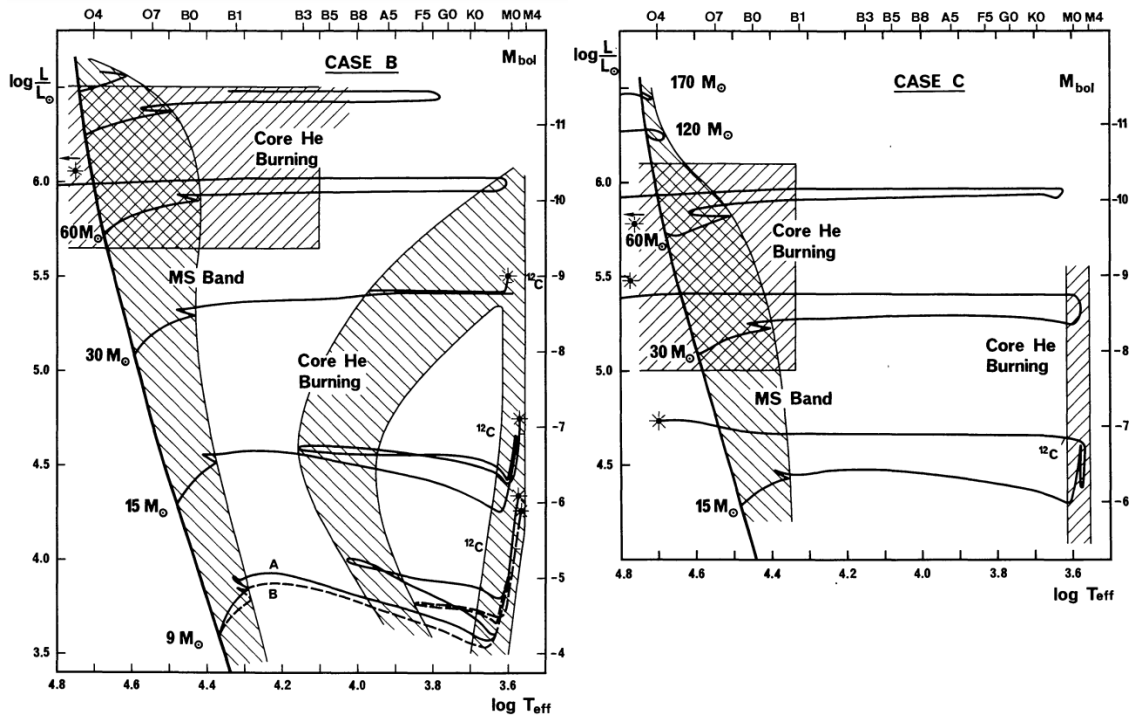


Figure 2.2: Post-main sequence evolution with mass loss for two cases of equation 2.10. Case B uses $N = 70$, and Case C uses $N = 140$. The "shiny dots" represent locations of pre-supernova models. The beginning of carbon burning is also labelled in the graph as " ^{12}C ". The original figure is from (Maeder, 1981). See figure 2.1 for a comparison.

2.1.4 Rotation

Like the mass loss rate \dot{M} , rotational velocity v_{rot} also has a crucial effect on the stellar evolution. OB stars have large v_{rot} during their pre-main sequence and main sequence phases. The velocity decreases considerably by the time the star leaves the main sequence. Fast rotation may cause stars to lose a larger fraction of their mass M before even entering the post-main sequence phase. As the star loses mass, it also decreases its angular momentum (Meynet & Maeder, 2000; Maeder, 2009).

The rotation also causes mixing of material in the stellar interiors. It brings helium from the convective core into the radiative envelope, increasing its molecular weight. That increases temperature T in the core and brings new hydrogen from the envelope, thus enlarging the core. For a $20 M_{\odot}$ star with a $v_{\text{rot}} = 200 \text{ km s}^{-1}$ the core is enlarged by about 20 % by the end of the main sequence. The mixing of helium into the envelope also causes its opacity κ to decrease, which in turn increases the luminosity L , increasing the likelihood of a blue ward evolution. Consequently, this means that stars can be overluminous for their masses. The increased width of the main sequence can be seen in figure 2.3. Rotation increases the width of main sequence for $M < 40 M_{\odot}$ and decreases it above this limit (Maeder, 2009).

Main sequence durations of OB stars can be therefore increased by their fast rotation. The duration can be generally increased by 25 % at $9 M_{\odot}$ star and by 15 % at $120 M_{\odot}$ star (Meynet & Maeder, 2003).

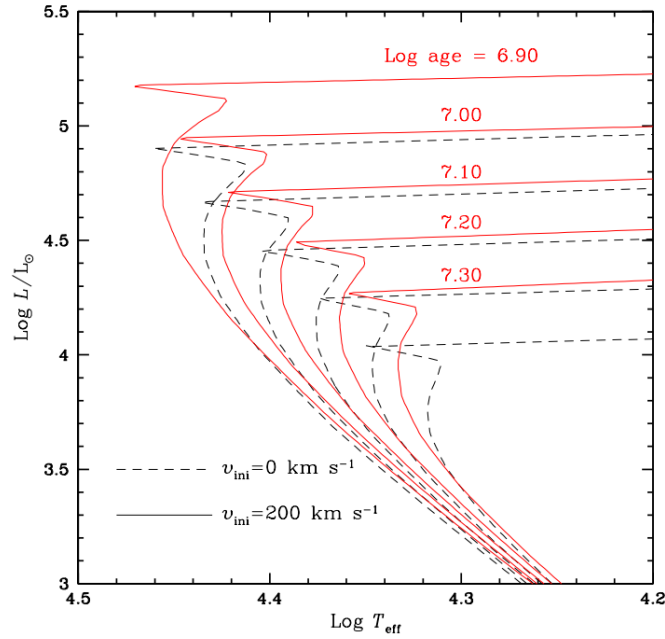


Figure 2.3: Stellar evolutionary isochrones computed for solar metallicity. Rotation enlarges the width of the main sequence. Taken from [Meynet & Maeder \(2000\)](#).

2.1.5 Chemical Abundance

Due to the dependency of mass loss rate \dot{M} (as in equations 2.4 and 2.5) and opacity κ on metallicity Z , the chemical abundance of massive stars plays an important role in their evolution as well. The metallicity Z may also slowly increase, because due to the mass loss rate, the massive stars lose outer layers, which consist primarily of hydrogen. Thus, for the higher values of metallicity Z a supergiant can become a WR star sooner.

In figure 2.4 we can see how the surface abundance evolves. Firstly, the initial abundances reflect the cosmic abundances. The abundance does not significantly change until the post-main sequence phase, because the star could not have lost enough of the envelope yet, and the first dredge-up has not occurred yet. Later, the He/H ratio starts to increase, as the hydrogen burning products appear at the stellar surface. The deviations from initial chemical composition are small because of a high dilution of CNO processed material in the large convective envelopes of red supergiants ([Maeder & Meynet, 1987](#)).

Once the shells of the fully intermediate convective zone appears at the surface due to the mass loss, the transitions become more discontinuous. Eventually, the majority of outer envelopes including unburned hydrogen is lost, and the helium becomes the most abundant element. At that point, the supergiant becomes a Wolf-Rayet star ([Maeder & Meynet, 1987](#)).

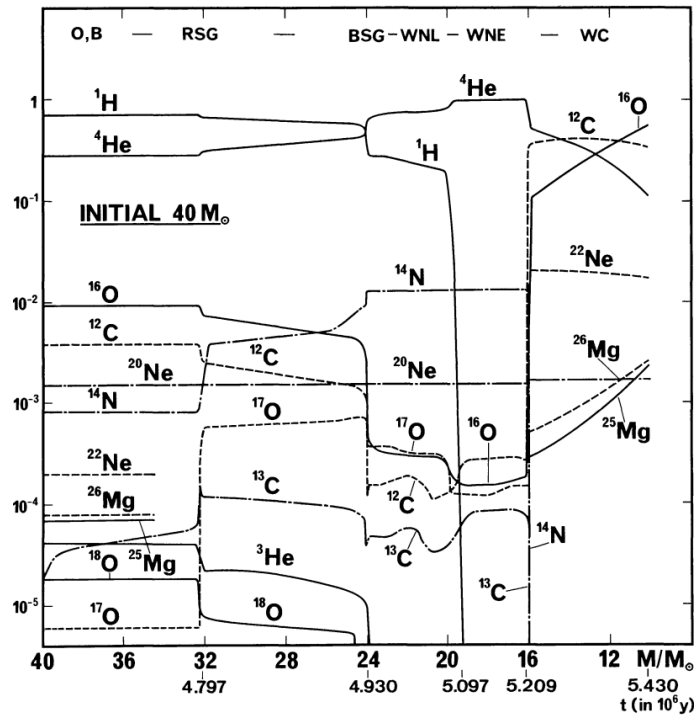


Figure 2.4: Evolution of surface abundance for an initial $40 M_{\odot}$ model as a function of the remaining mass and age. The evolutionary stages are indicated at the top of the figure. (Maeder & Meynet, 1987).

2.2 Betelgeuse

Betelgeuse is a semi-variable star and is the brightest star in the near-infrared part of spectrum (E2), typically ranking as one of the 10 brightest stars overall. It is classified as a red supergiant of M1–M2 spectral type (Keenan & McNeil, 1989).

2.2.1 History of Observation

Betelgeuse (spelled 'betəldʒu:z) is part of Orion constellation, in company with many other bright stars. Even though Rigel is brighter most of times, the name α Orionis in the end went to Betelgeuse and Rigel became β Orionis. Due to the Betelgeuse's extraordinary brightness, it has been observed since the ancient times. For that reason, the star was often one of the first targets for testing or using new technologies in astronomy. Betelgeuse's significant variability in brightness was therefore soon noticed. The first one to describe the variability was John F. W. Herschel, who published his first observations in his *Outlines of Astronomy* (1849). He continued to observe the star in the following decades and noticed that there is a shorter and a longer cycle of variability (Wilk, 1999). Many more observations followed, and the variability has been examined further.

Due to Betelgeuse's relative proximity and high brightness, it was picked as a first target for interferometric measurements by Michelson & Pease (1921), and they were able to determine the Betelgeuse's diameter R . The estimates of diameter were further improved

by [Bonneau & Labeyrie \(1973\)](#) with the invention of speckle interferometry.

As the technology continued to evolve, it was eventually possible to resolve first images of Betelgeuse, in infrared due to [Burns, Baldwin et al. \(1997\)](#), and in ultraviolet by Hubble Space Telescope ([Gilliland & Dupree, 1996](#)). Both observations also revealed a hot spot on the surface, which was believed to be one of the Betelgeuse’s rotational poles ([Buscher et al., 1990](#); [Uitenbroek et al., 1998](#)).

In more recent history, there were detected several dust and molecular shells surrounding Betelgeuse ([Kervella et al., 2018](#)).

2.2.2 Physical Characteristics

Despite many highest quality observations and research, several of the most fundamental characteristics of Betelgeuse remain significantly uncertain.

Parallax and Diameter

The largest uncertainty lies in the determination of the distance of Betelgeuse, even though it is relatively close to us. The results vary between 50–250 pc, as can be seen in table 2.3.

Reference	parallax π [mas]	distance d [pc]
Lambert et al. (1984)	-	155
Hipparcos ESA (1997)	7.63 ± 1.64	131^{+36}_{-23}
Tycho ESA (1997)	18.60 ± 3.60	54^{+13}_{-9}
Harper et al. (2008)	5.07 ± 1.10	197^{+45}_{-45}
Harper et al. (2017)	4.51 ± 0.80	222^{+48}_{-34}
Joyce et al. (2020)	$5.95^{+0.58}_{-0.85}$	168^{+27}_{-15}

Table 2.3: Summary of distance data for Betelgeuse. Adapted from [Dolan et al. \(2016\)](#).

There are several factors that contribute to this large uncertainty. First of all, the variability that is the subject of this thesis is due to Betelgeuse’s pulsations, therefore the actual diameter of the star does not have a stable value. Combining the fact that Betelgeuse is asymmetric with a large angular diameter [Dolan et al. \(2016\)](#), issues with defining the edge of the star, and that observations based on various parts of spectrum can give largely different results ([Gilliland & Dupree, 1996](#)), a wide uncertainty exists. For the last reason, the most accepted result has generally been considered the one by [Harper et al. \(2008\)](#) that yields $887 \pm 203 R_{\odot}$, as it has been derived from multi-wavelength observations. A new estimate by [Joyce et al. \(2020\)](#) was also released last year based on new data and combining several models that yield $764^{+116}_{-62} R_{\odot}$.

Mass and Mass Loss Rate

Similarly, the results of mass vary, although recent results are mostly in a relative accordance. Evolutionary models by [Dolan et al. \(2016\)](#) estimate the current mass M to be of $19.4\text{--}19.7 M_{\odot}$ and initial mass M in range of $20^{+5}_{-3} M_{\odot}$. The result by [Joyce et al. \(2020\)](#)

that combine evolutionary, asteroseismic, and hydrodynamical simulations, give a result of $16.5\text{--}19.0 M_{\odot}$ and initial mass M of $18\text{--}21 M_{\odot}$.

On the other hand, there is a relatively wide agreement for the current mass loss rate. Usually the mass loss rate \dot{M} is given roughly about $2_{-1}^{+1} \cdot 10^{-6} M_{\odot} \text{ yr}^{-1}$ (van Loon, 2012; Dolan et al., 2016; Joyce et al., 2020). Such a value is considered typical for red supergiants, according to van Loon (2012).

Motion and Rotation

Betelgeuse is considered a runaway star, moving with large proper motion of 30 km s^{-1} (van Loon, 2012) and average photospheric radial velocity $v_{\text{rad}} = 21.9 \text{ km s}^{-1}$ (Famaey et al., 2005). There have been issues with tracing Betelgeuse back to its origin, especially due to the uncertainty of the distance to the star. Using the higher distance values, such as the bottom ones in table 2.3, helps with resolving the issue, and the birthplace of the star can be likely placed into OB 1a association (van Loon, 2012).

Rotational velocity v_{rot} of Betelgeuse is higher than most other red supergiants typically have (van Loon, 2012). The inclination of 20° that was determined from HST ultraviolet image of Betelgeuse (Uitenbroek et al., 1998), gives a $v_{\text{rot}} \sim 15 \text{ km s}^{-1}$. As we have discussed in subsection 2.1.3, rotational velocity v_{rot} is instrumental in the evolution of a star. For Betelgeuse it means that it is older by up to $\sim 15\%$ and that it will lose less mass as RSG (van Loon, 2012). However, according to new study by Kervella et al. (2018) $v_{\text{rot}} \sin(i) = 5.47 \pm 0.25 \text{ km s}^{-1}$, it was determined that $i \sim 60^{\circ}$, yielding a rotational velocity $v_{\text{rot}} = 6.5_{-0.8}^{+4.1} \text{ km s}^{-1}$. Therefore Betelgeuse is not older by $\sim 15\%$, but less so.

Overall Evolution

According to van Loon (2012), Betelgeuse must have been a part of double-star system, likely in Orion OB 1a association. Betelgeuse's companion was a larger star, which caused its extraordinary rotational velocity. After the companion exploded, Betelgeuse was sent on its lone journey, with $v_{\text{rad}} \sim 35 \text{ km s}^{-1}$. It was a BSG at first, until it became a RSG about 10^4 years ago. It will continue to lose mass and cool down. Due to high v_{rot} it will likely manage to become a BSG for a short time once again, as it will still have enough mass. Eventually, it will explode as a supernova, likely of type IIb. Without rotation, the explosion would happen considerably earlier.

Currently, Betelgeuse is in the early core helium burning phase (Joyce et al., 2020).

To explain some of the Betelgeuse's peculiar behaviour it was suggested by Karovska et al. (1985) that it has one or two companions, but this has never been confirmed.

2.2.3 Variability

Betelgeuse's brightness changes by at least two different timescales (Joyce et al., 2020), observed since Herschell. Based on some of the most precise determinations of the periodicity Kiss et al. (2006) and Chatys et al. (2019), the shorter period is $P_{\text{short}} \sim 388 \pm 30$ days, and the longer period is $P_{\text{long}} \sim 5.6 \pm 1.1$ years (~ 2050 days). Both vary in the exact length and amplitude. The variations in magnitude m , radial velocity v_r and temperature T are visible in figure 2.5.

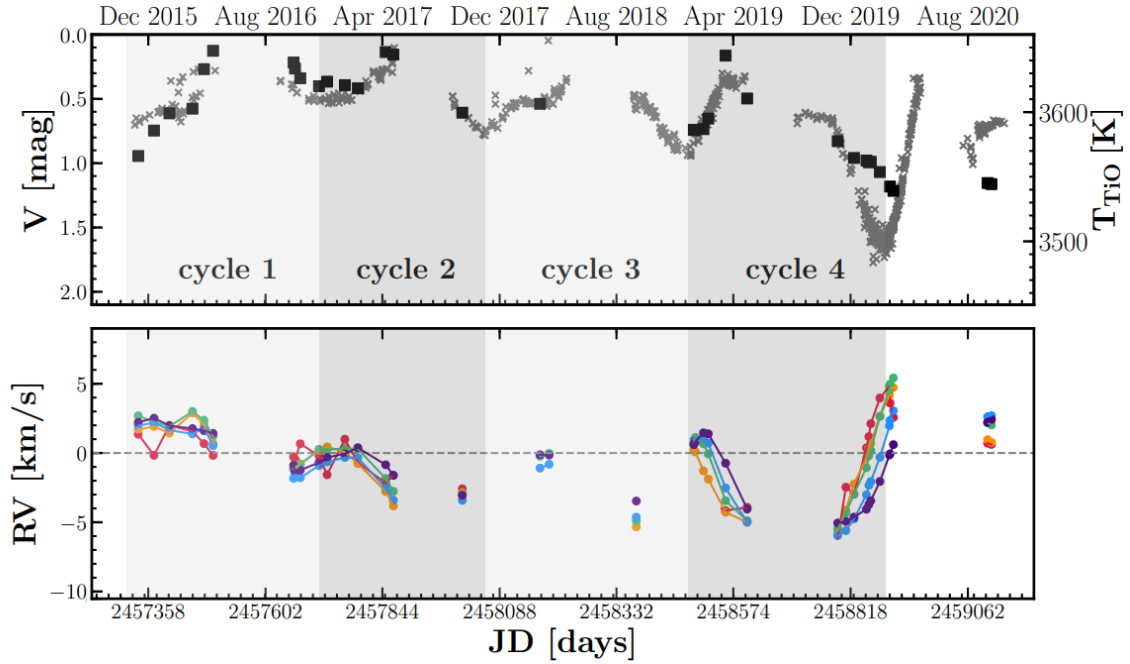


Figure 2.5: Comparison of long term evolution of radial velocities v_r , V magnitude and temperature determined from TiO bands T_{TiO} . Black squares correspond to T_{TiO} . The velocities were resolved by HERMES spectrograph, different colours correspond to various masks of cross-correlation functions. Includes the Great Dimming. Adapted from [Kravchenko et al. \(2021\)](#).

While there is no clear consensus, it is mostly assumed that the shorter period is driven by atmospheric pulsations in either the fundamental or low-overtone modes, and also by oscillations due to invocation of convective cells ([Kiss et al., 2006](#)). [Joyce et al. \(2020\)](#) concluded that the mode of atmospheric pulsations is the fundamental mode. The longer period is most often attributed to either flow timescales of giant convection cells ([Stothers, 2010](#)) or due to magnetic activity, rotation of starspots, episodic dust formation, or a nearby companion followed by a dust cloud ([Wood, 2000](#); [Wood et al., 2004](#)).

2.2.4 2019-2020 Dimming

In October 2019 Betelgeuse begun to decrease its brightness once again. However this time, the dimming continued much further than ever before, and it reached the historical minimum by the middle of February. The unprecedented event was nicknamed as The Great Dimming. The Dimming was first noticed by [Guinan et al. \(2019\)](#), who suggested that this dimming is due to confluence of the longer and shorter period. Betelgeuse had continued to dim until middle February, reaching a minimum of $V \sim 1.6$ mag. After that it appeared to increase its brightness again ([Guinan et al., 2020](#)). [Gehrz et al. \(2020\)](#) observed that the Betelgeuse's brightness in infrared was largely unaffected by the Great Dimming, whereas mostly the optical wavelengths were affected. Considering that Betelgeuse is the brightest in the infrared, it suggests that the overall brightness of Betelgeuse remained mostly intact. Therefore it seems unlikely that this episode would be due to major changes

within a star, but more likely due to a local surface event. In figure 2.6 we can see that Betelgeuse had dimmed asymmetrically.

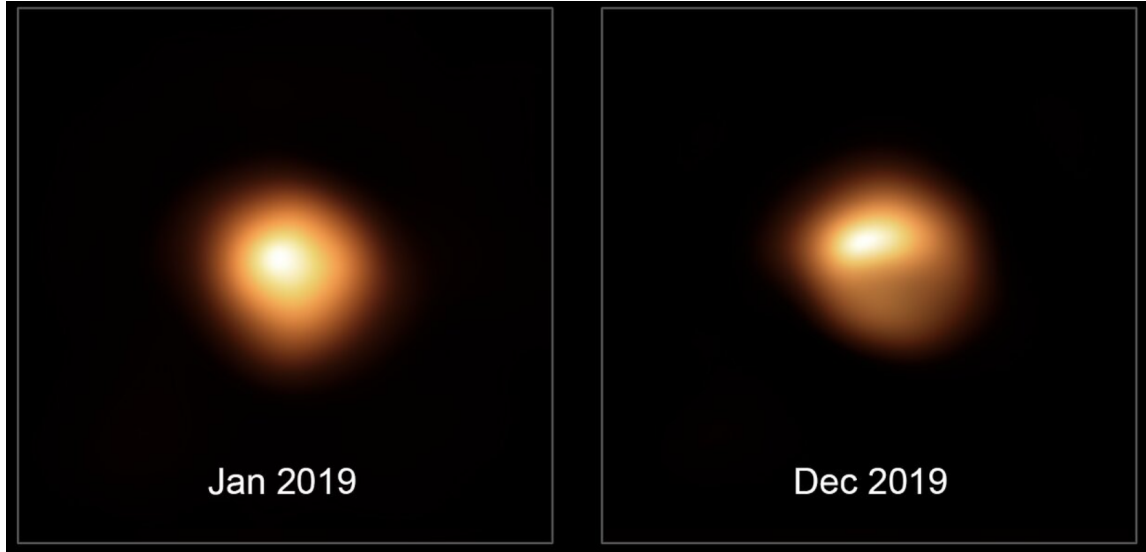


Figure 2.6: This comparison image shows Betelgeuse before and during the Great Dimming. It is visible that southern hemisphere had dimmed significantly. Taken from E3.

However, considering that such a dimming had never been observed before, the initial theory of a conjunction of the two periods did not seem to be the right explanation. Therefore several teams have been working on this issue, and suggested several possible solutions to explain this event.

Levesque & Massey (2020) argued the dimming episode could not have been caused by a decrease in Betelgeuse's T_{eff} , according to atmosphere models. Based on their the best fit, T_{eff} dropped only from 3650 K to 3600 K, which would be attributed to a decrease of visual magnitude $V \sim 0.17$ mag. That would definitely not be sufficient to explain the $V \sim 1.1$ mag drop in brightness. Therefore, they suggest that the decrease in V could be due to mass loss and subsequent large grain dust production that would cause an absorption, mostly in optical part of spectrum. Betelgeuse has several circumstellar shells and suffers asymmetric mass loss (Kervella et al., 2018). That would also explain the dimming of half of Betelgeuse, as seen in figure 2.6. However, Dharmawardena et al. (2020) found out the Betelgeuse has also dimmed in sub-millimetre wavelengths by about $\sim 20\%$ during the Great Dimming. They argue that a dust envelope would not have been able to cause the decrease in this part of spectrum, therefore directly opposing the model by Levesque & Massey (2020). They argue the Dimming must have been due to changes in the photosphere, as sub-millimetre wavelengths are primarily dominated by Betelgeuse's photosphere. Based on their models, they were able to present other possible causes that would explain the scope of the dimming. Either decrease in Betelgeuse's T_{eff} to 3450 K, or a significant surface activity through starspots. If 50 % of the surface was covered with $T_{\text{eff}} = 3250$ K spots, or 70 % of the surface with $T_{\text{eff}} = 3350$ K spots, that would also explain the The Great Dimming.

Dupree et al. (2020) managed to find a connecting link between most of the previous data. Based on the UV observations resolved by HST, they identified a hot structure that

had formed in Betelgeuse's southern hemisphere during the beginning of the Dimming. Due to a combination of two major effects, the expansion of photosphere as part of the pulsation period (see figure 2.7) and a convective upflow, the mass loss event was enhanced through an unprecedented powerful outflow. The resulting highly accelerated hot material would therefore be able cool down in a shorter time period. As the material cooled down, the dust opacity κ could increase quickly enough, which would explain the dimming of Betelgeuse's southern hemisphere.

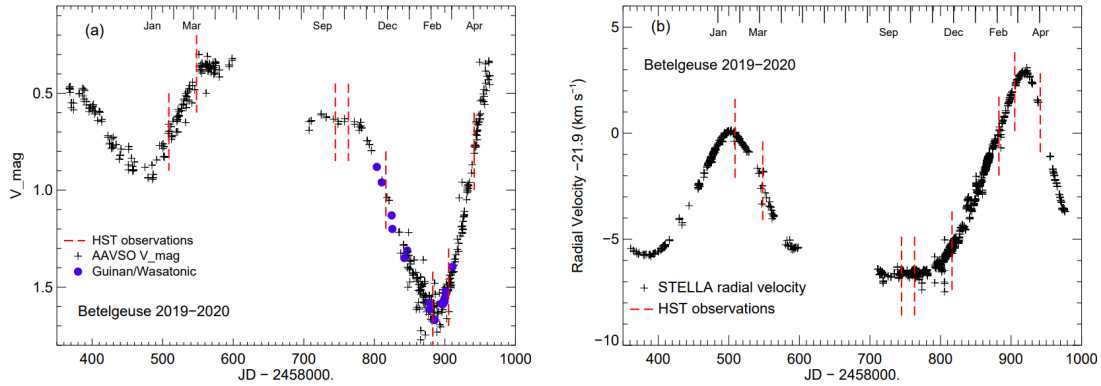


Figure 2.7: Figure comparing the variability of magnitude in filter V and radical velocity v_r during the Great Dimming. The radical velocity was resolved by STELLA optical spectrograph. The red broken lines indicates the times of HST spectral scans. Taken from (Dupree et al., 2020).

The irregularities in Betelgeuse's variability continued, as after it's initial rapid rise in brightness that restored Betelgeuse's usual values of brightness, it reached a secondary minimum at the beginning of August 2020. This minimum was attributed to an ejection of another dust cloud (Sigismondi et al., 2020).

Chapter 3

Stellar Spectroscopy

3.1 Formation of Spectrum

3.1.1 Continuous Spectrum

Within a gas that has very high temperature T (and thus also high kinetic energy E_k) and a high density ρ , thermal excitations through collisions and interactions are very frequent. A gas within the interior of stars is almost completely ionized plasma that interacts with photons primarily through processes of free-free and bound-free absorption and electron scattering. Free-free absorption means that a photon is absorbed by a free electron, and through an interaction with an adjacent atom or ion, the electron increases its energy. If an electron bound to an atom or ion absorbs a photon of a high enough energy, it may be removed from the atom or an ion, this process is called a bound-free absorption. Free electrons can also scatter photons in various directions, while the photons energies remain unchanged, which significantly increases the time needed for a photon to escape. Electrons can interact with photons of broad wavelength ranges through all these processes. Consequently, the light emitted from the star would appear as a continuous spectrum, referred to as the continuum ([Robinson, 2007](#); [Gray & Corbally, 2009](#)).

The spectrum of such light resembles a black body radiator. Such spectra, and especially their dependence on temperature T and wavelength λ , can be described using Planck's radiation law

$$I(\lambda) = B(\lambda, T) = \frac{2hc^2}{\lambda^5} \frac{1}{e^{\frac{hc}{\lambda kT}} - 1}. \quad (3.1)$$

This dependence means that with the increasing temperature T , the intensity peak moves towards lower wavelengths, hence towards the bluer colour, while the height of the peak also increases ([Chromey, 2010](#)).

To determine the intensity peak we can use Wien's Displacement Law

$$\lambda_{I_{\max}}(T) = \frac{b}{T}, \quad (3.2)$$

where b is Wien's constant ([Chromey, 2010](#)).

The stellar spectra form after photons go through major interactions in outer layers, such as bound-bound absorption, i.e., an electron bound to an atom absorbs a photon

and increases its energy. These outer layers are called the photosphere, which typically dominates the spectra. The chromosphere may also contribute to the spectra in cooler stars (Gray & Corbally, 2009).

3.1.2 Absorption Lines

When the light from a stellar core shines through a cooler thin body of gas, the photons are absorbed within a given line when the difference between its energy levels are equal to difference of energy levels in the atoms of the gas. The atoms in the gas absorb photons of specific wavelengths and the atoms become excited. However, the atom quickly emits another photon, to return itself to a lower energy level, or it may also de-excite itself by a collision. As the temperature is lower in these layers, we observe less photons at these wavelengths and there are dark lines in their place, or a decreased intensity. Those lines were created by the absorption, and are called absorption lines. Typically, they are formed when the light passes through diffuse outer layers of a star, that are cooler and less dense, i.e., stellar atmospheres, revealing of which elements do these layers consists of (Trypsteen & Walker, 2017).

3.1.3 Emission Lines

If a diffuse, low-density, cloud of gas is heated up by a nearby source, the electrons in the atoms in the cloud can get excited to higher energy levels either through thermal excitation or photons of matching wavelengths. The atoms may also become ionized, when the energy is high enough to release electrons. When they eventually recombine or fall back to lower energy levels, they emit a photon of specific wavelengths corresponding to the difference in energy levels. Therefore we can observe emission peaks at specific wavelengths. At higher temperatures T , we can observe higher levels of excitation and higher ionization states of an atom. The emission lines are typically formed at envelopes that surround very hot stars, or ionized nebulae in the proximity of hot stars (Trypsteen & Walker, 2017).

3.1.4 Spectral Classes of Stars

Based on stellar spectra we can divide stars into spectral classes. The commonly used is Morgan-Keenan (MK) system by Morgan et al. (1943), that distributed stars into 7 classes O, B, A, F, G, K, M, as is shown in table 3.1. The spectral sequence reflects mostly the effective temperature T_{eff} of stars. O stars are the ones with the highest temperature (the bluest), while M stars are the ones with lowest temperature (the orange/red), although later were also added spectral types L and T for even cooler objects. Each class is also subdivided into 0-9 subclasses, where 0 corresponds to the hottest, and 9 the coolest subclass.

The spectral classes on their own however cannot distinguish between stars of the same temperatures T , but largely different luminosities L . Therefore the MK system also includes luminosity classes, as is shown in table 3.2.

Eventually, new types of stars were discovered that did not fit into any of the pre-existing classes, e.g., L stars, i.e., the coolest and smallest main-sequence stars, called

Spectral Class	Temperature T_{eff} [K]	Spectral Features
O	≥ 28000	weak B, ionised He, strong UV continuum
B	10000 – 28000	medium B, neutral He lines
A	7500 – 10000	strong B, strong H lines, ionised metal lines
F	6000 – 7500	medium B, weak ionised Ca
G	4900 – 6000	weak B, ionised Ca, metal lines
K	3500 – 4900	very w. B, Ca, Fe, strong molecules, CH, CN
M	2000 – 3500	very w. B, molecular lines, neutral metals

Table 3.1: The Morgan-Keenan spectral system. B is an abbreviation for Balmer hydrogen lines, w. for weak. Adapted from [E1](#).

Symbol	Class of a Star
Ia	Luminous supergiants
Ib	Less luminous supergiants
II	Bright giants
III	Normal giants
IV	Subgiants
V	Main sequence
sd	Subdwarfs
wd	White dwarfs

Table 3.2: Luminosity Classes of Stars. Betelgeuse has luminosity class Iab, which means that it is between classes Ia and Ib. Adapted from [E1](#).

brown dwarfs, WR (Wolf-Rayet) stars, i.e., stars that were originally O stars, but lost significant part of their envelope, hence the core is partially revealed, and C stars, i.e., giants that have significant carbon lines ([Gray & Corbally, 2009](#)).

3.2 Spectral Lines

Every spectral line has its own line width. However, due to Heisenberg's uncertainty principle, energies of photons emitted during the transitions of electrons between energy levels in atoms are not strictly defined, therefore also the wavelength of a spectral line does not have only one value. The quantity that describes the spreading of photon energies is called a natural line width ([Chromey, 2010](#); [Krtićka, 2015](#)).

If a profile of a spectral lines in a spectrum is given by thermal Doppler broadening (Gauss function) and collisional broadening (Lorentzian profile), the profile is described by the Voigt function. Voigt function is a convolution of Gauss and Lorentzian profiles,

and is given by

$$\phi(\nu) = \frac{1}{\sqrt{\pi}\Delta\nu_D} \frac{\Gamma}{4\pi^2} \int_{-\infty}^{+\infty} \frac{\exp\left[-\frac{(\nu'-\nu_0)^2}{\nu_D^2}\right]}{(\nu-\nu')^2 + \left(\frac{\Gamma}{4\pi^2}\right)^2} d\nu', \quad (3.3)$$

where ν_0 is the frequency of the centre of the line, Γ is a parameter related to the width of the line, $\Delta\nu_D$ is a Doppler width (Krtićka, 2015). Doppler width $\Delta\nu_D$ of the line profile is given by

$$\Delta\nu_D(T, m) = v_M \frac{\nu_0}{c} = \sqrt{\frac{2kT}{m}} \frac{\nu_0}{c}, \quad (3.4)$$

where v_M is the most probable speed based on the Maxwell distribution. It describes an average value of velocity proportional to the temperature of atoms in gas (Robinson, 2007). The profile of spectral lines in stellar spectra may be significantly affected by processes within a star. Therefore, based on analysing the profiles of spectral lines, we are able to discover fundamental information about the star.

3.2.1 Radial Velocity

Based on Doppler Effect

$$\frac{v_r}{c} = \frac{\Delta\lambda}{\lambda_0} = \frac{(\lambda' - \lambda_0)}{\lambda_0}, \quad (3.5)$$

if an object is moving closer or further towards an observer, the spectral lines in the object's emitted spectrum will be shifted (Chromey, 2010). If the object is moving towards an observer, the wavelengths of spectral lines will be shifted to smaller wavelengths. On the other hand, if the object is moving away from us, the wavelengths of spectral lines will appear to be at longer wavelengths (Chromey, 2010).

Therefore, by measuring wavelengths of spectral lines and comparing them to laboratory values λ_0 , we are able to determine a radial velocity v_r of a star based on the shift. Radial velocity v_r tells us whether a star is moving towards or further from us along our line of sight (Chromey, 2010).

To be able to determine the shift properly, it is also necessary to do a heliocentric correction, i.e., removing the velocity due to the motions of Earth in its orbit around the Sun. Amplitude of these velocities is up to $\sim 30 \text{ km s}^{-1}$. For more precise measurements, it is also necessary to remove other motions, such as the ones caused by rotation or Moon (Trypsteen & Walker, 2017). If an observation was made aboard a space satellite, it is also necessary to correct the shift by satellite's velocity.

3.2.2 Rotational Velocity

If a star is rotating, part of its surface may be moving towards or further from us, relative to v_r . That causes rotational broadening of spectral line profiles, i.e., blue and red wings (Robinson, 2007). Whether and to what extent will we observe the rotational effects does not depend only on rotational equatorial velocity v_{rot} of a star, but it also depends on an inclination i of a star. Inclination i is an angle between a rotational axis of a star and our

line of sight. If the rotational axis is pointed at us, then $i = 0^\circ$ and we do not observe any rotational broadening, because the rotational motion does not happen along our line of sight. Whereas, if the rotational axis is perpendicular towards our line of sight, we observe the rotational effects in full strength. Therefore, we generally do not determine v_{rot} , but it's projection $v_{\text{rot}} \sin(i)$ (E1).

3.2.3 Temperature and Gravitational Acceleration

It is possible to determine surface effective temperature T_{eff} and gravitational acceleration g by fitting two sets of spectral lines, one set depending mostly on T_{eff} and other mostly on g (Krtićka, 2015). By directly comparing an observed spectrum with a spectrum of a known star of a similar type, we are also able to determine temperature. We model a spectrum and fit it's parameters, until it correspond to the observed spectrum of a star (Trypsteen & Walker, 2017).

3.2.4 Density of Outer Layers

The width and depth of spectral lines also give us information about the density of outer layers of a star, as that is where the absorption takes place. The lower the density ρ , the narrower the lines are, e.g., in red supergiants due to their large diameter R . When the density is high, the profiles of spectral lines are broadened, e.g., white dwarfs M (E1).

3.2.5 Chemical Composition

Based on specific spectral lines in a spectrum, it's possible to determine the presence of a chemical element in a star, but mainly also the amount of a specific element relative to other, typically relative to hydrogen H. Hence, it is possible to determine an abundance of a heavier element relative to H. Metallicity Z is the fraction of mass of all elements heavier than He, relative to H, within a star (Krtićka, 2015).

Chapter 4

Spectral and Photometric Analysis of Betelgeuse

4.1 Spectroscopy

To analyse spectral features of Betelgeuse, all data from available spectral archives were used. Most of the spectra were obtained by SSAP servers search function in Starlink SPLAT-VO: A spectral analysis tool ([Castro-Neves & Draper, 2014](#)), although some were also obtained from other archives. SPLAT-VO was also used as the main tool to analyse the spectra, and is freely available at [E4](#).

4.1.1 Spectral Analysis

It was first necessary to find high-quality spectra, as there are many that do not have sufficient quality for analysis of specific lines. Afterwards, the spectra had to be normalized, accomplished by dividing the spectra by an interpolated spectrum of continuum, using a "Spectrum from interpolation" function.

Once the spectrum is normalized, we are able to fit spectral lines that we choose and extract the needed parameters, using the "Fit lines" function. It is necessary to manually find and select the spectral lines that we want to fit. The function "Save line extents" and "Read line extents" was very useful, as it allowed me to save the positions of my spectral lines, and hence I was able to easily find them in other spectra. From the available fits, I was using Voigt profile to fit spectral lines (see equation [3.3](#)). It is possible to save the lines fits into a file. An example of the fitting process is shown in figure [4.1](#).

Apart from many other parameters, the fit most importantly provides a core of a spectral line, i.e., the wavelength λ' of the center of a spectral line. That allows us to compare it to the laboratory wavelength λ_0 of each spectral line from our fit, and based on that, to determine the wavelength shift $\Delta\lambda$ of a spectral line. We are able to find a radial velocity shift v_r of each line in km s^{-1} by using the equation [3.5](#). For a precise measurement of spectral lines, an instrument used needs to have a high enough resolution R . It is the smallest possible wavelength interval that a spectrograph can distinguish, and is given by

$$R = \frac{\lambda}{\Delta\lambda}, \quad (4.1)$$

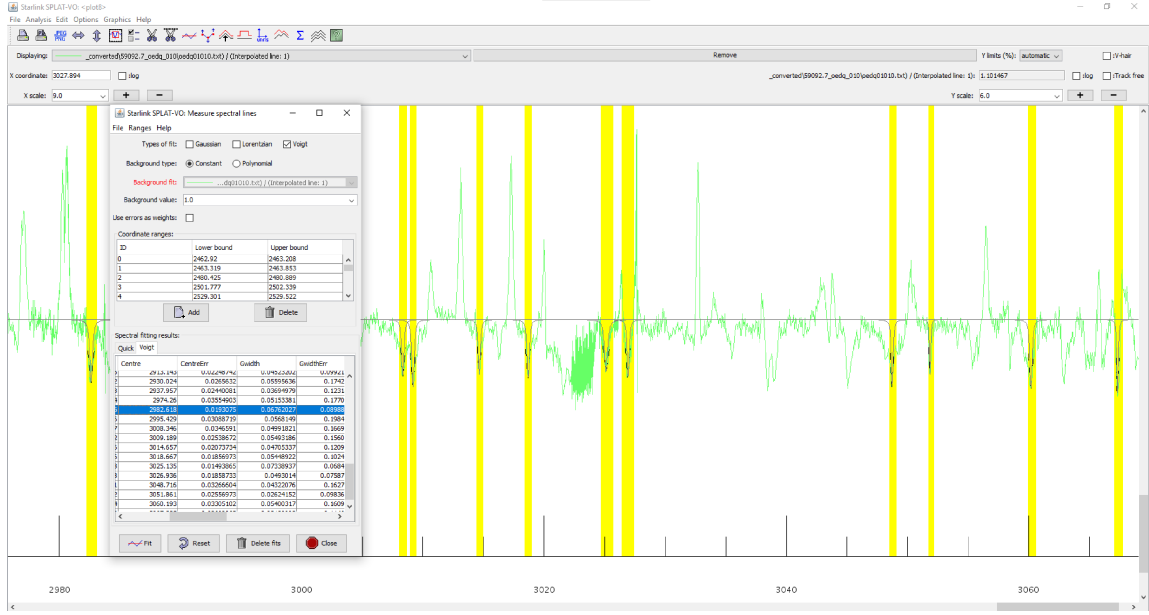


Figure 4.1: Results of Voigt fit in SPLAT-VO. Each marked line is fitted, and the results of the fit can be saved.

where $\Delta\lambda$ is the wavelength interval at a wavelength λ (Trypsteen & Walker, 2017).

Radial velocities of individual spectral lines may differ to a certain degree, therefore it is necessary to use a large number of spectral lines and statistically find the average v_r .

The most fundamental part is to find suitable spectral lines for the analysis. For a given spectrum, the amount of spectral lines present can vary, as well as their profiles. Sometimes they may be blended with other lines as well. This is exceptionally difficult in stars of spectral class M (or cooler), because they are somewhat far away from an ideal black body radiator, and there are many more lines present, including molecular bands. Therefore, the essential part is to correctly identify spectral lines in each spectrum, as possibly using wrong lines may cause false results. The lines that were used in this thesis are listed in the following sections. About 120 lines were used in total. The original number of lines was higher, but many of those additional lines were not used, due to various issues with identification, asymmetric line profiles and blending with other lines. In general, such issues revealed themselves as systemic wrong results of radial velocity.

To describe wavelength λ , I am using an unit of angstroms. 1 \AA is equal to 10^{-10} m . To describe date, I am using a Modified Julian Date (MJD). MJD is converted from Julian date, and is given by $\text{MJD} = \text{JD} - 2400000.5$. Julian date is the number of days since the noon on January 1, 4713 B.C. The uncertainties σ of results in this thesis were determined using standard deviation, unless stated otherwise.

4.1.2 Optical Spectra

For the optical part of spectrum, there are available many high-quality spectra, resolved by some of the most technologically advanced ground based telescopes. As all the spectra include a wide range of wavelengths, it was possible to use one set of spectral lines to

identify the lines in all the spectra. The used spectral lines are listed in table 4.1.

	λ_0 [Å]		λ_0 [Å]		λ_0 [Å]
Ca II	3933.660	Ca I	4226.730	Fe I	5079.740
Ca II	3968.470	V I	4234.000	Mg I	5167.322
Ti I	4024.571	Cr I	4254.352	Mg I	5183.604
Mn I	4030.760	V I	4259.309	Fe I	5371.489
Mn I	4033.070	Fe I	4271.760	Fe I	5405.775
Mn I	4034.490	Cr I	4274.812	Fe I	5429.696
Fe I	4045.812	Cr I	4289.731	Ni I	5476.910
Fe I	4063.594	H γ	4340.470	Na I	5889.951
Fe I	4071.738	Fe I	4383.550	Na I	5895.924
Sr II	4077.714	Fe I	4466.551	Fe I	6400.318
H δ	4101.734	Fe I	4482.169	Ti I	6413.102
Fe I	4132.058	Fe I	4489.739	Fe I	6421.351
Fe I	4134.420	Ti II	4501.270	Fe I	6430.846
Fe I	4143.868	Ti I	4512.734	Ca I	6455.600
Fe I	4181.755	Ti I	4522.797	Ca I	6462.570
Fe I	4187.039	H β	4861.297	Fe I	6469.123
V I	4190.726	Fe I	4920.503	Ca I	6471.662
V I	4191.516	Ba II	4934.077	H α	6562.772
Fe I	4199.095				

Table 4.1: Spectral lines used to analyse optical part of the available spectra. These lines were present in every spectrum. The wavelengths λ_0 are laboratory values in air. The lines were taken from E5. Additional ones from Fekel (2003), originally for determination of rotational velocities. The exact values of all the lines were taken from E5. The spectral lines are labelled in a spectrum in Appendix III and Appendix IV.

All the used spectra had a very high signal to noise ratio (SNR), higher than 150, in some cases even reaching 600. There were often available more than one sub exposure from the same observation. In such cases, I used the one with the highest SNR.

Below, I describe the individual sources of the spectra used in this thesis.

HARPS

High Accuracy Radial velocity Planet Searcher (HARPS) is European Southern Observatory's (ESO) echelle spectrograph, mounted on the La Silla 3.6m telescope in Chile. In order to primarily hunt exoplanets, it's radial velocity accuracy is one of the highest currently available, and has a resolution of 115 000 (Mayor et al., 2003).

ID	MJD [d]	λ [Å]	SNR	t_{exp} [s]	R
ADP.2020-02-13T01:08:03.105	58891.06	3781.5-6912.3	150	10	115000

Table 4.2: Index of HARPS spectra that were used in this thesis. Available at E6.

UVES

Ultraviolet and Visual Echelle Spectrograph (UVES) is ESO's spectrograph mounted on 8.2m Very Large Telescope (VLT) in Paranal in Chile. The light beam is divided into two arms, a blue and a red one. It has a maximum resolution of 80 000 in the blue arm, and 110 000 in the red arm ([Dekker et al., 2000](#)).

ID	MJD [d]	λ [Å]	SNR	t_{exp} [s]	R
ADP.2020-08-10T17:58:05.098	52530.42	3731.0-4999.0	340	5	65030
ADP.2020-06-15T10:09:57.651	56570.38	3281.9-4563.0	160	10	71050

Table 4.3: Index of UVES spectra that were used in this thesis. The sub exposures covering the rest of optical region are available as well, but the data were damaged, therefore I was not able to use them. Available at [E6](#).

X-shooter

X-shooter is ESO's wide band spectrograph mounted on VLT. It has three independent arms of echelle spectrographs. The maximum resolution is about 18 000, depending on the arm ([Vernet et al., 2011](#)).

ID	MJD [d]	λ [Å]	SNR	t_{exp} [s]	R
ADP.2020-09-25T13:19:59.217	55166.34	2993-10186	90	0.6	10532

Table 4.4: Index of X-shooter spectra that were used in this thesis. Available at [E6](#).

SOPHIE

Spectrographe pour l'Observation des Phénomènes des Intérieurs stellaires et des Exoplanètes (SOPHIE) is an echelle spectrograph mounted on 1.93m telescope of Haute-Provence Observatory in France. It covers most of the optical spectrum, with resolution up to 75 000 in a high resolution mode ([Perruchot et al., 2008](#)).

ID	MJD [d]	λ [Å]	SNR	t_{exp} [s]
19223	54074.01	4000-6800	160	20.0

Table 4.5: Index of SOPHIE spectra that were used in this thesis. I was not able to retrieve information about R . Available at [E7](#).

ELODIE

ELODIE was an optical echelle spectrograph mounted on 1.93m telescope of Haute-Provence Observatory. It's resolution was able to reach up to 45 000 ([Baranne et al., 1996](#)). It was decommissioned in 2006.

ID	MJD [d]	λ [Å]	SNR	t_{exp} [s]
19990126/0017	51204.90	4000-6800	690	300.38
20030821/0027	52873.14	4000-6800	400	120.12
20030916/0033	52889.16	4000-6800	210	10.27
20031109/0011	52953.09	4000-6800	220	30.27
20040213/0010	53048.90	4000-6800	290	20.26
20040426/0025	53121.81	4000-6800	200	45.26
20040826/0048	53244.16	4000-6800	210	15.27
20050203/0010	53404.90	4000-6800	180	10.27

Table 4.6: Index of ELODIE spectra that were used in this thesis. I was not able to retrieve information about R . Available at [E8](#).

FLASH HEROS

Heidelberg Extended Range Optical Spectrograph (HEROS) is an upgrade to FLASH spectrograph, and both the spectrographs were developed at Landessternwarte Heidelberg in Germany. They are echelle spectrographs and were mounted at several telescopes, including at La Silla. Its resolution can reach up to 20 000 ([Kaufer, 1998](#)). The spectra were taken in years 1995 and 1997, in both cases the spectrograph was mounted on the La Silla telescope.

ID	MJD [d]	λ [Å]
f2546	49868.95	3442.0-5592.5
f2546	49868.96	5774.7-8632.4
f0176	50455.19	3389.4-5743.8
f0177	50455.19	5836.2-8628.4

Table 4.7: Index of FLASH/HEROS spectra that were used in this thesis. I was not able to retrieve information about R and t_{exp} . Available at [E9](#).

4.1.3 UV spectra

Analysis of ultraviolet spectra turned out to be more difficult, due to fact that the number of the archived spectra was high, while they mostly had lower quality. That is true mainly for older spectrographs, whose SNR usually reaches only up to 40. On the other hand, the newer STIS data are major part of this thesis, as they have high quality and cover larger timescales, but it was necessary to convert the data from the original non-linear format.

The UV spectra that I used in this thesis were often captured in relatively narrow wavelength windows, compared to the optical spectra, therefore it was often not possible to use the same list of spectral lines in every UV spectra. Table 4.8 shows a list of all spectral lines across the UV range that were used. All the lines are in near ultraviolet region (NUV).

From the older data, I used only GHRS (see below). In another major source, International Ultraviolet Explorer (IUE), I was not able to find spectra with sufficient quality.

	λ_0 [Å]		λ_0 [Å]		λ_0 [Å]
Fe II*	2399.971	Fe I	2606.435	Fe II	2747.794
Fe II*	2411.252	Fe II	2607.866	Fe II*	2756.551
Fe II*	2411.800	Fe II	2629.077	Fe II*	2760.149
Fe II*	2414.044	Fe I*	2637.264	Fe II*	2769.752
Fe I	2462.926	Fe I	2648.346	Mg II*	2796.352
Fe I	2463.392	Cr II*	2664.211	Fe II	2881.601
Fe I	2480.525	Cr II*	2673.622	Fe II	2905.224
Fe II	2501.886	V II	2679.320	Fe I	2913.010
Si I	2529.269	V II	2680.112	Fe I	2929.864
Fe II	2529.837	Cr II	2680.683	Fe I	2937.762
Fe I**	2530.320	Fe I**	2681.249	Fe I	2974.103
Fe II	2534.389	V II	2688.750	Fe I	2982.315
Ti II	2535.381	V II	2689.507	Fe I	2995.300
Fe II	2541.735	Cr II*	2690.004	Fe I	3008.159
Fe II	2567.682	Fe II*	2693.633	Fe I	3009.015
Mn II	2576.875	V II*	2701.729	Fe I	3018.506
Fe II	2578.693	Fe II*	2706.881	Fe I	3024.913
Fe II	2583.356	Fe I*	2707.384	Fe I	3026.723
Fe II	2586.649	Fe II*	2733.257	Fe I	3048.491
Mn II	2594.497	Fe II	2744.008	Ni I	3051.710
Fe II	2599.146	Fe I**	2744.879	Fe I	3059.975
Fe II	2600.172	Fe II	2747.296	Ti II	3067.109

Table 4.8: Spectral lines used to analyse near ultraviolet spectra. Due to narrow spectral ranges, some of them were not present in every spectra. The lines with * were only used at some spectra with different wavelength range than the main wavelength range of STIS. The lines with ** exhibited significant variability, i.e., at some spectra their profile was largely variable, sometimes barely present at all. λ_0 are laboratory values in vacuum. Lines picked based on [Brandt \(1995\)](#), precise values taken from [E5](#). The spectral lines are labelled in a spectrum in [Appendix II](#).

HST GHRS

The Goddard High-Resolution Spectrograph was one of the instruments mounted at HST. It's resolution reached up to 80 000. The spectrograph was removed from HST in 1997. However, the quality of publicly available spectra for Betelgeuse was often not high enough for radial velocities analysis. Fortunately, [Brandt \(1995\)](#) constructed an ultraviolet atlas of Betelgeuse, consisting of higher-quality calibrated GHRS spectra from year 1992.

HST STIS

Space Telescope Imaging Spectrograph (STIS) is an echelle spectrograph that was installed to HST in 1997. After a malfunction, it was repaired in 2009 and has worked reliably ever since. It has a wide spectral range, from ultraviolet to infrared part of the spectrum, and numerous functions. In ultraviolet part of the spectrum, it is able to provide high spatial

ID	MJD start [d]	MJD end [d]	λ [Å]	SNR	t_{exp} [s]
ZOYL01	48889.125	48889.667	1979-3300	≤ 30	598-707

Table 4.9: The GHRS spectra that were used are part of an atlas by [Brandt \(1995\)](#). The atlas includes about 20 sub exposure, all starting with ZOYL01. As they all are part of the same set of observations, hence taken in the same day, and each covers a range of only about 50 Å, I did not list them. MJD corresponds to the first and last dataset in the set of observations. Unlike other ultraviolet spectra, the wavelengths in these calibrated data are in air. Available at [E10](#).

quality spectroscopy with resolution of $\sim 114\,000$. The data that I used were resolved mostly in E230M grating mode that provides a resolution of about 30 000. As the aperture slit that was used for Betelgeuse does not cover the whole surface of Betelgeuse (the slit has 25x100 mas), in each dataset there are usually available several subexposures from different positions across Betelgeuse ([Dupree et al., 2020](#)), as can be seen in figure 4.4.

STIS archive has dozens of Betelgeuse spectra, including ones during the Great Dimming. Furthermore, a significant portion of earlier data is available through the Advanced Spectral Library Project (ASTRAL) ([E11](#)). The ASTRAL archive aims to create high-quality spectra, therefore they cleaned the data and combined sub exposures in order to obtain higher quality ([Ayres, 2014](#)). The spectra from ASTRAL that I used are listed in table 4.10.

Unlike other echelle spectra used in this thesis, STIS data are not publicly available in a linear format, i.e., a dependency of flux on wavelength, but only in the original **x1d** format, where it is also dependant on a spectral order (see figure 4.2). Therefore they are non-linear and cannot be analysed in SPLAT-VO in it's default format. Nonetheless, the spectra that are part of ASTRAL library are already converted to the linear format.

The earlier (ASTRAL) spectra consist of smaller ranges of wavelengths, but it covers all the parts of UV spectra, Far and Near, while the newer data (non ASTRAL) all use one joint slightly wider wavelength range, covering only NUV. So for newer data it was possible to use one set of spectral lines (table 4.8). ASTRAL covers the spectra from the first decade of this century, cca 1998–2011. I used most of the available spectra. I did not use some of those that covered the same dates. If that was the case, then I picked the ones with higher SNR, but the main deciding factor was whether a spectrum had the same wavelength range, so that I would be able to use my set of spectral lines. In each set of older observations, STIS almost always captured at least one spectrum that covers the wavelength interval of about 2400–3100 Å, while there were additional ones from FUV, so for a given date I was mostly able to use my set of NUV wavelength lines. For that reasons, most of FUV spectra in the older data were not used.

Regarding ASTRAL data, only stage 0 spectra were used, therefore those spectra that were cleaned and converted to a linear spectrum, but were not yet combined with other spectra, to make sure the information about the period is not lost. ASTRAL spectra includes most subexposures from datasets with prefixes **o4de**, **o6lx** and **obkk**.

The numerous remaining STIS spectra from the second decade are not (yet) covered by ASTRAL, therefore I had to invent my own method of converting the spectra into a linear 1-d format. I used a python script to accomplish that.

ID	MJD [d]	λ [Å]	SNR	t_{exp} [s]
o4de03040	50821.440	2280-3118	20	380
o4de03050	50821.446	2280-3118	20	280
o4de03060	50821.451	2280-3118	20	380
o4de05040	50904.660	2280-3118	20	380
o4de05050	50904.666	2280-3118	20	280
o4de05060	50904.671	2280-3118	20	380
o4de07040	51077.176	2280-3118	20	425
o4de07050	51077.182	2280-3118	20	336
o4de07060	51077.186	2280-3118	20	456
o4de09040	51265.299	2280-3118	20	456
o4de09050	51265.305	2280-3118	20	336
o4de09060	51265.310	2280-3118	20	456
o6lx01020	52561.570	2280-3118	20	283
o6lx02060	52700.574	2280-3118	20	300
o6lx03060	52752.538	2280-3118	20	300
obkk72010	55600.338	2378-2650	30	1854
obkk72020	55600.391	2621-2887	50	2850
obkk71020	55606.115	2378-2650	30	2850
obkk73010	55615.846	2621-2887	50	1854
obkk74010	55617.910	2280-3118	110	1862
obkk74020	55617.962	2378-2650	30	2850
obkk76020	55652.376	2378-2650	30	2850

Table 4.10: HST STIS ASTRAL data that were used. I will be referring to these data as HST ASTRAL. Available at [E11](#).

The python script that I used is shown in appendix. The figure in [Appendix V](#) shows how to view and work with the default non-linear spectra (such spectra have **x1d** extension). Using stistools python package from STSCI one could work with the spectra further.

My own method of converting the **x1d** spectra is shown in [Appendix VI](#). The script returns a .txt file that includes wavelength, flux and error and can be analysed in SPLAT-VO similarly as other spectra. The spectra have not been properly cleaned, especially when compared to ASTRAL spectra, but for the purposes of analysing only specific spectral lines that I picked for determination of radial velocities v_r , it is suitable.

All the datasets from HST STIS that I used are listed in table [4.11](#). It includes datasets with prefixes **odxg**, **oe1i** and **oedq**. Some **oedq** data from the last year are still to be released.

STIS spectra are captured at different positions towards the centre of Betelgeuse (figure [4.4](#)), scanning from an edge of Betelgeuse to the other edge, through it's centre. Most datasets include 7 scans (010-070), but for the purposes of this thesis I did not need to use all the subexposures. In the newer data I aimed to use 3 subexposures, the ones from the edges (010 and 070) and the centre (040). In the older ASTRAL data, mostly data available for the given wavelength range was used, generally corresponding to 040, 050, and 060. However, in many cases some sub exposures were not available, so I sometimes could not have used the same subexposures, or I had to use other ones.

ID	MJD [d]	λ [Å]	SNR	t_{exp} [s]	δ ["]
odxg01010	58508.246	2274-3072	50	1337	28.78
odxg01040	58508.311	2274-3072	30	372	25.74
odxg01070	58508.361	2274-3072	50	2813	25.70
odxg02010	58547.508	2274-3072	50	1337	25.79
odxg02040	58547.572	2274-3072	30	372	25.74
odxg02070	58547.623	2274-3072	50	2813	25.69
odxg06010	58573.061	2274-3072	60	1337	25.80
odxg03010	58591.272	2274-3072	50	1337	25.80
odxg03040	58591.337	2274-3072	50	372	25.74
odxg03070	58591.388	2274-3072	50	2813	25.68
odxg04010	58714.684	2274-3072	40	1337	25.70
odxg04070	58714.799	2274-3072	60	2813	25.79
odxg07010	58744.261	2274-3072	50	1337	25.69
odxg07040	58744.327	2274-3072	40	372	25.75
odxg07070	58744.393	2274-3072	60	2813	25.80
odxg08010	58762.749	2274-3072	50	1337	25.69
odxg08040	58762.812	2274-3072	40	372	25.75
odxg08070	58762.863	2274-3072	50	2813	25.80
oeli01010	58815.582	2274-3072	50	1277	25.67
oeli01040	58815.643	2274-3072	40	372	25.75
oeli01070	58815.704	2274-3072	40	1277	25.82
oeli02010	58866.560	2274-3072	50	1277	25.76
oeli52010	58882.318	2274-3072	50	1277	25.79
oeli52040	58882.381	2274-3072	40	372	25.75
oeli52070	58882.435	2274-3072	30	1277	25.71
oeli03010	58904.761	2274-3072	60	1277	25.80
oeli03040	58904.823	2274-3072	30	372	25.75
oeli03070	58904.878	2274-3072	30	1277	25.70
oeli04010	58940.975	2274-3072	50	1277	25.81
oeli04040	58941.037	2274-3072	30	372	25.75
oeli04070	58940.091	2274-3072	30	1277	25.69
oedq01010	59092.704	2274-3072	50	1277	25.71
oedq01040	59092.766	2274-3072	40	354	25.76
oedq01070	59092.820	2274-3072	30	1150	25.80
oedq02010	59137.786	2274-3072	40	1277	25.70
oedq02040	59137.848	2274-3072	30	354	25.76
oedq02070	59137.902	2274-3072	30	1150	25.82
oedq52010	59176.976	2274-3072	40	1277	25.69
oedq52040	59177.038	2274-3072	30	354	25.76
oedq52070	59177.092	2274-3072	40	1150	25.83
oedq04010	59326.841	2274-3072	40	1277	25.83

Table 4.11: HST STIS data that were used. I will be referring to these data as HST STIS, to distinguish between these and the ones available via ASTRAL project. To receive full declination δ of Betelgeuse, it is necessary to add $0.7^\circ 24'$ to the values listed in the table. The δ values are included, as the positions and directions of spectral scans were not the same each time. Available at [E12](#).

Table Browser for 2: odxg01010_x1d.fits

	SPORD	NELEM	WAVELENGTH	FLUX	ERROR
1	67	1024	(3021.8545385445454, 3021.904142468909, 3021.9...	(-7.3703827E-14, -1.18054234E-14, -2.122607E-14, ...	(1.6934916E-14, 1.102608E-14, 1.1243198E-14, 1.3...
2	68	1024	(2977.3779842797235, 2977.4268840646705, 2977...	(1.9164963E-13, 2.4570043E-13, 2.825898E-13, 3.2...	(3.6758126E-14, 2.8098661E-14, 3.0305355E-14, 3...
3	69	1024	(2934.190961388847, 2934.23917556552, 2934.287...	(1.6353517E-13, 2.494957E-13, 4.2477293E-13, 5.0...	(3.1824722E-14, 2.6532131E-14, 3.3784353E-14, 3...
4	70	1024	(2892.238192302374, 2892.2857386829173, 2892.3...	(1.3787593E-13, 1.4613038E-13, 1.5192254E-13, 2...	(2.812076E-14, 2.0079245E-14, 2.0800434E-14, 2...
5	71	1024	(2851.4675142750243, 2851.5144099892896, 2851...	(1.8121418E-14, 4.8388546E-14, 5.762366E-14, 9.6...	(1.8682418E-14, 1.3242038E-14, 1.4427534E-14, 1...
6	72	1024	(2811.8296630415844, 2811.875924571531, 2811.9...	(1.1209473E-13, 1.5352585E-13, 1.5783151E-13, 1...	(2.5556839E-14, 1.9725056E-14, 2.0256571E-14, 2...
7	73	1024	(2773.278074257164, 2773.323717469108, 2773.36...	(9.2671415E-14, 1.1351139E-13, 1.9150576E-13, 3...	(2.5444033E-14, 1.7760367E-14, 2.1770126E-14, 2...
8	74	1024	(2735.7687010393274, 2735.8137412142178, 2735...	(9.004865E-14, 1.3565543E-13, 1.3095482E-13, 1.7...	(2.4480118E-14, 1.893946E-14, 1.8757966E-14, 2.1...
9	75	1024	(2699.259846109083, 2699.3042979709357, 2699.3...	(2.3738756E-13, 1.8991102E-13, 2.5361744E-13, 2...	(3.3231762E-14, 2.1975567E-14, 2.4827591E-14, 2...
10	76	1024	(2663.712007185894, 2663.75588492852, 2663.799...	(1.6296296E-13, 1.2210049E-13, 1.6098719E-13, 2...	(2.9260984E-14, 1.838471E-14, 2.0631146E-14, 2.3...
11	77	1024	(2629.0877344316964, 2629.131051743798, 2629.1...	(2.5348726E-14, 3.8624865E-14, 9.021266E-15, 1.5...	(2.0487447E-14, 1.2797574E-14, 1.0360607E-14, 1...
12	78	1024	(2595.3514988621246, 2595.394268951152, 2595.4...	(5.513993E-14, 8.2868953E-14, 1.3336854E-13, 1.2...	(2.3559508E-14, 1.636139E-14, 1.9524028E-14, 1.9...
13	79	1024	(2562.469570753965, 2562.5118063881625, 2562.5...	(3.0388744E-14, 7.4650206E-14, 1.022361E-13, 9...	(2.2566733E-14, 1.633165E-14, 1.8492413E-14, 1.8...
14	80	1024	(2530.4099071726155, 2530.451620622176, 2530.4...	(5.0518082E-14, 7.762725E-14, 6.7135696E-14, 1.0...	(2.4716501E-14, 1.7084533E-14, 1.701986E-14, 2.0...
15	81	1024	(2499.142047832585, 2499.183251009458, 2499.22...	(3.6606125E-14, 8.12053E-14, 1.0542316E-13, 7.81...	(2.4765576E-14, 1.807314E-14, 2.0288465E-14, 1.8...
16	82	1024	(2468.6370185787714, 2468.677722975526, 2468.7...	(7.093455E-14, 5.7075757E-14, 8.562553E-14, 1.19...	(2.934256E-14, 1.7005584E-14, 1.9826095E-14, 2.2...
17	83	1024	(2438.867241846569, 2438.907458573816, 2438.94...	(8.642654E-15, 1.1387062E-14, 2.861009E-14, 3.21...	(2.6033271E-14, 1.3230701E-14, 1.590918E-14, 1.7...
18	84	1024	(2409.8064535178105, 2409.8461933210906, 2409...	(-4.157944E-14, 8.585876E-15, 4.2019793E-15, 1.77...	(2.4772E-14, 1.4055894E-14, 1.4442998E-14, 1.662...
19	85	1024	(2381.4296256470757, 2381.4688989227197, 2381...	(-3.3416195E-14, 4.2381006E-14, 3.951382E-14, -4...	(2.6338654E-14, 1.8856729E-14, 1.9575731E-14, 1...
20	86	1024	(2353.7128945800378, 2353.7517113899958, 2353...	(-1.02152946E-13, -1.6670623E-14, 2.5763662E-14, ...	(1.7181769E-14, 1.17164545E-14, 1.881209E-14, 1...
21	87	1024	(2326.6334940295346, 2326.6718641155776, 2326...	(-6.803683E-14, -1.31834215E-14, -2.3256414E-14, ...	(2.3516277E-14, 1.2844491E-14, 1.3398449E-14, 1...
22	88	1024	(2300.1696927152743, 2300.207625512629, 2300.2...	(-5.5967065E-14, -1.8653537E-14, -1.418241E-15, 1...	(2.2733848E-14, 1.0649655E-14, 1.5417684E-14, 1...
23	89	1024	(2274.3007362088592, 2274.3382408586485, 2274...	(-1.1917191E-13, -8.09165E-15, -3.495924E-14, 2.64...	(1.919586E-14, 1.5190569E-14, 1.3360096E-14, 1.9...

Figure 4.2: An example of STIS data default format. Compared to other available spectra, these spectra have non-linear dependence of wavelength on flux, therefore the spectra had to be transformed into a linear format, so that I could analyze them in SPLAT-VO. The spectra consist of spectral orders from 67 to 89. Viewed in topcat (E13) .

4.1.4 Radial Velocity

I was able to analyse numerous high-quality spectra from all publicly available sources, but considering that they are spread across almost 30 years time scale, they do not provide a full time coverage of the variability, at least not until phased.

The combined spectra results are pooled in table 4.12 and are plotted together in figure 4.3. The values of radial velocities v_r for HST STIS datasets **odxg**, **oe1i** and **oedq**, i.e., the ones near the Great Dimming, are averaged, as in most of the datasets I analysed more than 2 sub exposures, the ones from the centre and edges. The full non averaged radial velocities for each of the subexposures are listed in table 4.13, as they are more relevant in the next section. On the other hand, I did not average the sub exposures from the ASTRAL **o4de** dataset, i.e., the ones between MJD 50821-51265, as the positions of the scans that I used were not symmetrical towards the centre of Betelgeuse.

The results in figure 4.3 have some considerable gaps, but fortunately they seem to cover the full range of possible radial velocities v_r values, i.e., the minima and maxima. At several places, the results also display a variability at smaller time scales, such as the ones from ELODIE, and especially the ones from STIS.

The radial curve shows a major systematic difference between the velocities determined from the optical and ultraviolet spectra. While the optical radial velocities v_r have a range between about 19–28 km s^{-1} , the ultraviolet spectra have a range of only 15–22 km s^{-1} . The variability itself seems to be happening on a different time scale as well. For example a closer examination of the well covered ultraviolet peak of ASTRAL **o4de** dataset shows a relatively slow variability near the local radial velocity maximum, covering ~ 370 days, while the profile of the peak suggests that the period is much longer. On the other hand, on a similar timescale radial velocities from ELODIE seems to undergo one full period of variability. Similarly, examining the **odxg**, **oe1i** and **oedq** ultraviolet radial velocities near

Ultraviolet spectra			Optical spectra		
Source	MJD [d]	v_r [km s ⁻¹]	Source	MJD [d]	v_r [km s ⁻¹]
HST GHRS	48889.12	15.98 ± 0.72	F/H	49868.96	19.90 ± 0.85
HST ASTRAL	50821.44	20.90 ± 0.39	F/H	50455.68	27.97 ± 0.50
HST ASTRAL	50821.45	21.20 ± 0.40	ELODIE	51204.90	22.67 ± 0.48
HST ASTRAL	50821.45	20.27 ± 0.43	UVES	52530.42	22.02 ± 0.58
HST ASTRAL	50904.66	21.61 ± 0.63	ELODIE	52873.14	22.75 ± 0.48
HST ASTRAL	50904.67	21.35 ± 0.39	ELODIE	52899.16	22.64 ± 0.46
HST ASTRAL	50904.67	21.61 ± 0.74	ELODIE	52953.09	20.45 ± 0.50
HST ASTRAL	51077.18	21.57 ± 0.40	ELODIE	53048.90	19.98 ± 0.57
HST ASTRAL	51077.18	20.36 ± 0.45	ELODIE	53121.81	20.68 ± 0.44
HST ASTRAL	51077.19	19.45 ± 0.45	ELODIE	53244.16	22.96 ± 0.44
HST ASTRAL	51265.30	20.01 ± 0.50	ELODIE	53404.90	19.29 ± 0.47
HST ASTRAL	51265.31	20.73 ± 0.50	SOPHIE	54074.01	22.65 ± 0.53
HST ASTRAL	51265.31	20.57 ± 0.46	XSHOOTER	55116.34	26.62 ± 0.72
HST ASTRAL	52562.57	19.90 ± 0.49	UVES	56570.38	20.61 ± 0.50
HST ASTRAL	52701.57	20.42 ± 0.41	HARPS	58891.07	19.82 ± 0.49
HST ASTRAL	52752.54	20.28 ± 0.44			
HST ASTRAL	55600.34	21.05 ± 0.47			
HST ASTRAL	55600.39	20.03 ± 0.50			
HST ASTRAL	55606.12	20.21 ± 0.47			
HST ASTRAL	55615.85	20.44 ± 0.49			
HST ASTRAL	55617.91	19.21 ± 0.53			
HST ASTRAL	55617.96	18.08 ± 0.45			
HST ASTRAL	55652.38	17.89 ± 0.45			
HST STIS	58508.31	17.30 ± 0.64			
HST STIS	58547.57	17.30 ± 0.64			
HST STIS	58573.06	17.46 ± 0.46			
HST STIS	58591.34	17.57 ± 0.59			
HST STIS	58714.76	17.30 ± 0.64			
HST STIS	58744.33	16.78 ± 0.58			
HST STIS	58762.81	17.69 ± 0.64			
HST STIS	58815.64	17.29 ± 0.65			
HST STIS	58866.56	16.36 ± 0.59			
HST STIS	58882.38	17.91 ± 0.62			
HST STIS	58904.82	17.81 ± 0.58			
HST STIS	58941.04	17.94 ± 0.63			
HST STIS	59092.77	17.45 ± 0.70			
HST STIS	59137.85	17.88 ± 0.61			
HST STIS	59177.04	18.15 ± 0.61			
HST STIS	59326.89	17.73 ± 0.83			

Table 4.12: Determined radial velocity v_r from all the spectra. For some optical spectra, a heliocentric correction was performed using E14, as not all the spectra had been already corrected by their providers. Some STIS spectra were averaged, see table 4.13 for the non averaged values.

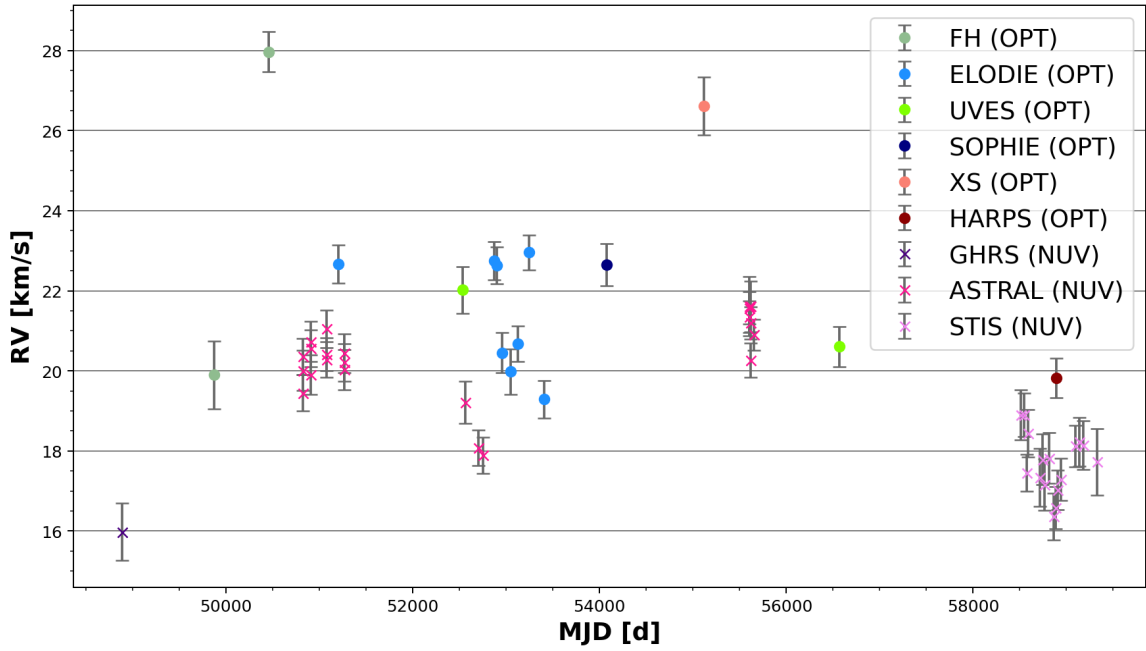


Figure 4.3: Dependence of radial velocity v_r on MJD, using results from all the spectra that were analysed in this thesis. How the data compare to the light curve is discussed in figure section 4.4. A larger version of the figure is provided later in this thesis in figure 4.14, as part of the radial-light curve.

The Great Dimming, covering ~ 820 days yields a slow fall into a minimum, culminating by the time of the Great Dimming, and a subsequent slow rise. Therefore, the data suggest that radial velocity in ultraviolet is undergoing a variability on a much longer time scale than radial velocity in the the optical part of the spectrum, while the amplitude is smaller. I will examine the period and variability of radial velocities v_r further in section 4.3, once I can also compare it with photometric data. Ultraviolet and optical radial velocities will be examined separately.

An important distinction to make is addressing what the term radial velocity v_r in regards to Betelgeuse signifies. While radial velocities v_r from the spectra demonstrate that there is a significant variability, therefore that the visible layers of Betelgeuse are periodically moving towards and away from us, relative to an average radial velocity \bar{v}_r , the centre of the mass of Betelgeuse is moving at a relatively constant radial velocity (the value given in section 2.2.2 by Famaey et al. (2005)), and the changes we observe are largely due to the pulsations of Betelgeuse. Henceforth, the variability is due to some layers of Betelgeuse's atmosphere changing it's relative velocity towards us. As the majority of contributions to the spectra are from the photosphere, it would be more relevant to use term photospheric velocity v_{photo} to describe the velocity variability, to properly distinguish between these two motions.

4.1.5 Rotational Velocity

As I emphasized in [section 4.1.3](#), the spectra from STIS are taken at different positions of Betelgeuse, including the centre and edges. Furthermore, as can be seen in [figure 4.4](#), the path of spectral scans is almost perpendicular to the rotational axis by [Kervella et al. \(2018\)](#). Thus, if the rotational effects are observable, it is possible to determine this, by comparing the spectra from edges to the central spectra and to each other, as one side of Betelgeuse should be moving towards us, while the other side away from us.

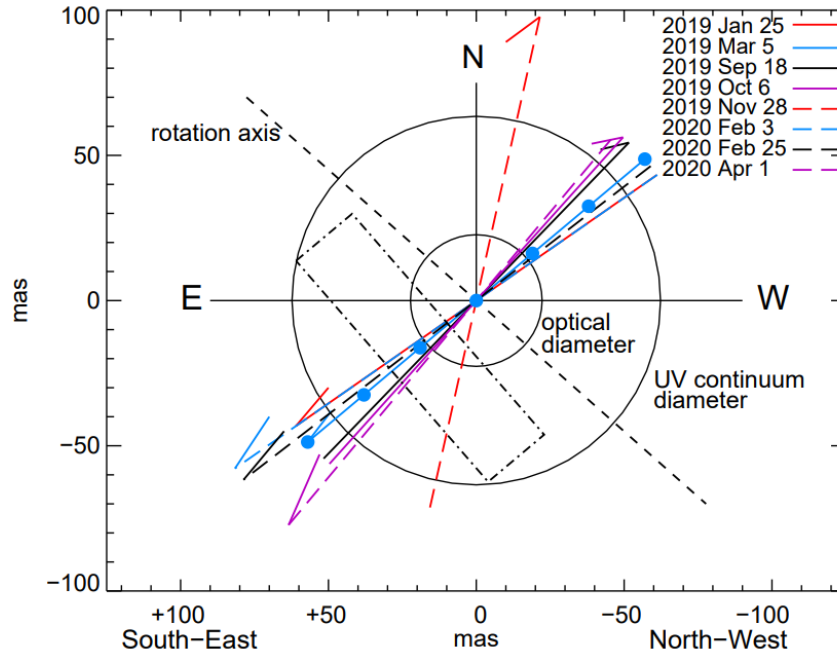


Figure 4.4: Locations of spectral scans across the surface of Betelgeuse. The broken coloured lines are for different datasets, while the arrows indicate their direction. The blue circles show the specific locations of spectral scans, while the rectangle shows the size of the aperture. The rotational axis is based on the value determined by [Kervella et al. \(2018\)](#). The figure was adapted from [Dupree et al. \(2020\)](#).

Table [4.13](#) lists results of radial velocities v_r , they are plotted in [figure 4.5](#). These data were also used in the previous chapter for determining the changes in radial velocity, but most datasets were averaged, in cases when there were more than 1 sub exposure available.

Even though in some datasets the values of central radial velocities are indeed between radial velocities from edges, the resulting plot ([figure 4.5](#)) does not show a systematic trend that would reveal the projected rotational velocity $v_{\text{rot}} \sin(i)$. This is due to the fact that the values of photospheric of the edges are in general at various values relative to central radial velocities. And more importantly, the values of radial velocities from both edges are not systematically higher or lower towards each other. There appears to be a certain systematic trend for the data by the middle of the [figure 4.5](#), i.e., by the time of the Great Dimming, as the difference between radial velocities from the edges has relatively uniform values. According to [Kervella et al. \(2018\)](#) in [section 2.2.2](#), the value of projected rotational velocity should be $v_{\text{rot}} \sin(i) = 5.47 \pm 0.25 \text{ km s}^{-1}$, therefore the effects should

Dataset	MJD [d]	v_r [km s ⁻¹]		
		010	040	070
odxg01	58508.25	18.36 ± 0.67	19.21 ± 0.61	19.15 ± 0.59
odxg02	58547.51	19.69 ± 0.57	18.83 ± 0.47	18.17 ± 0.58
odxg06	58573.06	17.46 ± 0.46		
odxg03	58591.27	18.56 ± 0.64	19.13 ± 0.59	17.63 ± 0.55
odxg04	58714.68	17.15 ± 0.76		17.53 ± 0.67
odxg07	58744.26	18.11 ± 0.57	17.45 ± 0.64	17.81 ± 0.70
odxg08	58762.75	16.73 ± 0.50	17.27 ± 0.68	17.47 ± 0.72
oe1i01	58815.58	17.13 ± 0.56	18.47 ± 0.63	17.86 ± 0.70
oe1i02	58866.56	16.36 ± 0.59		
oe1i52	58882.32	16.75 ± 0.54	15.73 ± 0.46	17.26 ± 0.60
oe1i03	58904.76	16.95 ± 0.42	16.66 ± 0.44	17.48 ± 0.59
oe1i04	58940.97	17.75 ± 0.56	16.98 ± 0.50	17.15 ± 0.53
oedq01	59092.70	18.18 ± 0.48	18.10 ± 0.50	18.10 ± 0.58
oedq02	59137.76	17.45 ± 0.64	18.22 ± 0.64	19.03 ± 0.55
oedq52	59176.98	17.42 ± 0.64	18.65 ± 0.57	18.38 ± 0.61
oedq04	59326.84	17.73 ± 0.83		

Table 4.13: Determined radial velocities from edges and a centre of the Betelgeuse. MJD correspond to the first sub exposure within a dataset.

have been theoretically observable. But based on the data, it is questionable whether rotational effects are observable in UV. That notion is reinforced by figure 4.4, as we can see that ultraviolet diameter of Betelgeuse is much larger than the optical diameter.

However, it should also be noted that while one may be able to measure rotational effects at the edges, no longer are the radial velocities of the pulsations, i.e. the photospheric velocity v_{photo} , measured to the full extent. Therefore assuming that the average \bar{v}_r value of the centre of the mass of Betelgeuse is higher than during the Great Dimming, as the ultraviolet radial velocities appear to be at minimum during the Dimming, the radial velocities from the edges should hypothetically be somewhat higher than the central radial velocities, at least during The Great Dimming.

But of course, as the diameter R of Betelgeuse changes significantly during the pulsations, compared with the positions of STIS scans, which remain relatively the same to the centre of Betelgeuse, it is possible that the 010 and 070 sub exposures might not have been scanned at the relative edge of Betelgeuse in some datasets.

I also analysed 3 sub exposures in each of the HST STIS ATRAL **o4de** dataset. There the positions that I used however were not symmetric with respect to the center of Betelgeuse, but instead they were 040, 050 and 060. Therefore, going from the centre to one of the edges, but not the full way. Similarly, there should hypothetically be a systematic shift in radial velocity (as the STIS could have been scanning in either direction, the values of radial velocity could be either increasing or decreasing). The change would likely be small, but considering the higher quality of ASTRAL spectra, it could be possible to observe the effects. Nonetheless, the results of **o4de** dataset in table 4.12 (the values with MJD between 50821-51266) do not show any systematic shift either, even though the

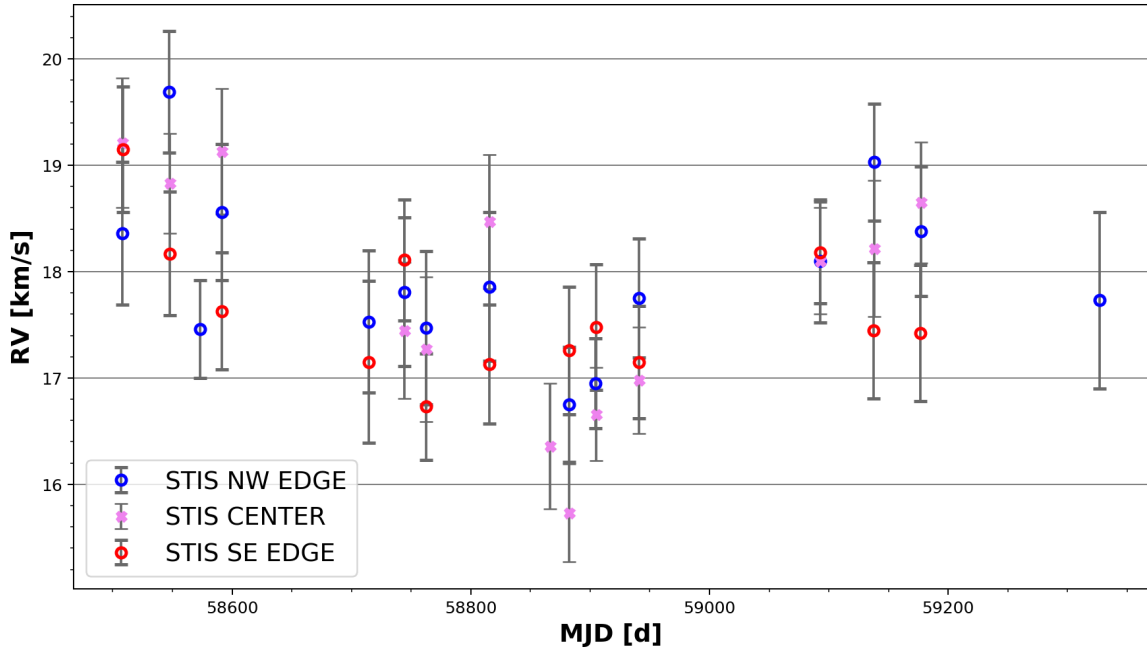


Figure 4.5: Comparison between radial velocities determined from central spectra (040) and edge spectra (010 and 070) from the datasets **odxg**, **oeli** and **oedq**. The directions of scans were not the same each time, EDGE labels assigned based on δ in table 4.11.

values appear to be somewhat systematic in figure 4.3.

4.2 Photometry

There are many publicly available sources of photometric data as well, in general divided across less sources, but each includes a lot of data. Some data is derived from space missions, while other parts are gathered from ground observatories, or even amateur astronomers. For cleaning the data by removing outliers, I used peranso program (Paunzen & Vanmunster, 2016). Peranso is one of the leading programs for working with photometric data and determining periods in variable systems. It can be downloaded from E15. To be able to use the program fully, it is necessary to buy a license to the program, although it is also possible to use a trial version. To remove outliers, it is possible to use Lowess fit with 3 following parameters. I set a value of "Smoothing amount" parameter to about 20, while I set values of "Envelope width" and "Curve size" to about 3. These parameters were used to remove outliers in most of the following photometric data.

Apart from the sources listed below, I had also accessed Transiting Exoplanet Survey Satellite (TESS) photometric data, but in the end I did not use the data, as the data covered only a very small timescale (a few days), while it would have been necessary to calibrate the data.

4.2.1 BRITE

Bright Target Explorer (BRITE) is a network of nanosatellites that study the brightest stars in the sky. The network aims to study all stars with visual magnitude m higher than 3.5 mag. Due to its low orbit and wide field of view, it is able to provide valuable long term continuous observations. Therefore the mission provides many useful data for photometry and asteroseismology of these stars. It consists of 5 nanosatellites, three working in red filter, and two in blue filter (not fully corresponding to B and R filters). All the data and information are available at [E16](#).

By default, the data is provided in the following format. The date is in Heliocentric Julian Date (HJD), which I converted to MJD. Flux is provided as the signal extracted from image per second, hence it's in $\frac{\text{ADU}}{\text{s}}$. Some other data were available as well, but I did not need those. Based on BRITE's Cookbook by [Pigulski \(2018\)](#), the flux was converted into apparent magnitude m using Pogson's equation

$$m = -2.5 \log_{10}(f) + 14.5, \quad (4.2)$$

where f is the flux of a star. It is necessary to add an arbitrary constant of 14.5 mag to the results.

BRITE is focused at several stellar fields, including Orion. So far, Orion field has been observed and published 7 times, 6 of those observations have already been made public and 5 of them include Betelgeuse. BRITE stays at single field for several months, for Betelgeuse it's usually since autumn till March.

Red Filter

The observations in red filter are provided by 3 nanosatellites, UniBRITE (UBr), BRITE Toronto (BTr) and BRITE Heweliusz (BHR). They were pointed at Betelgeuse during mission fields Ori I (2013-2014), Ori II (2014-2015) and Ori III (2015-2016).

Blue Filter

The observations in blue filter are provided by 2 nanosatellites, BRITE Austria (Bab) and BRITE Lem (BLb). The blue satellites were pointed at Betelgeuse each time, hence including the missions mentioned above, as well as Ori IV (2016-2017) and Ori VI (2019-2020).

All filters

The results are plotted together in figure 4.6. The data contained large numbers of outliers, which is typical for BRITE data, therefore it was necessary to remove them. The outliers are usually due to a stellar image being located close to the edge of a subraster or the image being smeared by the satellite's movement, when an observation takes a significant portion of BRITE's ~ 100 minutes orbit, or even more than one orbit. However due the huge amount of data, the light curve is still clearly visible. Unfortunately, the data have significant gaps and do not cover that a large timescale.

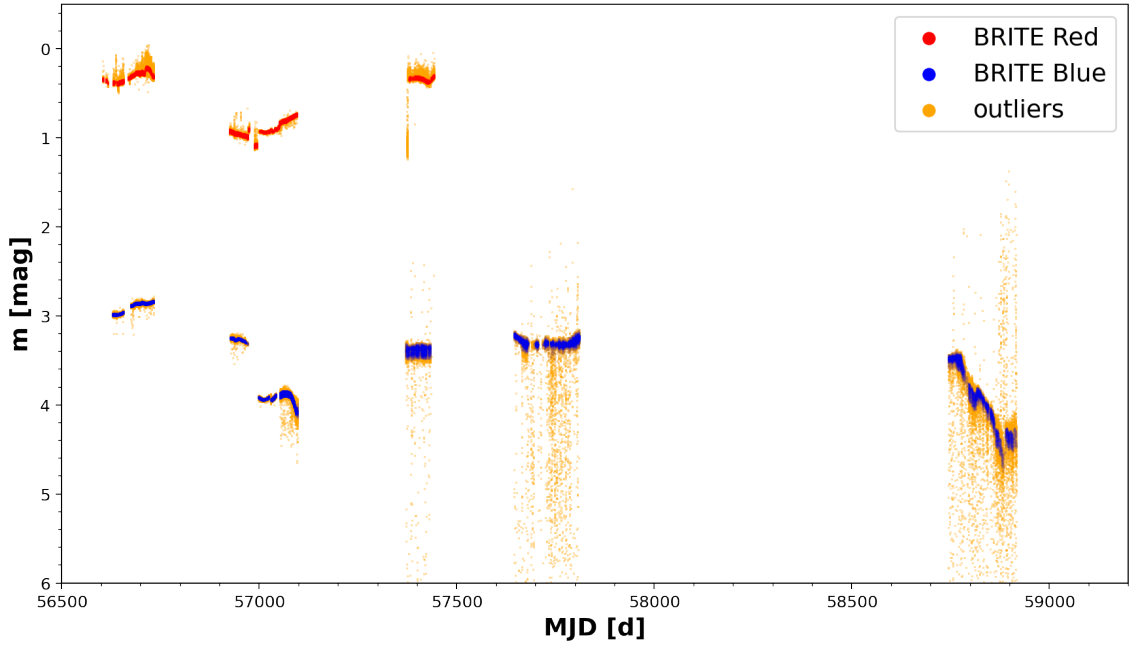


Figure 4.6: Light curve of Betelgeuse in both of BRITE filters. The colours correspond to the filters. The curve includes The Great Dimming. The data contain about 200 000 data points. About 15 % of the data were removed as outliers by peranso.

4.2.2 SMEI

Solar Mass Ejection Imager (SMEI) is an instrument aboard Coriolis satellite. Aboard the satellite there are other instruments as well, studying earth atmosphere using a polarimetric radiometer. SMEI observes many stars, while it also studies solar winds, aiming to be able to predict them. Apart from periodical changes in brightness, it can also detect asteroseismological oscillations (Jackson, 2004). All the information are available at web page of the program E17.

The bandpass in which SMEI observes is 4500-11000 Å, therefore it is similar to one of the filters in Gaia spectroscopic system (E18). The data is not publicly available, but due to courtesy of doc. Ernst Paunzen, Dr.rer.nat., I was allowed access. The SMEI data are in Gregorian calendar format, therefore it was necessary to convert them to MJD. The brightness of Betelgeuse was already provided in apparent magnitude m .

The original data had some false trends and measurement errors. Ernst Paunzen cleaned the data and removed the effects of stray light and other errors, while I also removed some of the remaining outliers. The final data are plotted in figure 4.7.

We are able to see Betelgeuse's variability in a great detail. It covers numerous continuous periods of the shorter cycle, and almost two periods of the longer cycle. Therefore, these data can be used to determine periodicity and study it's details, as well as compare it to the radial velocities v_r .

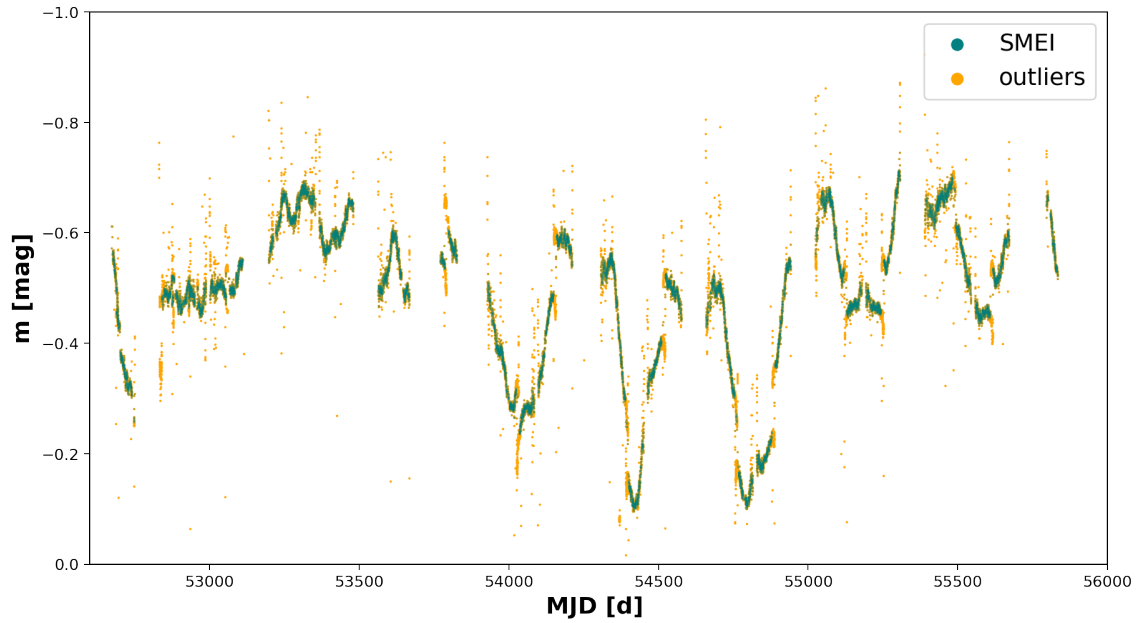


Figure 4.7: Light curve of Betelgeuse, using SMEI data. It covers data from about 2002 to 2012. The outliers were removed by peranso. The access to the data is due to courtesy of Ernst Paunzen.

4.2.3 AAVSO

The American Association of Variable Star Observers (AAVSO) is an organization that collects observations of variable stars from both, amateur and professional astronomers. In result, the data come from various sources and instruments. Nevertheless, all the data come through a validation process that ensures the quality of the data. Thus, the AAVSO archive is a major science resource. The data can be accessed at [E19](#). The archive is focused at photometric observations, although there are also some spectroscopic ones.

For Betelgeuse, there exists a wealth of data, over 37 000 observations. However, a large majority of them are in Visual filter, i.e., by a naked eye, that covers about a hundred of years. Those data were not used. Instead, observations corresponding to the photometric filters, i.e., the ones that were observed using photometric instruments, were used. A majority of those data are in *V* filter. The *V* filter observations relatively continuously cover the last 30 years, which I can use well to supplement SMEI observations. The other filters are mostly continuous only during The Great Dimming, as the unprecedented event apparently attracted many observers. Those data can be used to compare the scope of the dimming in various filters. As the AAVSO data are already provided calibrated, I plot the data together in a joint light curve (figure 4.8), alongside the calibrated data from figures 4.7 and 4.6.

4.2.4 Light Curve

Combining the data gives us almost a continuous brightness variability of Betelgeuse in the 2000-s, with SMEI covering the first decade, and AAVSO supplementing sufficiently

enough the rest. The combined plot can be seen in figure 4.8.

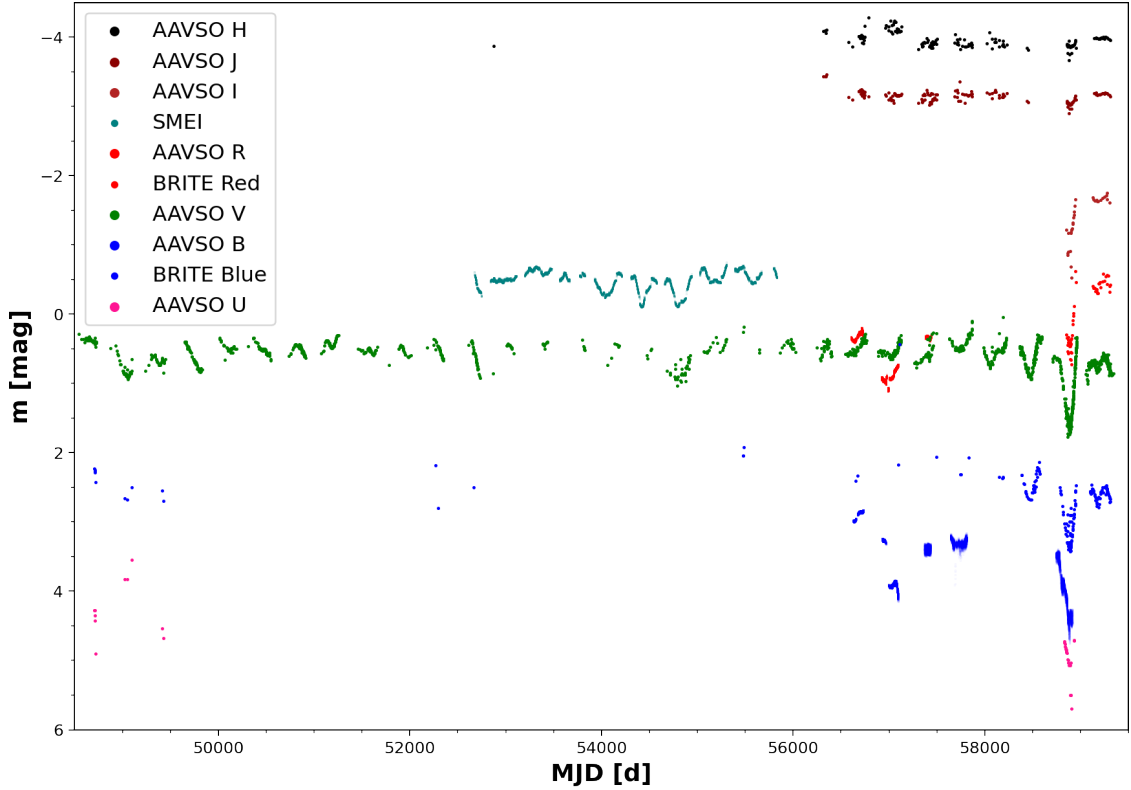


Figure 4.8: Light curve comprising of all the photometric data used in this thesis, covering the last three decades, and ending shortly after The Great Dimming. The data from V filter range even farther into history, but for scaling purposes they are not plotted.

As can be seen in the the figure, the observations in filters using longer wavelengths (I, J, H) are considerably less affected by the variability of the star. As the star is the brightest in near-infrared region, it means that the variability that we observe (most often in optical region) does not affect the overall brightness of the star in such a dramatic way. That can be seen in even greater extent during the Great Dimming as well, which suggests several possible causes of the Dimming. This is further examined in the subsection 4.5.1. For the determination of period, SMEI is the best source, as it has a continuous high-quality coverage of almost two periods. The V filter from AAVSO is also very promising, but it has large time gaps. The time gaps are caused by the position of the star, as in summer it is difficult to observe Betelgeuse by ground based observations (therefore most of the optical spectra have been resolved in winter as well). The period determination is going to be covered in the following section 4.3.

4.3 Period Analysis

For determination the periods, I used primarily the peranso program, and supplemented some functions by period04 (Lenz & Breger, 2005) as well. Period04 has a similar purpose

to peranso and is freely available at full version, but has less functionality. Period04 can be downloaded at [E20](#).

I will explore Betelgeuse’s semi-periodicity from several different angles in the upcoming sections, i.e., based on photometric data and based on radial velocities v_r of optical and ultraviolet spectra. The generally accepted periods given by [Kiss et al. \(2006\)](#) and [Chatys et al. \(2019\)](#) in [subsection 2.2.3](#) will be referred to as the shorter period ($P_{\text{short}} \sim 388$ days) and as the longer period ($P_{\text{long}} \sim 2050$ days).

4.3.1 Photometric Variability

Photometric period analysis was performed using the SMEI data in peranso, after outliers were removed. The result is shown in figure 4.9.

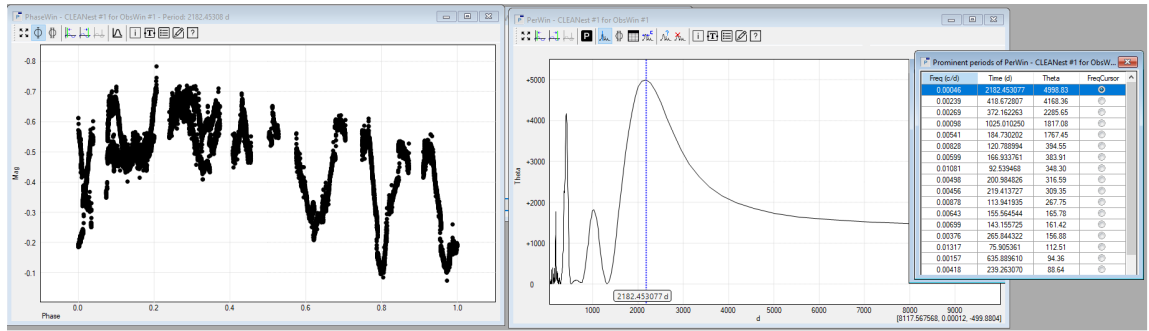


Figure 4.9: Period analysis of Betelgeuse’s apparent brightness based on SMEI, determined by peranso’s Fourier transformation using CLEANest model. The dominant longer ~ 2150 days and the shorter ~ 400 days periods are clearly visible. However, the span of the data is only ~ 3000 days, therefore the determination of the longer period is not reliable. On the left side, the SMEI data are phased by the longer period, after the removal of outliers.

The dominant periods are $P_1 = 2182 \pm 284$ d and $P_2 = 419 \pm 14$ d (the uncertainties, as well as all the following ones, are given by peranso). The third strongest period $P_3 = 372 \pm 72$ d shares the peak with P_2 . These results correspond well to the values given in [subsection 2.2.3](#) by [Kiss et al. \(2006\)](#) and [Chatys et al. \(2019\)](#). However, as SMEI covers ~ 3000 days, it is questionable whether peranso’s determination of P_1 is reliable. Nonetheless, the longer period is often given with a similarly large uncertainty, such as in the literature cited above.

4.3.2 Radial Velocity Variability

As I discussed in [subsection 4.1.4](#), radial velocity from different parts of Betelgeuse’s spectrum, i.e., ultraviolet and optical, should be examined separately.

Optical Radial Velocities Variability

I analysed all radial velocity results from the optical part of the spectrum (table 4.12), therefore all the data from the ground spectrographs. The periods of variability determined based on the data were promising. However, as they had large time gaps, I also adapted

high-quality determinations of radial velocities from figures 2.5 by HERMES spectrograph (Kravchenko et al., 2021) and 2.7 by STELLA spectrograph (Dupree et al., 2020) to improve the results. From the available masks that Kravchenko et al. (2021) used to resolve HERMES spectra, I chose to adapt mask C4 into this thesis, as the radial curve of the mask was the most similar to the radial curve by STELLA. Peranso was used to determine the periods, and period04 was used to determine the amplitudes.

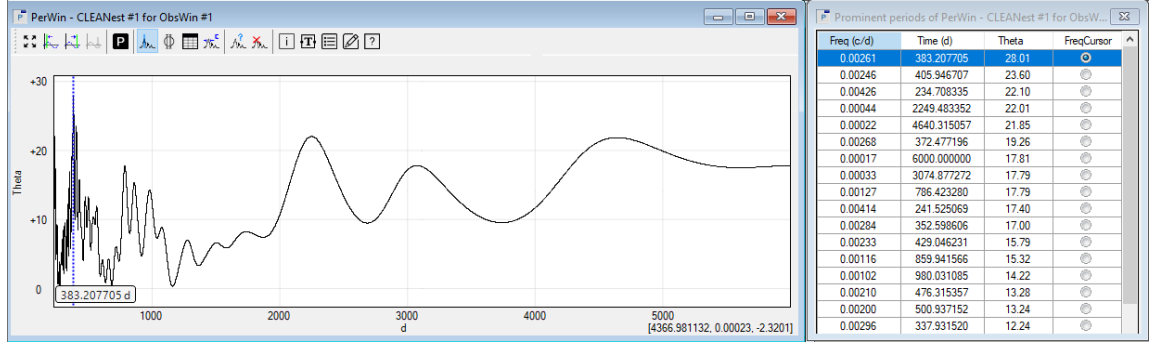


Figure 4.10: Period analysis of optical radial velocity v_r , i.e., photospheric velocity v_{photo} , determined by peranso's Fourier transformation using CLEANest model. The minimal period was set to 200 days.

The dominant periods are $P_{1,v_r} = 383 \pm 7$ d, $P_{2,v_r} = 406 \pm 7$ d, $P_{3,v_r} = 235 \pm 5$ d and $P_{4,v_r} = 2249 \pm 240$ d. The first two result corresponds well to the shorter period given in subsection 2.2.3 by Kiss et al. (2006) and Chatys et al. (2019), as well as to my shorter photometric period (P_2 and P_3). Furthermore, when the optical v_r are phased by the period P_{1,v_r} , it corresponds relatively well to the period, as can be seen in figure 4.11.

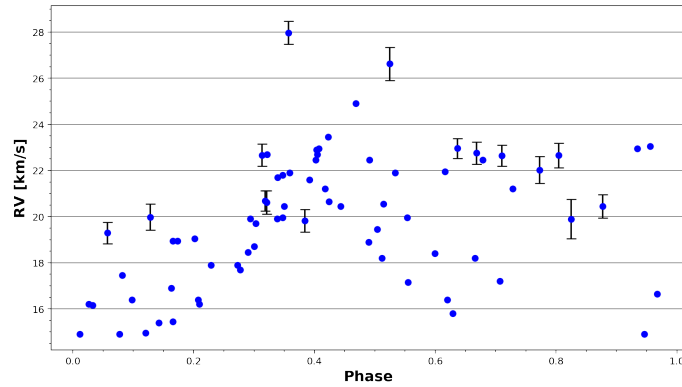


Figure 4.11: Optical radial velocity v_r phased by period P_{1,v_r} . The values with error bars are the optical radial velocities determined in this thesis, the ones without error bars are the ones adapted from the figures 2.5 by Kravchenko et al. (2021) and 2.7 by Dupree et al. (2020).

The fourth period P_{4,v_r} likely suggests a connection to the longer period. But in general, the variability of optical radial velocity does not fully correspond to the longer period, as it is only the fourth strongest period. Therefore, considering that the variability

of radial velocity, i.e., the photospheric velocity v_{photo} , is attributed to the pulsations of the atmosphere (discussed in subsection 4.1.4), these results support that the shorter period is caused primarily by the Betelgeuse's pulsations, while the longer period is due to other processes that may partially affect radial velocities as well.

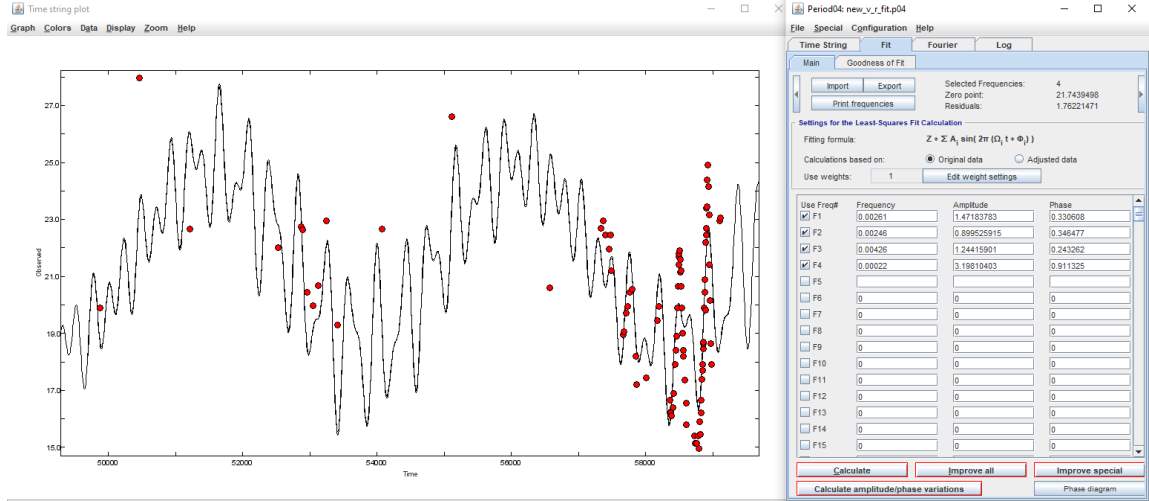


Figure 4.12: Optical radial velocity v_r fitted in period04 with the 4 strongest periods from the peranso's Fourier transformation.

Based on period04, radial amplitudes $v_{r,\text{max}}$ of the 4 most dominant periods are $v_{P_1,\text{max}} = 1.47 \text{ km s}^{-1}$, $v_{P_2,\text{max}} = 0.90 \text{ km s}^{-1}$, $v_{P_3,\text{max}} = 1.24 \text{ km s}^{-1}$ and $v_{P_4,\text{max}} = 3.20 \text{ km s}^{-1}$. These values were used to create a fit of optical radial velocities in figure 4.14.

Ultraviolet Radial Velocities Variability

I performed the period analysis for all radial velocity results from the ultraviolet part of the spectrum, hence from the spectrographs aboard HST. I used the averaged values of for some of the datasets, i.e., the values in table 4.12, not the ones in table 4.13.

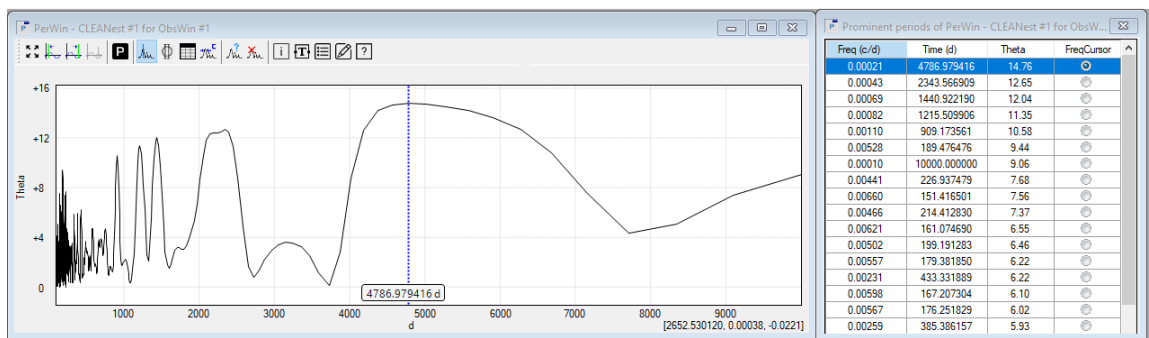


Figure 4.13: Period Analysis of ultraviolet radial velocity v_r , determined by peranso's Fourier transformation using CLEANest model. No apparent period is given.

The dominant periods are $P'_{1,v_r} = 4800 \pm 1400 \text{ d}$, $P'_{2,v_r} = 2340 \pm 380 \text{ d}$ and $P'_{3,v_r} = 1441 \pm 62 \text{ d}$. However, P'_{1,v_r} is very likely a false peak, as the given period is about a half the time

span of the data, and also has a huge uncertainty. P'_{2,v_r} suggests a connection to the longer period, although P'_{3,v_r} and two other relatively strong peaks near it suggests an entirely different period. Therefore, it appears that the variations of ultraviolet radial velocities v_r are not caused by the pulsations. Instead, they are likely a subject to other processes in other parts of the Betelgeuse's atmosphere, possibly loosely connected to the similar ones that cause the longer period (the processes were listed in chapter [subsection 2.2.3](#)).

4.4 Radial-Light Curve

I plotted together the radial velocity (table [4.12](#)) and major photometric data in figure [4.14](#), so that we can directly compare the curves. The fit that was used in the figure is just an approximations of the pulsations, based on Fourier transformation in `peranso` and `period04`. It represents correctly, that the exact amplitude changes, as well as the length of each pulsation cycle to a certain degree, as other processes likely influence the period as well. I used the results of optical radial velocity from figures [2.5](#) by [Kravchenko et al. \(2021\)](#) and [2.7](#) by [Dupree et al. \(2020\)](#) to improve the fit and also to directly compare the data, as the studies aggregated more data within shorter periods of time. The adapted data cover years 2015-2020. During that time period, my only optical radial velocity data point is the one from HARPS, however it corresponds well to the adapted values.

The variability of amplitudes of both curves seems to be correlated, i.e., when the magnitude amplitudes are smaller, the radial amplitudes are smaller as well and vice versa. That can be seen reasonably well by examining the section covered by SMEI, as well as during the Great Dimming. The fit suggests a relatively strong dependence of the radial velocity on the longer period P_{4,v_r} , but as there are not enough data in most of the curve, it is not certain that the dependence is truly that significant.

4.5 Discussion on the Great Dimming

I am able to discuss the event only based on the limited data and tools that were used in this thesis. Nevertheless, even despite the fact, I am able to make several conclusions based on my results.

The radial velocity variability does not point towards anything unusual during the Great Dimming, although the radial velocity amplitude of the peak during the Great Dimming seems to be a bit higher than usually. The values of the velocities are similar to some of the other values during the last 30 years, therefore the Great Dimming was likely not directly caused by pulsations, and it also did not affect them. Although, while in other data from the last 30 years there does not seem to be a direct correlation between the optical and ultraviolet radial velocities v_r , during the Great Dimming there is. Based on radial curve in figure [4.14](#) there was a maximum shortly after the Dimming. In the same time, based on the extensive continuous ultraviolet data from the same time that I used, there conclusively was a minimum of ultraviolet radial velocity, about a month before the apparent magnitude m minimum, i.e., the Great Dimming. Based on the other data, it is hard to say whether this correlation between ultraviolet and optical (photospheric) radial velocity is a rule, or whether it happened only during the Great Dimming.

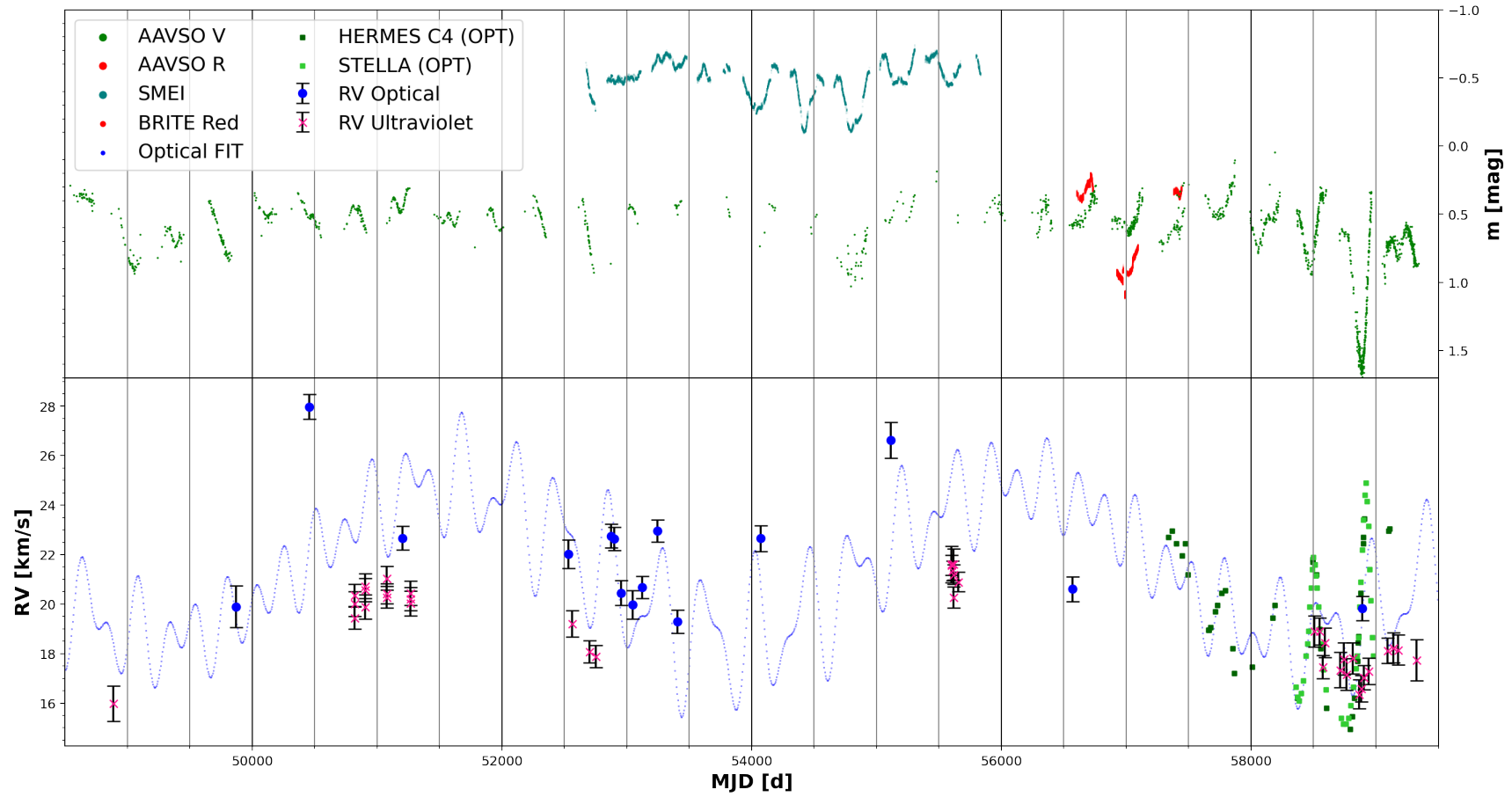


Figure 4.14: A joint plot of radial and photometric data, covering the last 30 years, including the Great Dimming. For the photometric data, only some data were used for scaling purposes. For the fit of optical radial photospheric velocities v_r , the amplitude values determined by period04 in [section 4.3.2](#) were used, i.e., also the ones from [Kravchenko et al. \(2021\)](#) and [Dupree et al. \(2020\)](#).

The photometric data do not support that the Great Dimming is due to a convergence of the shorter and longer period, as even when the two periods from the SMEI data are extrapolated, such a decrease in apparent magnitude m could likely not happen. Fortunately, the AAVSO photometric data from various filters (figure 4.8) give a major information about what could have possibly caused the Dimming. Based on the filters from near-infrared region, where Betelgeuse is the brightest, the Dimming is on a much smaller magnitude scale (filter I) than in optical filters, or barely noticeable at all (filters J and H). Therefore, it possibly means that Betelgeuse was actually not physically affected by the Great Dimming, i.e., that the star did not change its luminosity L , but that there was an extinction, mostly in optical region. That could have been due to dust particles in a proximity of the star, therefore Betelgeuse must have experienced a significant loss of mass prior to the Dimming. The reason could also be, that Betelgeuse's effective temperature T_{eff} decreased. That would cause the peak of Betelgeuse's brightness to move to higher wavelengths (based on Planck's radiation law in equation 3.1), henceforth the Dimming would be of a smaller scale in the infrared. So Betelgeuse could have decreased either its entire surface's effective temperature, or only some parts of the surface did. Betelgeuse is known to have large convective cells and starspots, so possibly the overall surface temperature could have temporarily decreased due to an unprecedented activity of this kind. I shortly explore effects of a hypothetical decrease in effective temperature T_{eff} in the following subsection 4.5.1.

4.5.1 Models of Stellar Fluxes

Using the atlas of grids of models and fluxes available at Fiorella Castelli's website (E21), I am able to compare what changes to the flux of a star of similar composition to Betelgeuse would correspondingly cause a decrease in temperature T_{eff} . The most similar set of models to Betelgeuse is *fp00k2c125odfnew*. It is a grid of fluxes for a star of a Sun's metallicity Z with a velocity of turbulences $v_{\text{turb}} = 2 \text{ km s}^{-1}$, which is the maximal available v_{turb} . According to Dolan et al. (2016), Betelgeuse has $Z = 0.024$ and according to models for Betelgeuse by Harper et al. (2020) it has $v_{\text{turb}} \sim 5 \text{ km s}^{-1}$. Furthermore, the models of fluxes are divided based on T_{eff} and $\log(g)$. Based on models by Levesque & Massey (2020), the best models for Betelgeuse have $\log(g) = 0$, therefore I picked the models with this value. Based on figure 2.5 by Kravchenko et al. (2021), Betelgeuse's T_{eff} varies between $\sim 3550 \text{ K}$ and $\sim 3650 \text{ K}$. The nearest available values of T_{eff} in the atlas were 3500 K , which was the lowest available value, and 3750 K , therefore I used those two values.

Altogether, several compromises had to be made to find the closest model to Betelgeuse, henceforth the following results are approximative. According to the formula in the atlas, model fluxes H_{λ} were converted to flux F by

$$F(\lambda) = \frac{4H_{\lambda}c}{\lambda^2}. \quad (4.3)$$

The results are shown in figure 4.15. The models shows that the greatest decrease in magnitude m would be in the optical region (filter V), up to $\sim 1 \text{ mag}$. The decreases in filters B and R would be slightly smaller, in filter I it would be about $\sim 0.5 \text{ mag}$, and

in infrared filters J and H it would be about ~ 0.2 mag. These values are very similar to the ones that we can see during the Great Dimming in the figure. To have exact values of apparent magnitude difference Δm it would be also necessary to add extinction A . Nevertheless, despite the various approximations taken, it appears plausible that based on these approximative models, the Great Dimming could have been caused by decrease of effective temperature by about $\Delta T_{\text{eff}} \sim 250$ K.

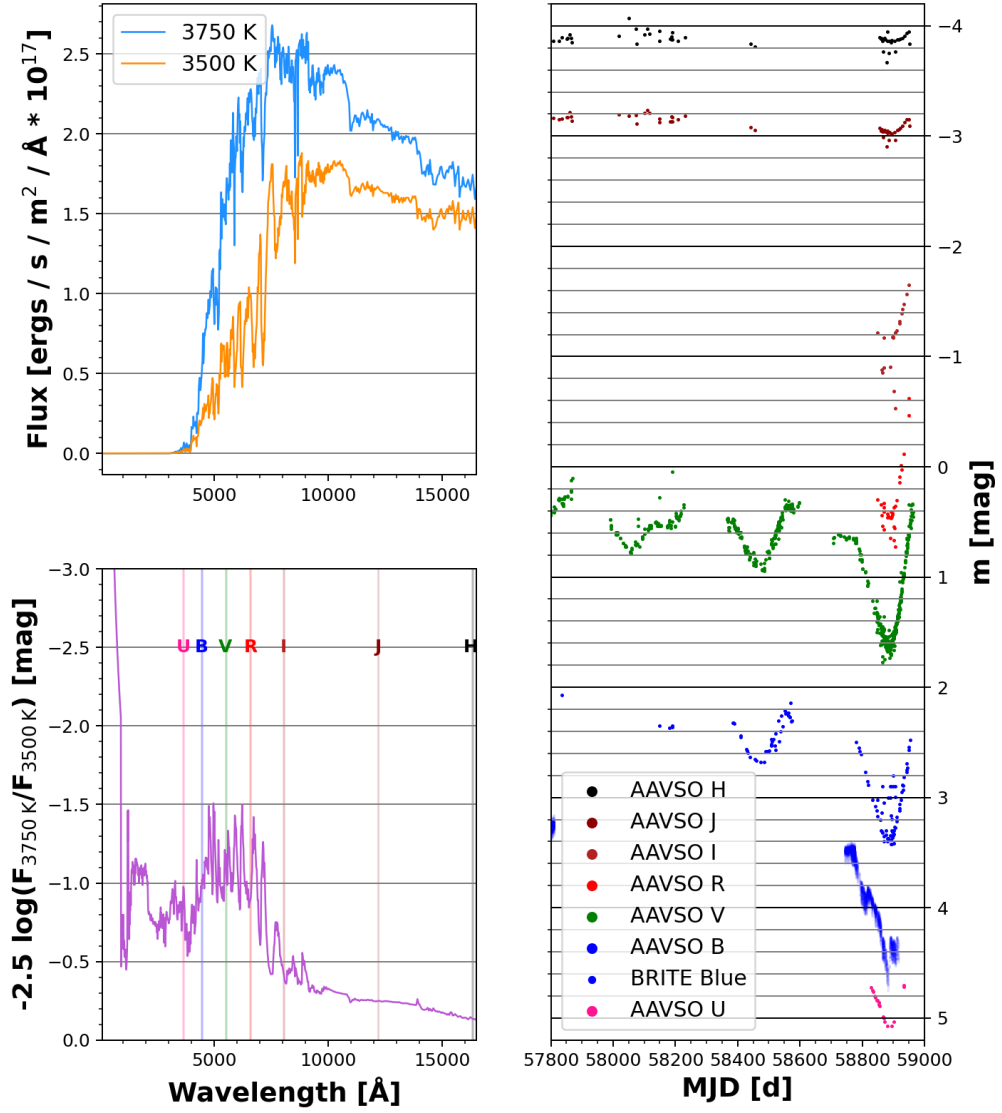


Figure 4.15: Upper left figure shows the emergent fluxes for a star with effective temperature T_{eff} equal to 3750 K and 3500 K. Bottom left figure shows a dependence of the magnitude difference Δm between the two models and also labels the midpoints of used photometric filters. The third figure shows The Great Dimming in a greater detail than figure 4.8, so that the magnitude depths of the Great Dimming can be compared to the the bottom left figure.

Conclusions and Future Insights

In this thesis I aimed to study Betelgeuse's variability in an attempt to explain what causes it, and possibly bring some context to the unprecedented Great Dimming that we witnessed in February 2020. In the theoretical part, I explained basics of overall stellar evolution to be able to discuss red supergiants and especially Betelgeuse. As part of it, I summarized results of some of the leading papers that studied the Great Dimming event. I also shortly described the stellar spectroscopy and some of its methods, before moving on to the analysis. Most my results are in a relative accordance with the results published in the cited papers.

In the practical part, I used spectroscopic and photometric methods to study Betelgeuse's variability. I accessed all the available public archival data, coming from various high-quality instruments, as well as a non public source. In total, I analysed about 80 spectra from optical and near ultraviolet region, and about 200 000 photometric data points. I analysed them in 3 astrophysical programs and created my own python scripts to resolve the data.

To perform spectroscopic analysis of the available spectra, I used about 120 spectral lines, spread from near ultraviolet to optical region. Notwithstanding the relatively complex spectral features that M stars have, due to the fact that the used spectra were in general resolved by some of the most technologically advanced spectrographs currently available, I was able to detect a systematic variability of radial velocity in ultraviolet and optical regions and determine its period over the last 30 years to a certain degree, despite large time gaps between some of the data. It became apparent that variability of optical and ultraviolet radial velocities v_r are distinctively different from each other. The optical radial velocity variability corresponds very well to period of about $P_{l,v_r} = 383 \pm 7$ d. Therefore, because the changes of radial velocity are likely caused by the pulsations, I interpret the radial velocity from optical region as a photospheric velocity v_{photo} of Betelgeuse and P_{l,v_r} as a period of its pulsations. Such a period corresponds to the values determined by [Kiss et al. \(2006\)](#) and [Chatys et al. \(2019\)](#).

The ultraviolet region did not yield a reasonably accurate period. To a certain degree, it seems to be affected by the pulsation cycle and the overall magnitude variability. The variability of ultraviolet radial velocities is likely due to a multitude of processes in other parts of atmosphere, likely the chromosphere. Despite the fact that most of the spectra that were used in this thesis were from ultraviolet region, the data was usually restricted to relatively short periods of time, thus proving it difficult to correctly determine the overall period. As part of studying the ultraviolet spectra, I also attempted to measure projected rotational velocity $v_{\text{rot}} \sin(i)$ of Betelgeuse, by studying additional spectra from edges of the star, and comparing them to central spectra. But this analysis did not provide reasonable

results. Apart from other reasons already discussed, the reason that the method did not succeed might be largely due to the fact, that the parts of Betelgeuse's atmosphere where ultraviolet spectral lines are formed simply do not seem to fully reflect the rotation of photosphere. However, [Kervella et al. \(2018\)](#) suggests a period of rotation between 15-20 years and a rotational coupling of Betelgeuse and its chromosphere, therefore if a more elaborate method would have been used, it would have likely been possible to determine $v_{\text{rot}} \sin(i)$. Nonetheless, [Lobel & Dupree \(2001\)](#) revealed local nonradial motions within the chromosphere and velocity flows in opposite directions, whereas (local) upflows and downflows of the parts of chromosphere are partially in phase with photospheric pulsations. That suggests why the results of ultraviolet radial velocity in this thesis did not provide expected results of $v_{\text{rot}} \sin(i)$.

For photometric analysis, I used 3 main sources. Most useful was the data from SMEI and AAVSO. SMEI provided a high-quality continuous light curve, covering almost two longer periods, based on which I was able to determine the longer period, $P_1 = 2182 \pm 284 \text{ d}$, although this result might not be fully reliable, as I discussed in [section 4.3](#). The shorter photometric period $P_2 = 419 \pm 14 \text{ d}$ is in a reasonable accordance with the two most dominant periods determined by photospheric velocities (P_{1,v_r} and P_{2,v_r}). Both the photometric periods are in accordance with the values by [Kiss et al. \(2006\)](#) and [Chatys et al. \(2019\)](#). I was not able to acquire comparably good results of periods from AAVSO, even though it covers a larger time scale than SMEI. That is likely due to it being ground based observations, hence it does not cover several months each year, when Betelgeuse is too close to Sun. As Betelgeuse has at least two periods, the gaps were likely too much of an uncertainty for the programs that I was using. However, all the photometric results were continuous sufficiently for me to be able to compare the light curve to the radial curve during the last 30 years in [figure 4.14](#).

Based on the radial and photometric variability results from the last 30 years, there does not appear to be much evidence that the Great Dimming is caused by the regular variability, nor it seems to be a convergence of different periods of variability. Nonetheless, AAVSO provided results from several different photometric filters during the Great Dimming, which shows that the longer wavelengths suffered a considerably smaller extinction of apparent magnitude than the smaller wavelengths. That likely narrows down possible origin of the Dimming to either dust absorption, or a decrease in temperature. I used approximative stellar models to determine the effects of a decrease in temperature by $\Delta T_{\text{eff}} \sim 250 \text{ K}$, and I received results similar to the Great Dimming. These models support the results in [subsection 2.2.4](#) by [Dharmawardena et al. \(2020\)](#), i.e., likely a formation of large starspots was responsible for the Great Dimming, and thus my results also oppose the results by [Levesque & Massey \(2020\)](#) to a certain degree. I had no tools to examine whether the Dimming could have been caused by dust absorption, or what effects on Betelgeuse's flux would it have had, therefore I am not able to fully rule out this major possibility that is supported by [Levesque & Massey \(2020\)](#) and [Dupree et al. \(2020\)](#). On the contrary, the minimum of ultraviolet radial velocity during the beginning the Great Dimming ([figure 4.14](#)) that was determined in this thesis likely corresponds to the mass loss event in southern hemisphere of Betelgeuse that was reported by [Dupree et al. \(2020\)](#) and according to them was responsible for the Great Dimming.

Red supergiants are complex objects, therefore to properly analyse some of the Betel-

geuse's physical properties that I touched on, it would be necessary to employ more robust methods and models. Regarding my results, it is possible that there are some discrepancies within the data, due to using numerous different data sources, as hypothetically some of the sources are not equally comparable to each other without some additional calibrations. Due to the complex nature of spectra of M stars, it might also be better to not use spectral lines quantitatively, but qualitatively. For example, instead of using a large number of spectral lines as done in this analysis, it would hypothetically be better to study specific lines, whose profiles and variability are well known in M supergiants, more thoroughly. Analysis of other significant spectral features of Betelgeuse, such as emission peaks in the ultraviolet region and titanium oxide molecular bands in the optical and infrared regions, would also reveal additional fundamental information about Betelgeuse.

Appendix

Contents:

- I) A python script to visualise spectra and add spectral lines labels to them**
- II, III and IV) Atlas of ultraviolet and optical spectral lines used in this thesis**
- V) A python script to visualize non linear STIS spectra**
- VI) A python script to convert STIS non linear spectra to a linear format for analysis in SPLAT-VO**

```

fig = plt.figure(figsize=(8.3, 11.69), dpi=180)
gs = fig.add_gridspec(5, hspace=0.2)
axs = gs.subplots(sharex=False, sharey=False)
#plt.tick_params(labelcolor="none", bottom=False, left=False)

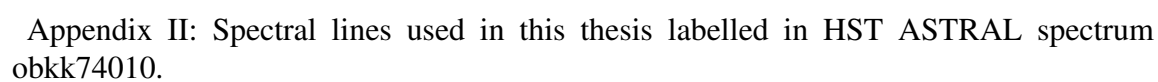
axs[0].plot(harps['Wave'],harps['Flux'], linestyle='--', linewidth=0.33)
axs[1].plot(harps['Wave'],harps['Flux'], linestyle='--', linewidth=0.33)
axs[2].plot(harps['Wave'],harps['Flux'], linestyle='--', linewidth=0.33)
axs[3].plot(harps['Wave'],harps['Flux'], linestyle='--', linewidth=0.33)
axs[4].plot(harps['Wave'],harps['Flux'], linestyle='--', linewidth=0.33)
axs[0].set_xlim([5000, 5150])
axs[0].set_ylim([0, 5])
axs[1].set_xlim([5150, 5300])
axs[1].set_ylim([0, 5])
axs[2].set_xlim([5350, 5500])
axs[2].set_ylim([0, 5])
axs[3].set_xlim([5850, 6000])
axs[3].set_ylim([0, 5])
axs[4].set_xlim([6395, 6565])
axs[4].set_ylim([0, 5])

plt.xlabel("Wavelength in Air [Å] ", fontsize=15, fontweight='bold')
axs[2].set_ylabel("Normalized Flux", fontsize=15, fontweight='bold', ha="center", va="center", labelpad=10)

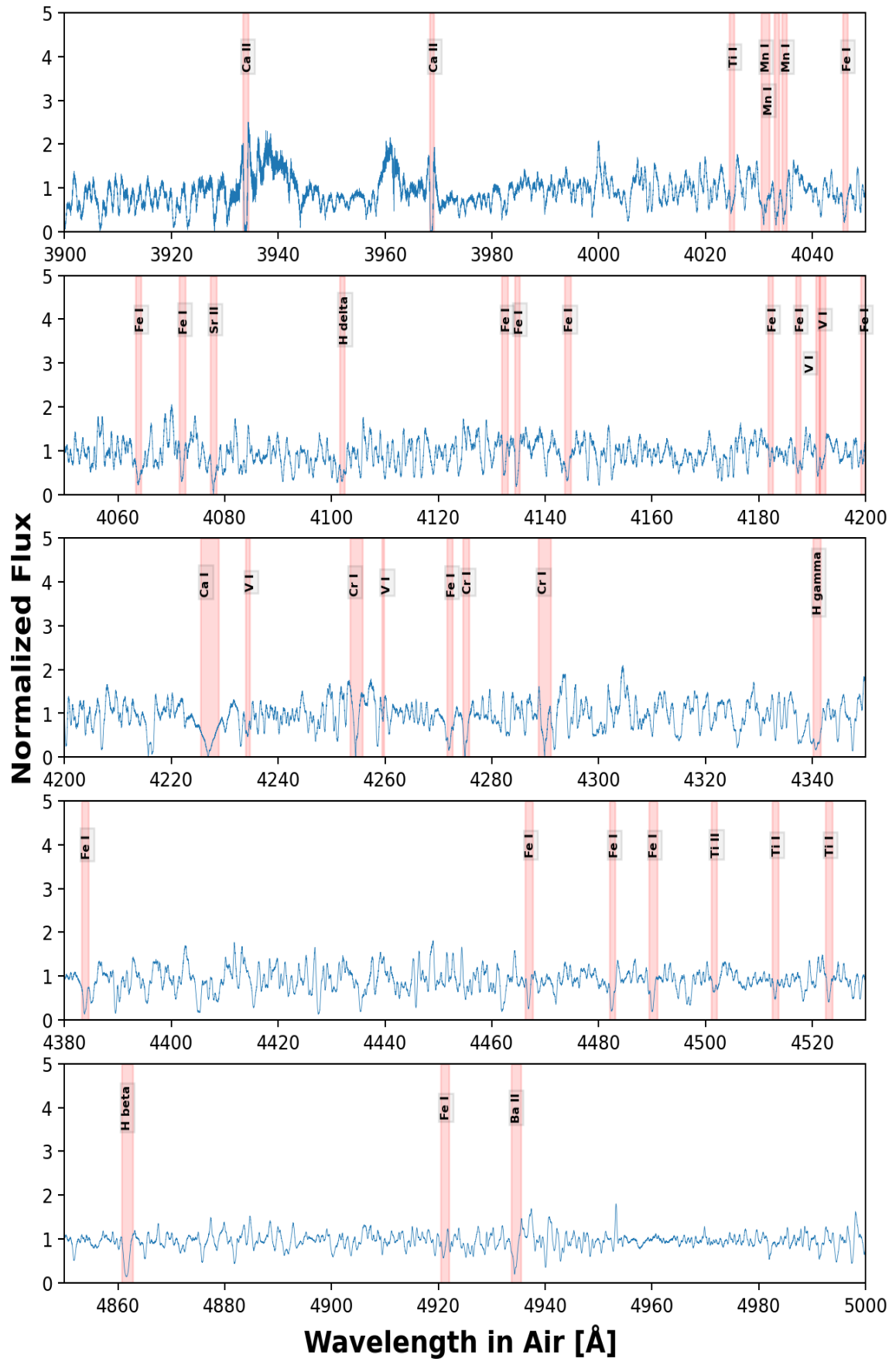
for i in range(len(opt_lines)):
    if opt_lines[i][0] > 5000 and opt_lines[i][0] < 5150:
        axs[0].axvspan(opt_lines[i][0], opt_lines[i][1], alpha=0.15, color='red')
        axs[0].text(opt_lines[i][0], 4.0, str(opt_lines[i][2]), rotation=90, fontsize=6, fontweight='bold', va='center',
                    bbox={'facecolor': 'grey', 'alpha': 0.1, 'pad': 1})
    if opt_lines[i][0] > 5150 and opt_lines[i][0] < 5300:
        axs[1].axvspan(opt_lines[i][0], opt_lines[i][1], alpha=0.15, color='red')
        axs[1].text(opt_lines[i][0], 4.0, str(opt_lines[i][2]), rotation=90, fontsize=6, fontweight='bold', va='center',
                    bbox={'facecolor': 'grey', 'alpha': 0.1, 'pad': 1})
    if opt_lines[i][0] > 5350 and opt_lines[i][0] < 5500:
        axs[2].axvspan(opt_lines[i][0], opt_lines[i][1], alpha=0.15, color='red')
        axs[2].text(opt_lines[i][0], 4.0, str(opt_lines[i][2]), rotation=90, fontsize=6, fontweight='bold', va='center',
                    bbox={'facecolor': 'grey', 'alpha': 0.1, 'pad': 1})
    if opt_lines[i][0] > 5850 and opt_lines[i][0] < 6000:
        axs[3].axvspan(opt_lines[i][0], opt_lines[i][1], alpha=0.15, color='red')
        axs[3].text(opt_lines[i][0], 4.0, str(opt_lines[i][2]), rotation=90, fontsize=6, fontweight='bold', va='center',
                    bbox={'facecolor': 'grey', 'alpha': 0.1, 'pad': 1})
    if opt_lines[i][0] > 6395 and opt_lines[i][0] < 6565:
        axs[4].axvspan(opt_lines[i][0], opt_lines[i][1], alpha=0.15, color='red')
        axs[4].text(opt_lines[i][0], 4.0, str(opt_lines[i][2]), rotation=90, fontsize=6, fontweight='bold', va='center',
                    bbox={'facecolor': 'grey', 'alpha': 0.1, 'pad': 1})

```

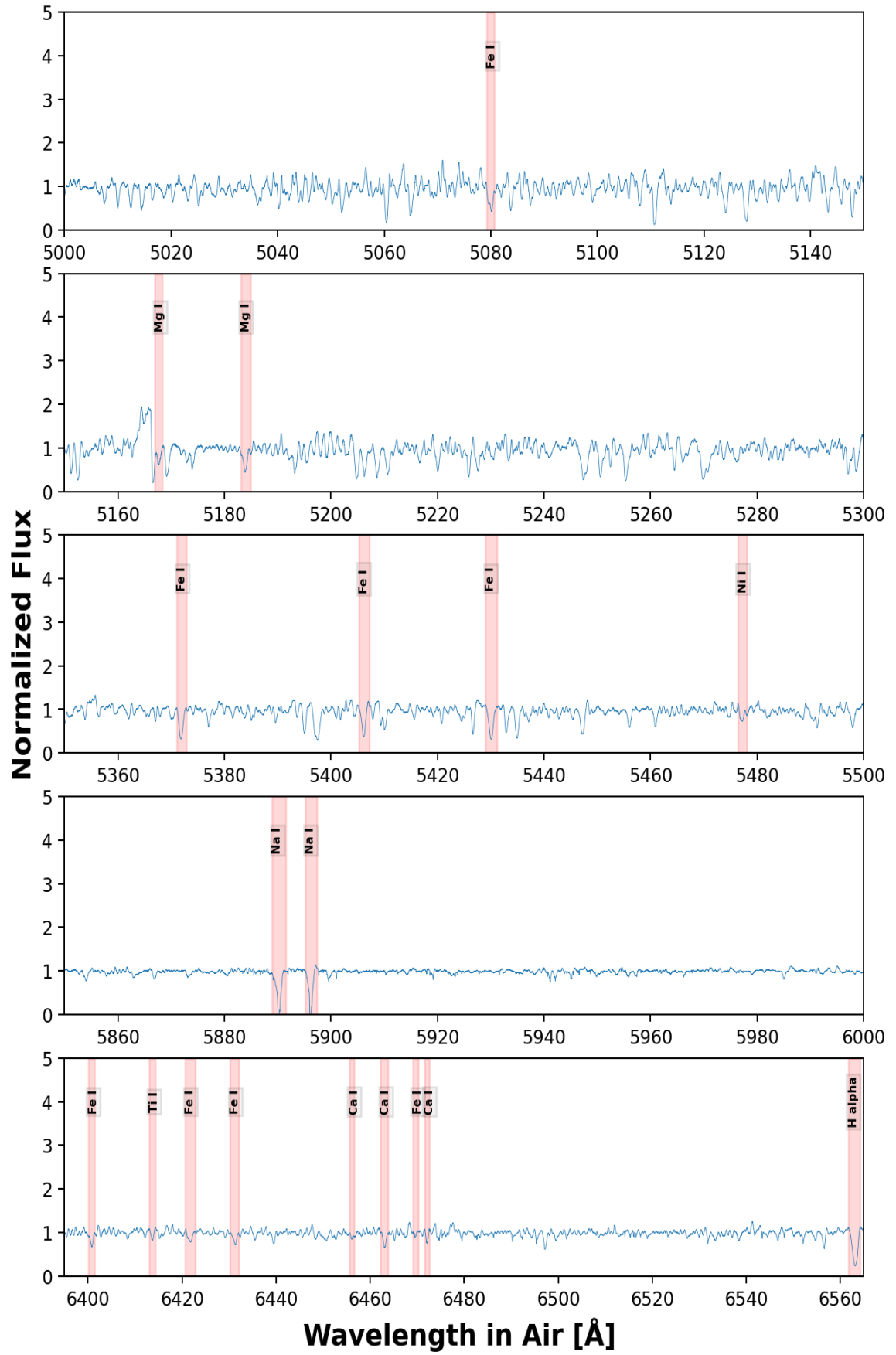
Appendix I: Sample of a python script to visualise spectra below and label the lines that I used. In spectra where some line labels were too close to each other I added positional exceptions and adjustments.



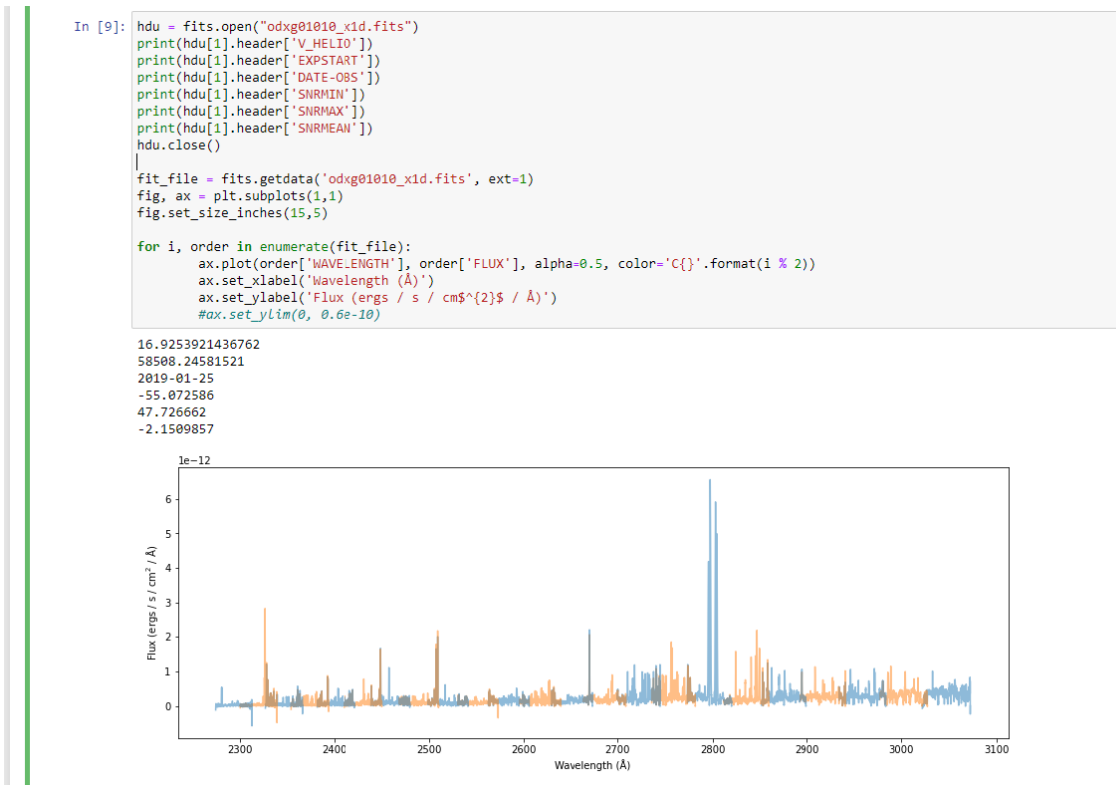
Appendix II: Spectral lines used in this thesis labelled in HST ASTRAL spectrum obkk74010.



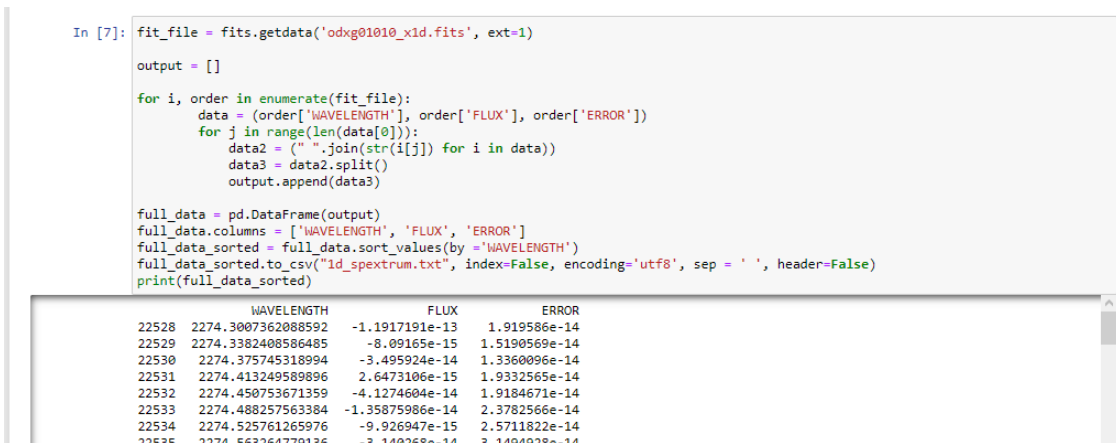
Appendix III: Spectral lines used in this thesis labelled in the HARPS spectrum.



Appendix IV: Spectral lines used in this thesis labelled in the HARPS spectrum.



Appendix V: Python script to visualise all the STIS spectral orders and list useful information from header. Adapted from a freely available STIS Data Analysis guide ([E22](#)).



Appendix VI: My own python script to transform echelle spectra wavelengths and fluxes that depend on spectral order into a classical 1D linear spectrum (in .txt format) that can be analysed in SPLAT-VO. In the default format, each row is for one spectral order, and all the wavelengths are stored in one cell per row. What the script accomplishes is that it extracts the data from the cells, and add them all into columns, along with the wavelengths.

Bibliography

- Carroll, B. W., & Ostlie, D. A., *An Introduction to Modern Astrophysics*, Addison-Wesley, 2nd Edition, 2007, p. 1278, 0-321-44284-9
- Chromey, F. R., *To Measure the Sky: An Introduction to Observational Astronomy*, Cambridge University Press, 2010, p. 462, 978-0521747684
- Elridge, J. J., & Tout, Ch. A., *The Structure and Evolution of Stars*, World Scientific Publishing Europe, 2019, p. 240, 978-1-78326-579-4
- Gray, R. O., & Corbally, Ch. J., *Stellar Spectral Classification*, Princeton University Press, 2009, p. 592, 978-0-691-12510-7
- Karttunen, H., Kroger, P., Oja, H., et al., *Fundamental astronomy*, Springer-Verlag Berlin Heidelberg, 3rd Edition, 1996, p. 542, 3-540-60936-9
- Kippenhahn, R., Weigert, A., Wess, A., *Stellar Structure and Evolution*, Springer, 2nd Edition, 2012, p. 622, 978-3642445248
- Lambourne, R. J. A., *Relativity, Gravitation and Cosmology*, Cambridge University Press, 2010, p. 312, 978-0521131384
- Maeder, A., *Physics, Formation and Evolution of Rotating Stars*, Springer, 2009, p. 853, 978-3540769484
- Morison, I., *Introduction to astronomy and cosmology*, WILEY, 2008, p. 360, 978-0-470-03333-3
- Robinson, K., *Spectroscopy: The Key to the Stars: Reading the Lines in Stellar Spectra*, Cambridge University Press, 2007, p. 172, 978-0387367866
- Sion, E. N., Vennes, S., Shipman, H. L., *White Dwarfs: Cosmological and Galactic Probes*, SPRINGER, 2005, p. 279, 978-1-4020-3693-4
- Stahler, S., & Palla, F., *The Formation of Stars*, WILEY-VCH Verlag GmbH & Co. KGaA, 2004, p. 865, 3-527-40559-3
- Trypsteen, M. F. M., & Walker, R., *Spectroscopy for Amateur Astronomers*, Cambridge University Press, 2017, p. 151, 978-1-107-16618-9

Articles

- Ayres, T. R., *HST/STIS Advanced Spectral Library (ASTRAL)*, International Workshop on Stellar Spectral Libraries ASI Conference Series, 2014, Vol. 11, pp. 1-6, 2014
- Baranne, A., Queloz, D., Mayor, M., et al., *ELODIE: A spectrograph for accurate radial velocity measurements*, Astronomy and Astrophysics Supplement, v. 119, p. 373-390, 1996
- Bernasconi, P. A., & Maeder, A., *About the absence of a proper zero age main sequence for massive stars*, Astronomy and Astrophysics, i. 307, p.829, 1996
- Bianco, F. B., et al., *Multi-color Optical and Near-infrared Light Curves of 64 Stripped-envelope Core-Collapse Supernovae*, The Astrophysical Journal Supplement, v. 213, i. 2, 2014
- Bonneau, D., & Labeyrie, A., *Speckle Interferometry: Color-Dependent Limb Darkening Evidenced on Alpha Orionis and Omicron Ceti*, Astrophysical Journal, v. 181, 1973
- Brandt, J. C., Heap, S. R., Beaver, E. A., et al., *An Atlas of Alpha Orionis Obtained with the Goddard High Resolution Spectrograph on the Hubble Space Telescope*, Astronomical Journal, v. 109, p. 2706 1995
- Burns, D., Baldwin, J. E., et al., *The surface structure and limb-darkening profile of Betelgeuse*, Monthly Notices of the Royal Astronomical Society, v. 290, i. 1, p. L11-L16 1997
- Buscher, D. F., Haniff, C. A., Baldwin, J. E., et al., *Detection of a bright feature on the surface of Betelgeuse*, Monthly Notices of the Royal Astronomical Society, v. 245, 1990
- Chamel, N., Haensel, P., Zdunik, J. L., Fantina, A. F., *On the Maximum Mass of Neutron Stars*, International Journal of Modern Physics E, v. 22, i. 7, 2013
- Chandrasekhar, S., *The highly collapsed configurations of a stellar mass (Second paper)*, Monthly Notices of the Royal Astronomical Society, i. 95, p.207, 1935
- Castro-Neves, M., & Draper, P. W., *SPLAT-VO: Spectral Analysis Tool for the Virtual Observatory*, Astrophysics Source Code Library, record ascl:1402.008, 2014
- Chatys, F. W., Bedding, T. R., Murphy, S. J., et al., *The period–luminosity relation of red supergiants with Gaia DR2*, Monthly Notices of the Royal Astronomical Society, v. 487, i. 4, pp. 4832–4846 2019
- Crowther, P., *Evolution of Massive Stars, Mass Loss and Winds*, (eds. M. Heydari-Malayeri, Ph. Stee, J.-P. Zahn), EAS Publications Series, v. 13, p. 119 , 2004
- Dekker, H., D’Odorico, S., Kaufer, A., et al., *Design, construction, and performance of UVES, the echelle spectrograph for the UT2 Kueyen Telescope at the ESO Paranal Observatory*, Proc. SPIE, Optical and IR Telescope Instrumentation and Detectors, v. 4008, p. 534-545 , 2000

- Dharmawardena, T. E., Mairs, S., Scicluna, P., et al., *Betelgeuse Fainter in the Submillimeter Too: An Analysis of JCMT and APEX Monitoring during the Recent Optical Minimum*, The Astrophysical Journal Letters, v. 897, i. 1, id.L9, 7 pp. 2020
- Dolan, M. M., Mathews, G. J., Lam, D. D., et al., *Evolutionary Tracks for Betelgeuse*, The Astrophysical Journal, v. 819, i. 1, 15 pp 2016
- Dupree, A. K., Strassmeier, K. G., Matthews, L. D., et al., *Spatially Resolved Ultraviolet Spectroscopy of the Great Dimming of Betelgeuse*, The Astrophysical Journal, v. 899, i. 1, id.68 2020
- Ekström, S., Georgy, C., Eggenberger, P., Meynet, G., *Grids of stellar models with rotation. I. Models from 0.8 to 120 M_{\odot} at solar metallicity ($Z = 0.014$)*, Astronomy And Astrophysics, v. 537, id. A146, p. 18 , 2012
- Famaey, B., Jorissen, A., Luri, X., et al., *Local kinematics of K and M giants from CORAVEL/Hipparcos/Tycho-2 data*, Astronomy and Astrophysics, v. 430, p. 165-186 2005
- Fekel, F. C., *Rotational Velocities of B, A, and Early-F Narrow-lined Stars*, The Publications of the Astronomical Society of the Pacific, v. 115, i. 809, pp. 807-810. 2003
- Gehrz, R. D., Marchetti, J., McMillan, S., et al., *Betelgeuse remains steadfast in the infrared*, The Astronomer's Telegram, No. 13518 2020
- Gilliland, R. L., & Dupree, A. K., *First Image of the Surface of a Star with the Hubble Space Telescope*, Astrophysical Journal Letters, v. 463, p.L29 1996
- Guinan, E. F., Wasatonic, R. J., Calderwood, T. J., *Updates on the "Fainting" of Betelgeuse*, The Astronomer's Telegram, No. 13365 2019
- Guinan, E. F., Wasatonic, R. J., Calderwood, T. J., *The Fall and Rise in Brightness of Betelgeuse*, The Astronomer's Telegram, No. 13512 2020
- Harper, G. M., Brown, A., Guinan, E. F., *A New VLA-Hipparcos Distance to Betelgeuse and its Implications*, The Astronomical Journal, v. 135, i. 4, pp. 1430-1440 2008
- Harper, G. M., Brown, A., Guinan, E. F., et al., *An Updated 2017 Astrometric Solution for Betelgeuse*, The Astronomical Journal, v. 154, i. 1, 6 pp. 2017
- Harper, G. M., Guinan, E. F., Wasatonic, R., Ryde, N., *The Photospheric Temperatures of Betelgeuse during the Great Dimming of 2019/2020: No New Dust Required*, The Astrophysical Journal, v. 905, i. 1, id.34, 11 pp. 2020
- Hayashi, Ch., & Nakano, T., *Evolution of Stars of Small Masses in the Pre-Main-Sequence Stages*, Progress of Theoretical Physics, v. 30, i. 4, p.460, 1963
- Iben, I. Jr., & Tutukov, A. V., *Supernovae of type I as end products of the evolution of binaries with components of moderate initial mass*, Astrophysical Journal, v. 54, p. 335, 1984

- Jackson, B. V., Buffington, A., Hick, P. P., et al., *The Solar Mass-Ejection Imager (SMEI) Mission*, Solar Physics, v. 225, i. 1, pp.177-207, 2004
- Joyce, M., Leung, S., Molnár, L., et al., *Standing on the Shoulders of Giants: New Mass and Distance Estimates for Betelgeuse through Combined Evolutionary, Asteroseismic, and Hydrodynamic Simulations with MESA*, The Astrophysical Journal, v. 902, i. 1, 25 pp. 2020
- Kalogera, V., & Baym, G., *The Maximum Mass of a Neutron Star*, Astrophysical Journal Letters, v. 470, p. L61, 1996
- Karovska, M., Noyes, R. W., Roddier, F., et al., *On a Possible Close Companion to alpha Ori*, Bulletin of the American Astronomical Society, v. 17, p.598 1985
- Kaufer, A., *Variable Circumstellar Structure of Luminous Hot Stars: the Impact of Spectroscopic Long-term Campaigns*, Reviews in Modern Astronomy 11: Stars and Galaxies, v. 11, p. 177, 1998
- Keenan, P. C., & McNeil, R. C., *The Perkins Catalog of Revised MK Types for the Cooler Stars*, Astrophysical Journal Supplement v. 71, p. 245 1989
- Kervella, P., Decin, L., Richards, A. M. S., et al., *The close circumstellar environment of Betelgeuse. V. Rotation velocity and molecular envelope properties from ALMA*, Astronomy and Astrophysics, v. 609, p. 17, 2018
- Kiss, L. L., Szabó, G. M., Bedding, T. R., *Variability in red supergiant stars: pulsations, long secondary periods and convection noise*, Monthly Notices of the Royal Astronomical Society, v. 372, i. 4, p. 1721-1734. 2006
- Kravchenko, K., Jorissen, A., Van Eck, S., et al., *Atmosphere of Betelgeuse before and during the Great Dimming event revealed by tomography*, Astronomy and Astrophysics, manuscript no. 39801corr 2021
- Lambert, D. L., Brown, J. A., Hinkle, K. H., Johnson, H. R., *Carbon, nitrogen and oxygen abundances in Betelgeuse*, Astrophysical Journal, v. 284, p. 223-237, 1984
- Lenz, P., & Breger, M., *Period04 User Guide*, Communications in Asteroseismology, v. 146, p. 53-136 2005
- Levesque, E. M., & Massey, P., *Betelgeuse Just Is Not That Cool: Effective Temperature Alone Cannot Explain the Recent Dimming of Betelgeuse*, The Astrophysical Journal Letters, v. 891, i. 2, id.L37, p. 6 2020
- Lobel, A., & Dupree, A. K., *Spatially Resolved STIS Spectroscopy of α Orionis: Evidence for Nonradial Chromospheric Oscillation from Detailed Modeling*, The Astrophysical Journal, v. 558, i. 2, p. 815-829. 2001
- Maeder, A., *Grids of evolutionary models for the upper part of the HR diagram. Mass loss and the turning of some red supergiants into WR stars.*, Astronomy and Astrophysics, v. 102, p. 401 - 410, 1981

- Maeder, A., & Meynet, G., *Grids of evolutionary models of massive stars with mass loss and overshooting - Properties of Wolf-Rayet stars sensitive to overshooting.*, Astronomy and Astrophysics, v. 182, p. 243 - 263, 1987
- Mayor, M., Pepe, F., Queloz, D., et al., *Setting New Standards with HARPS*, The Messenger, No.114, p. 20-24, 2003
- Meynet, G., & Maeder, A., *Stellar evolution with rotation - V.*, Astronomy and Astrophysics, v. 361, p. 101-120, 2000
- Meynet, G., & Maeder, A., *Stellar evolution with rotation - X.*, Astronomy and Astrophysics, v. 404, p. 975 - 990, 2003
- Meynet, G., Chomienne, V., Ekström, S., et al., *Impact of mass-loss on the evolution and pre-supernova properties of red supergiants*, Astronomy And Astrophysics, v. 575, id. A60, p. 18 , 2015
- Michelson, A. A., & Pease, F.G., *Measurement of the Diameter of alpha Orionis with the Interferometer*, Astrophysical Journal, v. 53, p. 249-259, 1921
- Mokiem, M. R., de Koter, A., Vink, J. S., et al., *The empirical metallicity dependence of the mass-loss rate of O- and early B-type stars*, Astronomy and Astrophysics, v. 473, i. 2, p. 603-614 , 2007
- Morgan, W. W., Keenan, P. C., Kellman, E., *An atlas of stellar spectra, with an outline of spectral classification*, Chicago, Ill., The University of Chicago press, 1943
- Ozel, F., & Freire, P., *Masses, Radii, and Equation of State of Neutron Stars*, Annual Review of Astronomy and Astrophysics, v. 54, p.401, 2016
- Paunzen, E., & Vanmunster, T., *Peranso - Light curve and period analysis software*, Astronomische Nachrichten, v. 337, i. 3, p. 239, 2016
- Perruchot, S., Kohler, D., Bouchy, F., et al., *The SOPHIE spectrograph: design and technical key-points for high throughput and high stability*, Ground-based and Airborne Instrumentation for Astronomy II., Proceedings of the SPIE, v. 7014, 12 pp., 2008
- Pigulski, A., et al., *BRITE Cookbook 2.0*, Polish Astronomical Society, v. 8, p. 175-192 , 2018
- Reimers, D., *Circumstellar absorption lines and mass loss from red giants*, Memoires of the Societe Royale des Sciences de Liege, v. 8, p. 369-382 , 1975
- Sigismondi, C., Vollmann, W., Nickel, O., et al., *Second dust cloud on Betelgeuse*, The Astronomer's Telegram, No. 13982 2020
- Stothers, R. B., *Giant Convection Cell Turnover as an Explanation of the Long Secondary Periods in Semiregular Red Variable Stars*, The Astrophysical Journal, v. 725, i. 1, pp. 1170-1174 2010

- Turatto, M., *Classification of Supernovae*, Lecture Notes in Physics, v. 598, p. 21, 2003
- Uitenbroek, H., Dupree, A. K., Gilliland, R. L., *Spatially Resolved Hubble Space Telescope Spectra of the Chromosphere of alpha Orionis*, The Astronomical Journal, v. 116, i. 5, pp. 2501-2512 1998
- van der Hucht, K. A., *New Galactic Wolf-Rayet stars, and candidates. An annex to The VIIth Catalogue of Galactic Wolf-Rayet Stars*, Astronomy and Astrophysics, v. 458, i. 2, p. 453-459, 2006
- van Loon, J. Th., *Betelgeuse and the red supergiants*, EAS Publications Series, v. 60, p. 307-316 , 2012
- Vernet, J., Dekker, H., D'Odorico, S., Kaper, L., et al., *X-shooter, the new wide band intermediate resolution spectrograph at the ESO Very Large Telescope*, Astronomy and Astrophysics, v. 536, 15 pp., 2011
- Vink, J. S., de Koter, A., Lamers, H. J. G. L. M., *Mass-loss predictions for O and B stars as a function of metallicity*, Astronomy And Astrophysics, v. 369, p. 574-588 , 2001
- Wood, P. R., *Variable Red Giants in the LMC: Pulsating Stars and Binaries?*, Publications of the Astronomical Society of Australia, v. 17, i. 1, p.18-21 2000
- Wood, P. R., Olivier, E. A., Kawaler, S. D., *Long Secondary Periods in Pulsating Asymptotic Giant Branch Stars: An Investigation of their Origin*, The Astrophysical Journal, v. 604, i. 2, pp. 800-816. 2004
- Wilk, S. R., *Further Mythological Evidence for Ancient Knowledge of Variable Stars*, The Journal of the American Association of Variable Star Observers, v. 27, n. 2, p. 171-174, 1999
- Woosley, S. E., Heger, A., Weaver, T. A., *The evolution and explosion of massive stars*, Reviews of Modern Physics, v. 74, i. 4, p. 1015, 2002

Electronic Publications

- Mikulášek, Z., & Krtićka, J., *Introduction to Physics of Stars*, Masaryk University - Department of Theoretical Physics and Astrophysics, 2005, URL: <https://astro.physics.muni.cz/download/documents/skripta/F3080.pdf>, [Online, accessed February 9th, 2021]
- Krtićka, J., *Physics of Hot Stars II*, Masaryk University - Department of Theoretical Physics and Astrophysics, 2015, URL: https://astro.physics.muni.cz/download/documents/skripta/F7601_2.pdf, [Online, accessed April 27th, 2021]
- Pols, O. R., *Stellar Structure and Evolution*, Astronomical Institute Utrecht, 2011, URL: <http://www.icolick.org/~woosley/ay112-14/texts/pols11.pdf>, [Online, accessed February 9th, 2021]

Other Electronic Sources

- [E1] Australia Telescope National Facility, *The Hertzsprung-Russell Diagram*, Hollow, R., 2002, URL: <https://www.atnf.csiro.au/outreach/education/senior/astrophysics>, [Online, accessed April 27th, 2021]
- [E2] The Infrared Processing and Analysis Center at Caltech, *Explanatory Supplement to the 2MASS All Sky Data Release and Extended Mission Products*, Cutri, R. M., Skrutskie, M. F., Van Dyk, S., 2006, URL: <https://old.ipac.caltech.edu/2mass/releases/allsky/doc/>, [Online, accessed April 22th, 2021]
- [E3] European Space Agency, *ESO Telescope Sees Surface of Dim Betelgeuse*, Montargès, M., Cannon, E., Kervella, P., Ferreira, B., 2019, URL: <https://www.eso.org/public/news/eso2003/>, [Online, accessed April 22th, 2021]
- [E4] <http://star-www.dur.ac.uk/~pdraper/splat/splat.html>
- [E5] <http://spectra.freeshell.org/whyspectroweb.html>
- [E5] https://physics.nist.gov/PhysRefData/ASD/lines_form.html
- [E6] <http://archive.eso.org/scienceportal/home>
- [E7] <http://atlas.obs-hp.fr/sophie/>
- [E8] <http://atlas.obs-hp.fr/elodie/>
- [E9] <http://dc.zah.uni-heidelberg.de/flashheros/q/web>
- [E10] <https://archive.stsci.edu/hst/atlasalfori/>
- [E11] <https://archive.stsci.edu/prepds/astral/#catalog>
- [E12] <https://archive.stsci.edu/hst/search.php>
- [E13] <http://www.star.bris.ac.uk/~mbt/topcat/>
- [E14] <https://www.gb.nrao.edu/cgi-bin/radvelcalc.py>
- [E15] <https://www.cbabelgium.com/peranso/downloads.html>
- [E16] <http://brite-wiki.astro.uni.wroc.pl/bwiki/doku.php?id=start>
- [E17] <https://earth.esa.int/web/eoportal/satellite-missions/c-missions>
- [E18] https://www.cosmos.esa.int/web/gaia/iow_20180316
- [E19] <https://www.aavso.org>
- [E20] <https://www.univie.ac.at/tops/Period04/>
- [E21] <https://wwwuser.oats.inaf.it/castelli/grids.html>
- [E22] <https://hst-docs.stsci.edu/stisdhb>

